

AD A 120828

AD-F 500085

12

NSWC TR 81-491

DYNAMIC TESTING WITH THE NSWC THREE- DEGREE-OF-FREEDOM GAS BEARING

BY F. J. REGAN

STRATEGIC SYSTEMS DEPARTMENT

8 MARCH 1982

Approved for public release, distribution unlimited.

DTIC
ELECTE
S OCT 27 1982 D
B



NAVAL SURFACE WEAPONS CENTER

Dahlgren, Virginia 22448 • Silver Spring, Maryland 20910

DTIC FILE COPY

82 10 25 019

UNCLASSIFIED

SECURITY CLASSIFICATION OF THIS PAGE (When Data Entered)

REPORT DOCUMENTATION PAGE		READ INSTRUCTIONS BEFORE COMPLETING FORM
1. REPORT NUMBER NSWC TR 81-491	2. GOVT ACCESSION NO. AD-A120828	3. RECIPIENT'S CATALOG NUMBER
4. TITLE (and Subtitle) DYNAMIC TESTING WITH THE NSWC THREE-DEGREE-OF-FREEDOM GAS BEARING		5. TYPE OF REPORT & PERIOD COVERED
		6. PERFORMING ORG. REPORT NUMBER
7. AUTHOR(s) F. J. REGAN		8. CONTRACT OR GRANT NUMBER(s)
9. PERFORMING ORGANIZATION NAME AND ADDRESS Naval Surface Weapons Center (Code K22) White Oak Silver Spring, MD 20910		10. PROGRAM ELEMENT, PROJECT, TASK AREA & WORK UNIT NUMBERS 11221N J0094, SB/77430
11. CONTROLLING OFFICE NAME AND ADDRESS		12. REPORT DATE 8 March 1982
		13. NUMBER OF PAGES 138
14. MONITORING AGENCY NAME & ADDRESS (if different from Controlling Office)		15. SECURITY CLASS. (of this report) UNCLASSIFIED
		15a. DECLASSIFICATION/DOWNGRADING SCHEDULE
16. DISTRIBUTION STATEMENT (of this Report) Approved for public release; distribution unlimited.		
17. DISTRIBUTION STATEMENT (of the abstract entered in Block 20, if different from Report)		
18. SUPPLEMENTARY NOTES		
19. KEY WORDS (Continue on reverse side if necessary and identify by block number) Wind tunnel testing Dynamic testing pitch damping ablation		
20. ABSTRACT (Continue on reverse side if necessary and identify by block number) This report presents the design, construction and operational procedures of the NSWC Three-Degree-of-Freedom Gas Bearing. The data reduction technique that is used with angular measurements from this support is developed and applied to measured wind tunnel data. These wind tunnel data were obtained from non-ablating and ablating models undergoing dynamic motion in the NSWC Hypersonic Wind Tunnel. Test results are compared with earlier experiments with dynamic ablating models and theoretical speculations.		

UNCLASSIFIED

SECURITY CLASSIFICATION OF THIS PAGE (When Data Entered)

UNCLASSIFIED

SECURITY CLASSIFICATION OF THIS PAGE (When Data Entered)

20. (Cont.)

All tests were carried out at Mach 7.95.

UNCLASSIFIED

SECURITY CLASSIFICATION OF THIS PAGE (When Data Entered)

FOREWORD

This report discusses a three-degree-of-freedom dynamic wind tunnel test program using slender cones with and without nose-tip ablation. These tests were carried out in the NSWC Hypersonic Tunnel using a gas-bearing support designed and fabricated specifically for this program. A data reduction program, also formulated for these tests, provided static and dynamic stability derivatives from measurements of bi-planar displacement angles. Comparisons are made where possible with results from previously conducted static tests. A significant result of these tests was a demonstration of the dynamic unstabilities associated with the presence of nose-tip ablation. Also, it was shown that during ablation there is continual and significant forward motion of the static center of pressure. This test program was sponsored by the Reentry Aerodynamics program.

A. M. Morrison

A. M. Morrison
By direction



Accession For	
NTIS GRA&I	<input checked="" type="checkbox"/>
DTIC TAB	<input type="checkbox"/>
Unannounced	<input type="checkbox"/>
Justification	
By	
Distribution/	
Availability Codes	
Dist	Avail and/or Special
A	

CONTENTS

	<u>Page</u>
1.0 INTRODUCTION	7
2.0 BEARING DESIGN/CONSTRUCTION	8
3.0 DATA REDUCTION	19
3.1 DIFFERENTIAL EQUATION OF MOTION	19
3.2 DATA REDUCTION EQUATIONS	27
3.3 COMPUTER PROGRAM	40
4.0 WIND TUNNEL TEST	54
4.1 NON-ABLATING NOSE WIND TUNNEL TESTS	56
4.2 ABLATING NOSE WIND TUNNEL TESTS	73
4.3 POST-ABLATION WIND TUNNEL TEST - ABLATING NOSE SUBSTRUCTURE (SYMMETRICAL)	106
4.4 POST-ABLATION WIND TUNNEL TEST - ABLATING NOSE SUBSTRUCTURE (ASYMMETRICAL)	125
5.0 CONCLUSIONS	127
6.0 BIBLIOGRAPHY	128

ILLUSTRATIONS

Figure		Page
1	Sphere/Cone Model Mounted in the Naval Surface Weapons Center Hypersonic Wind Tunnel	10
2	Gas Bearing Assembly and Readout	11
3	Gas Bearing Assembly/Readout Components	12
4	Air Bearing Section	14
5	Model Schematic	16
6	Orthogonal Camera Coverage of Model Motion	21
7	External Dimensions of Wind Tunnel Model	53
8	Representative Model Photographic Views Approximately 1 Second Apart	55
9	Angles of Attack and Sideslip Versus Time (Hemi-Spherical Nose)	57
10	Angle of Attack Versus Angle of Sideslip for Time Intervals (Hemi-Spherical Nose)	61
11	Plotted Force Data for $r_N/r_B = 0.223$ Configuration with Straight Sting	72
12	Ablating Nose Substructure	74
13	Nose Ablation Sequence	76
14	Angles of Attack and Sideslip Versus Time (Ablating Nose)	85
15	Angle of Attack Versus Angle of Sideslip (Ablating Nose)	89
16	Relative Position of Initial Windward Meridian and Instantaneous Windward Meridian (Ablating Nose)	102
17	Angles of Attack and Sideslip Versus Time (Ablating Nose Substructure-No Tilt)	109
18	Angle of Attack Versus Angle of Sideslip (Ablating Nose Substructure-No Tilt)	112
19	Angle of Attack Versus Angle of Sideslip (Ablating Nose Substructure-3 Degree Tilt)	122

TABLES

<u>Table</u>		<u>Page</u>
1	Equation (1) Symbol Definition	20
2	Least Squares/Differential Corrections Data Reduction Program	41
3	Stability Derivative Program	48
4	Symbol Definition	50
5	Data Reduction for Data Points 1 To 900 for Sphere Cone Model	71
6	Non-Dimensional Aerodynamic Coefficients and Spin Rate for Data Points 1 To 900	71
7	Summary of Ablating Model Wind Tunnel Tests	99
8	Summary of Reduced Data from Post-Ablation Model with Symmetrical Nose Substructure.	108
9	Non-Dimensional Aerodynamic Coefficients and Spin Rate for Mode with Asymmetrical nose Substructure.	126

1.0 INTRODUCTION

In conventional wind tunnel testing the model is attached to a rigid structure, often a cantilever beam. This support is called a "wind tunnel balance" since an integral part of the structure is a load measuring unit. A measurement of the forces of constraint is assumed equivalent to a measurement of the aerodynamic loads. By rotating the model and/or support structure relative to the flow vector, the dependency of load on angle can also be measured. While there is much to recommend testing of rigidly constrained models, such testing cannot measure the aerodynamic effects caused by the rate of change of angular variables. The three-degree-of-freedom gas bearing support was designed to permit the measurement of time dependent aerodynamic loads. The model is supported by a cantilever beam with the attachment point at the model's center of gravity. The support permits restricted angular motion in pitch and yaw (about 7.5 degrees) and unrestricted angular motion in roll.

While physical realism may be enhanced by the testing of unconstrained models, the determination of the aerodynamic loads is no longer a primary measurement as it is in constrained model testing. The primary measurement is model angular displacement from a null or trim condition. In the three-degree-of-freedom gas bearing support these angles are roll, pitch (angle of attack), and yaw (angle of sideslip). The task facing the analyst, then, is to deduce what the loads must have been during the test in order to produce the observed motion. The procedure then involves postulating or modeling the flow-body interaction. This is equivalent to postulating the form of relevant differential equation(s).

In the present application the differential equation describes the external flow of a compressible fluid about a non-permeable structure. The fluid is regarded as being everywhere continuous and the component of the fluid velocity normal to the surface of the structure is everywhere zero. If the differential

equation is linear then the coefficients may be regarded as "constants of proportionality" between angular displacement (and its derivative) and the applied moment. The recordings of angular displacement (primary measurements) are in a sense "solutions" of the differential equations; the goal of data reduction, then, is to determine the numerical values of the coefficients that provide (according to some criterion) the "best fit" to the observed (measured) angular motion. The criterion that will be used here for "best fit" will minimize the square of the "error" or difference between the assumed function and the data points.

The emphasis of this report will be on the use of the Three-Degree-of-Freedom Gas Bearing (TDGB) rather than on its mechanical design. However, a description of the mechanical features along with annotated assembly drawings and photographs will be included. The readout or data-gathering techniques associated with this TDGB can never be regarded as complete, since technological improvements will suggest alterations from time-to-time.

By way of supporting claims of utility, some wind tunnel test results will also be included. Non-dimensional aerodynamic coefficients will be given for both ablating and non-ablating configurations.

2.0 BEARING DESIGN/CONSTRUCTION

The Three-Degree-of-Freedom Gas Bearing (TDGB) permits unlimited model freedom in roll and restricted freedom in angles of attack and sideslip. It is certainly possible to provide the same degrees of freedom with a gimbal system using mechanical bearings. However, in the present application where heat loads are modest, a gas bearing is particularly attractive because of its low and consistent friction. However, the gas bearing does require a continuous supply of gas (air in present case) and as it turns out, some control of the temperature of the gas entering the region of the bearing sphere is necessary to maintain sphere/socket clearances. The bearing air also must exit the model's base. However the

mass flow is so small that exhaust air has no significant effect on model motion.

The sphere/cone model is shown attached to the gas bearing and mounted in the NSWC Hypersonic Wind Tunnel in Figure 1. This model is a 7° cone (half-angle) with at 22 percent spherical bluntness. All aerodynamic data presented in this report were obtained using this model (see section (4)).

The gas bearing assembly and angular readout is shown in Figure 2. This support and readout system is intended for conical models. The model mounts directly to the assembly which in turn is attached to the cantilever or "sting" support.

Figure 3 is an exploded view of the assembly shown in Figure 2. The front and aft ball housings form the stator of the 2.5 inch diameter sphere also called the "socket." The inner surface of the housings is molded epoxy (DEVCON). The clearance tolerance between the sphere and the epoxy socket is on the order of 0.001 inch. The method of forming this socket and maintaining this tolerance is interesting. When the sphere is fabricated a second and nearly identical sphere is also fabricated. This second sphere is then nickel plated. The epoxy socket is then molded to this plated sphere. The unplated sphere then fits the socket with the required clearance. Sphere-socket clearance may vary somewhat so the plating thickness may vary a few thousandths of an inch. However, more important than the clearance itself is consistency in clearance all around the bearing surface. The only difficulties experienced with the bearing clearance were caused by cooled air (due to expansion) which contracted the epoxy after prolonged bearing use. Heating the air prior to entry at the bearing surface totally eliminated this problem.

All components aft of the ball housing are associated with the pitch/yaw/roll fiber optic readout system. This system was not entirely satisfactory although some angular measurements using the fiber optic system were used for data

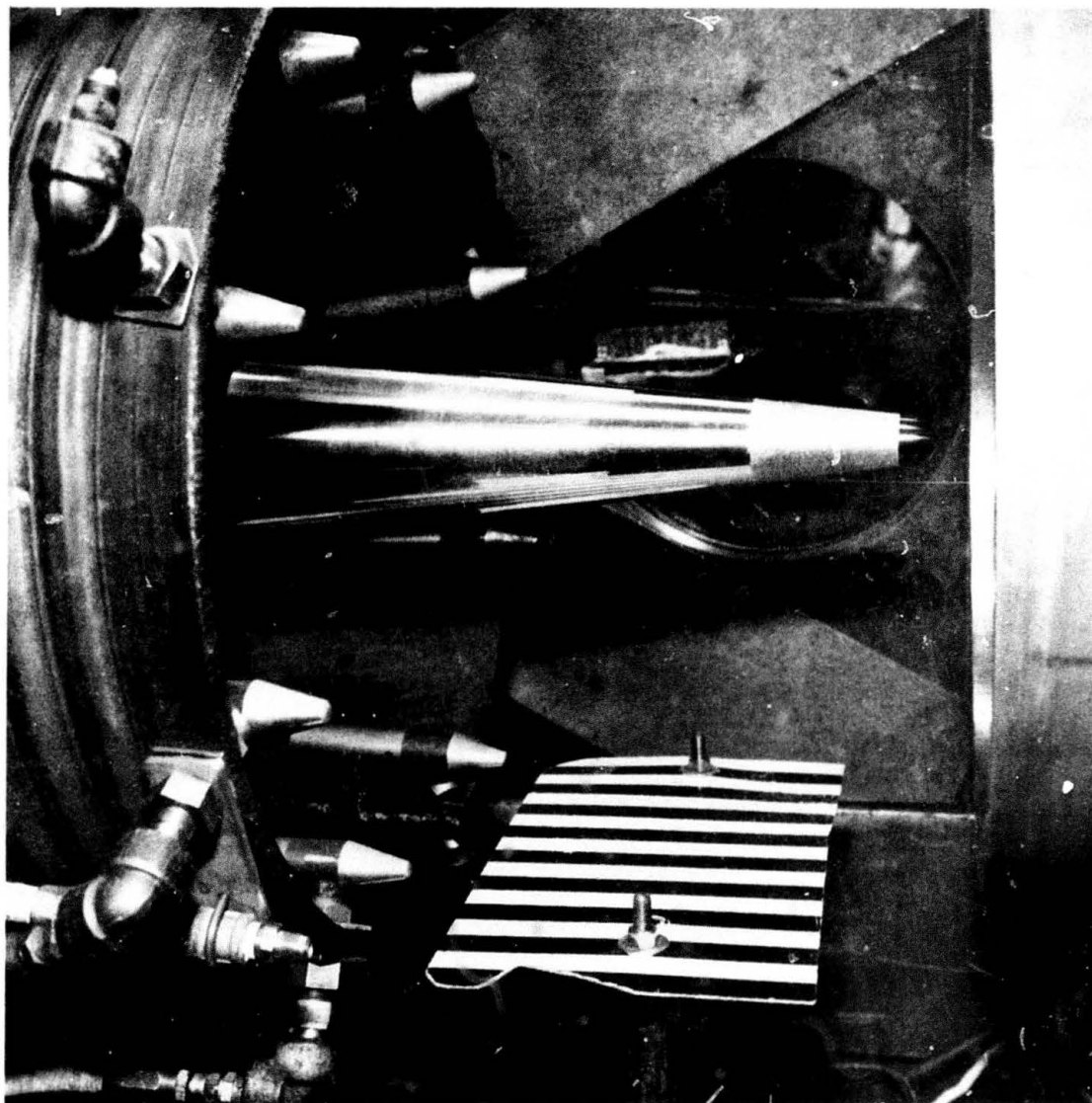


FIGURE 1 SPHERE/CONE MODEL MOUNTED IN THE NAVAL SURFACE WEAPONS CENTER HYPER-SONIC WIND TUNNEL.

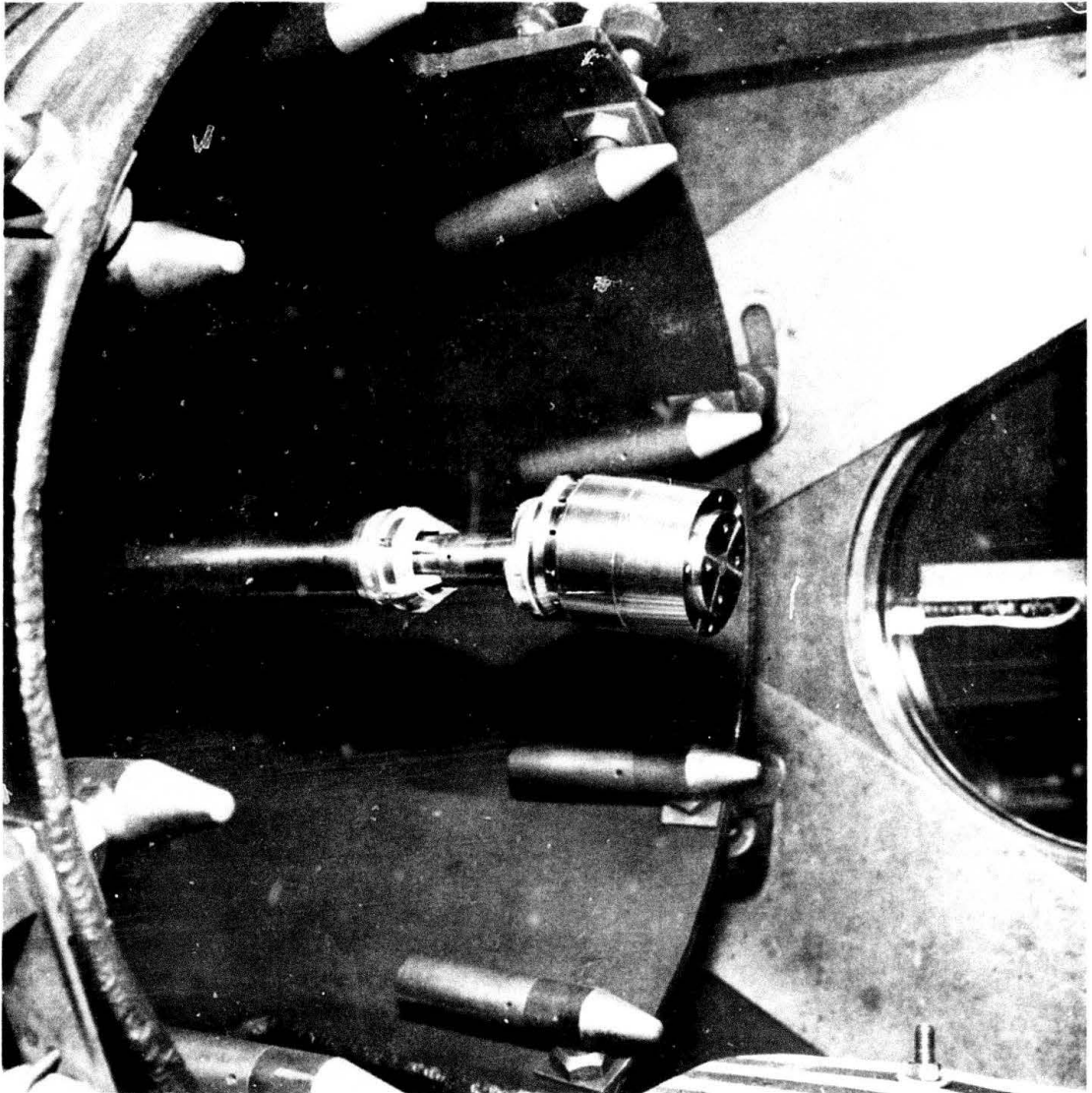


FIGURE 2 GAS BEARING ASSEMBLY AND READOUT.

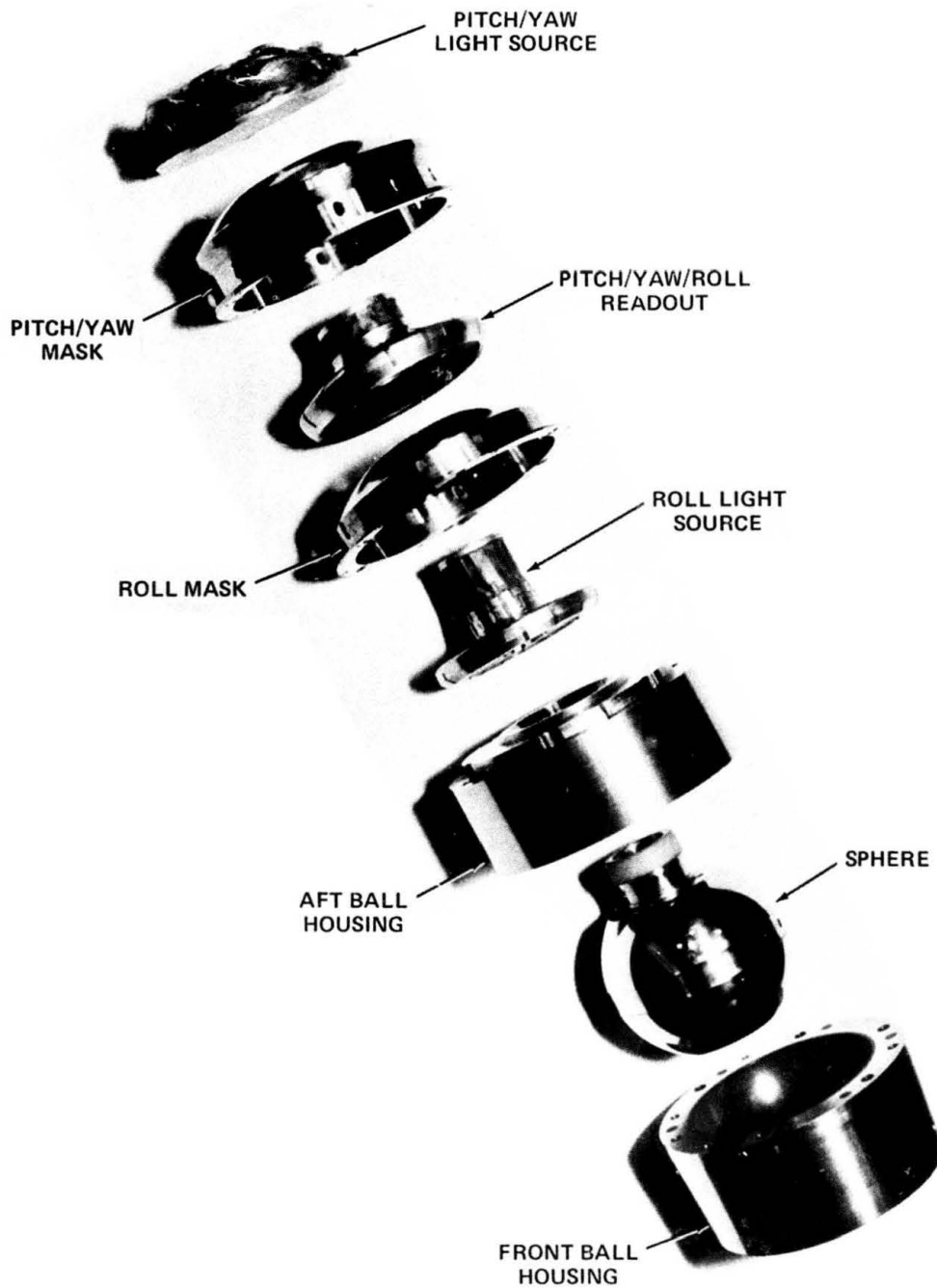


FIGURE 3 GAS BEARING ASSEMBLY/READOUT COMPONENTS.

reduction. Roll or spin rates measured using this system provided a check on the independent measurements that led to computations of the two oscillatory frequencies (see equation (11c)).

The fiber optic system readout will not be discussed in great detail since it is to be subjected to modification or replacement. In principle the fiber optic readout is fairly straightforward, although in practice fiber breakage limited the angular coverage.

The fiber optic light guides are 0.020 inch diameter. These guides are located at discrete angular positions. A light source outside of the tunnel is conducted by the guides through the sting and inside the bearing. The angles of attack (pitch) and sideslip (yaw) are read approximately every half degree; the roll angle is read every 22.5 degrees. As the model rotates a mask covers and uncovers the guides from the external light source. As a guide is uncovered the light crosses a 0.050 inch gap to enter another guide directly opposite the light-carrying-guide. The mask sheath (attached to the model to share its angular rotation) moves within this gap.

The light from the pickup guide then goes to a photocell where it is converted to an electrical signal. A total of five channels are required, two for pitch, two for yaw and one for roll. After these signals have been recorded (analog) on magnetic tape, they are digitized. The digitized signal, together with a "readout algorithm" and calibration provides the angular record, i.e. degrees (in yaw and pitch) versus time. In the next section the discussion will cover how this angular record can be used to calculate the characteristic frequencies and damping exponents and ultimately the non-dimensional aerodynamic derivatives.

Figure 4 provides a schematic of the more salient features of the bearing. It will be noted that the sting is not solid but contains various passages for the light guides as well as conduits for bearing and control air. There are five

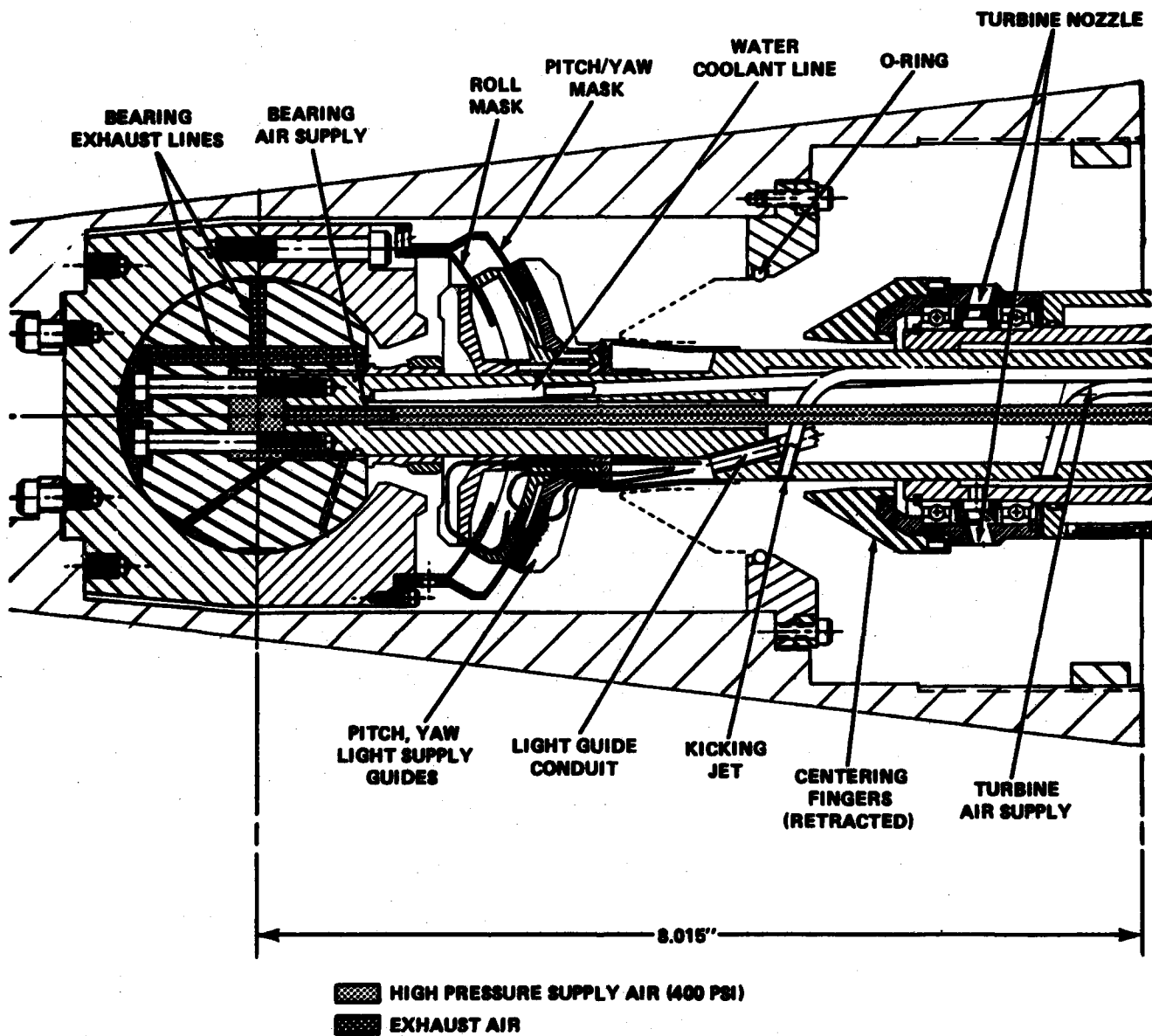


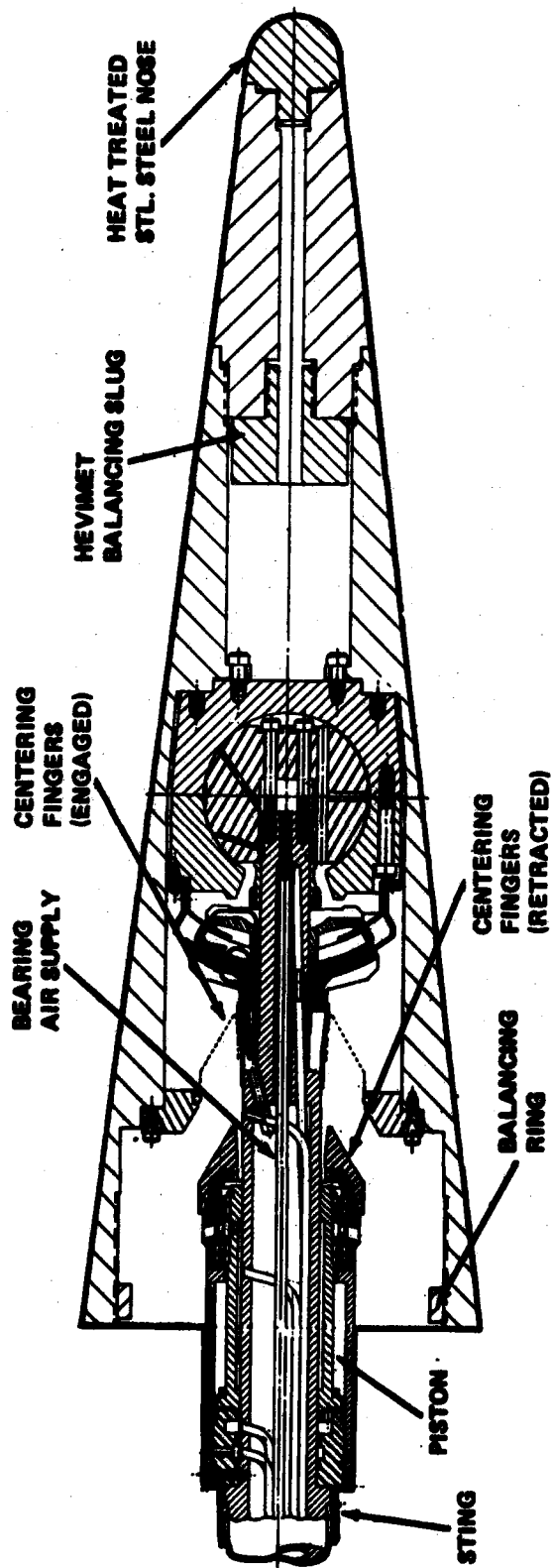
FIGURE 4 AIR BEARING SECTION.

separate air supply passages: (a) bearing, (b) kicking jet, (c) centering fingers-forward, (d) centering fingers retract, (e) turbine (see Figure 5).

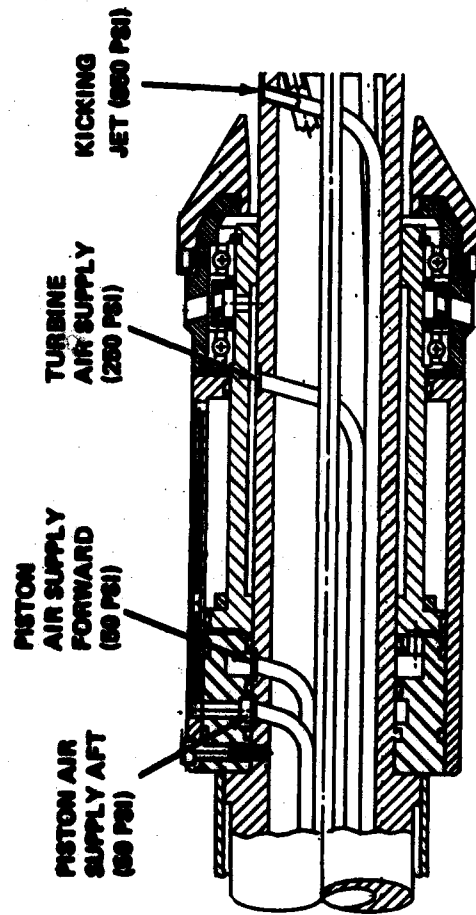
Bearing air is admitted into the sting at about 375 to 400 psi. As pointed out earlier, bearing air should be heated so that there is no significant contraction of the epoxy socket. Setting an exact temperature is not feasible, nor is it necessary: the air after expansion in the bearing must be equal to or somewhat greater than the socket temperature. The bearing air supply enters the bearing sphere as indicated and exhausts through eight holes--four forward and four aft. This air is then carried by the bearing exhaust lines in the sphere to the rear of the bearing where it enters the model interior. Bearing exhaust air passes near the fiber optic readout system, partially contributing to the cooling requirements. It will be noted that there is also water cooling provided to the readout system. The air finally exits the base of the model.

The second air source is the air jet. The air jet is simply a high pressure jet of air (about 850 psi) which when applied to one side of the model impulsively gives the model an initial disturbance in angle and angular rate. Because the model is spinning, a mechanical initiator would be unduly complicated. The air jet has been found to be an entirely reliable and effective means for initiating model motion.

The third and fourth air supplies move the piston and the centering fingers forward and aft. Air at about 50 psi enters the base through the conduit indicated in Figure 5a (and the enlargement in Figure 5b). The piston moves forward, forcing the centering fingers into the O-ring. The turbine then imparts spin to the model while at the same time holding the model at null in both orthogonal aerodynamic angles. When the desired spin rate is achieved, air is simultaneously bled from the region aft of the piston and applied to the forward piston face by the aft piston air supply. The piston and centering fingers are driven aft. The



5 (a)



5 (b)

FIGURE 5 MODEL SCHEMATIC.

model is now available for angle of attack initiation by the kicking jet described earlier.

The final air supply drives the turbine. Air is admitted to the turbine at 200 to 250 psi. The turbine does not contain blades as might be expected but rather consists of 18 equally spaced holes or nozzles drilled in the piston forming a ring around the piston. Two of these nozzles are shown in Figures 4 and 5. The axis of these nozzles are directed such that the effluent vector has a component tangential to the piston surface. When the piston is pressured in a positive direction, the centering fingers are forced against the O-ring attached to the model. Air imparted to the turbine then spins the model while at the same time holding the model's centerline directly into the wind tunnel flow vector. Once the model has been spun to the desired spin rate the fingers are retracted, turbine air supply terminated and the kicking jet initiated. At this point the model is assumed undergoing spin/yaw/pitch motion that is satisfactory for data acquisition.

Since the model must be dynamically balanced for proper angular response, there is provision for ensuring that the center of mass is at the point of rotation. Fore and aft movement of the center of mass is controlled by the location of the HEAVIMET (tungsten alloy) balancing slug seen in Figure 5. Since the model is configurationally a body of revolution, most of the components also have an axis of symmetry and are shaped on a lathe. However, internal screw holes and other irregularities can place the center of mass off the configurational axis of symmetry. Consequently a balancing ring (located at the rear of the model) can be machined in accordance with balancing machine instructions to bring the center of mass laterally to the axis of configuration symmetry.

Because the dynamic model is used in a flow environment where the stagnation temperature may be 1700 degrees Fahrenheit, prolonged usage might cause the

temperature in the vicinity of the fiber optic light guides to exceed 175 degrees Fahrenheit. Thus, water cooling is provided by a passage through the center of the sting. In the present set of tests water cooling was probably unnecessary since bearing effluent air provided sufficient cooling for the test durations (less than 60 seconds).

The preceding description covered the essentials of the model's mechanical design features. The fiber optic system functioned only intermittently and hence cinematic coverage was used for all data reduction. The only other difficulty experienced was binding (intermittent stator/rotor contact) in the gas bearing after prolonged use. This problem was alleviated by heating the bearing air to about 50 degrees over ambient. Tests for maximum sustainable loads on the gas bearing have not been made; however, it has shown the capability of sustaining a model weight of 35 pounds and an axial aerodynamic load of over 100 pounds.

3.0 DATA REDUCTION

In this section the relevant differential equation of model motion and the solution of this equation will be given. The least squares data reduction technique will be developed and the computer program, formulating this technique will be given.

3.1 DIFFERENTIAL EQUATION OF MOTION. The wind tunnel model has been indicated to undergo angular motion about three mutually perpendicular axes while immersed in a continuous newtonian medium. The situation then is similar to classical aeroballistic motion with two restrictions. In classical aeroballistics the model (or projectile) moves through an essentially stationary medium with permissible motion about and along three mutually perpendicular axes. The Galilean transformation from a moving model/stationary medium to a linear constrained model/moving medium does not change the physics of aeroballistics. However, constraining the model against linear motion does mean that only the equations of angular motion need be considered: the equations of linear motion are identically zero.

There is some controversy associated with the origins of the equations of aeroballistic motion known as "tricyclic theory." Reference (1) is often considered the seminal paper in the statement of the tricyclic theory; reference (2) is also a broad statement of the theory and contains many extensions and applications to the ballistic range. However, a possibly more readable paper than either of these and one that will be used here as the basic reference is reference (3) by H. R. Vaughn.

¹ Nicolliades, J.D., "On the Free Flight Motion of Missiles Having Slight Configurational Asymmetries," Ballistic Research Laboratories Report No. 858, June 1953.

² Murphy, C.H., "Free Flight Motion of Symmetric Missiles," Ballistic Research Laboratories Report No. 1216, July 1963.

³ Vaughn, H.R., "A Detailed Development of the Tricyclic Theory," Sandia Laboratories, SC-M-67-2933, February 1968.

Relying on the development contained in reference (3) it is possible to show that the angular motion about two orthogonal and wind tunnel-fixed axes is described by the equations:

$$\begin{aligned} I\ddot{\alpha} - p\dot{\beta}I_x - M_{\alpha}\dot{\alpha} - (M_{\alpha}^* + M_q)\dot{\alpha} - M_{\delta}\delta \cos pt - M_{p\beta}p\beta &= 0 \\ I\ddot{\beta} + p\dot{\alpha}I_x + N_{\beta}\dot{\beta} - (N_r - N_{\dot{\beta}})\dot{\beta} - M_{\delta}\delta \sin pt - N_{p\alpha}p\alpha &= 0 \end{aligned} \quad (1)$$

In the above equation, α and β are the angular deviation of the model's axis of symmetry (or principal axis of inertia) from the velocity vector: α measures deviation in the vertical plane and β deviation in the horizontal plane. Figure 6 indicates the measurement of these angles. Since the maximum excursions in α and β are limited to less than 7 degrees, any ambiguities due to commutivity of angular rotations may be ignored.

Table 1 below defines the various symbols appearing in equations (1).

TABLE 1 M_{α} EQUATION (1) SYMBOL DEFINITION

SYMBOL	COEFFICIENT	DEFINITION
M_{α}	$C_{m\alpha} = M_{\alpha} / (\bar{q}cd)$	Pitching moment derivative
M_{β}	$C_{m\beta} = M_{\beta} / (\bar{q}cd)$	Yawing moment derivative
M_q	$C_{mq} = M_q / (\bar{q}cd^2/2V)$	Pitch damping derivative
M_r	$C_{mr} = M_r / (\bar{q}cd^2/2V)$	Yaw damping derivative
$M_{p\alpha}$	$C_{m_{p\alpha}} = M_{p\alpha} / (\bar{q}cd^2/2V)$	Yaw Magnus derivative
$M_{p\beta}$	$C_{m_{p\beta}} = M_{p\beta} / (\bar{q}cd^2/2V)$	Pitch Magnus derivative
M_{δ}	$C_{m_{\delta}} = M_{\delta} / (\bar{q}cd)$	Trim moment derivative
δ	---	Equivalent trim off-set angle
I	---	Transverse moment of inertia
I_x	---	Roll moment of inertia

³ See Footnote 3 on page 19.

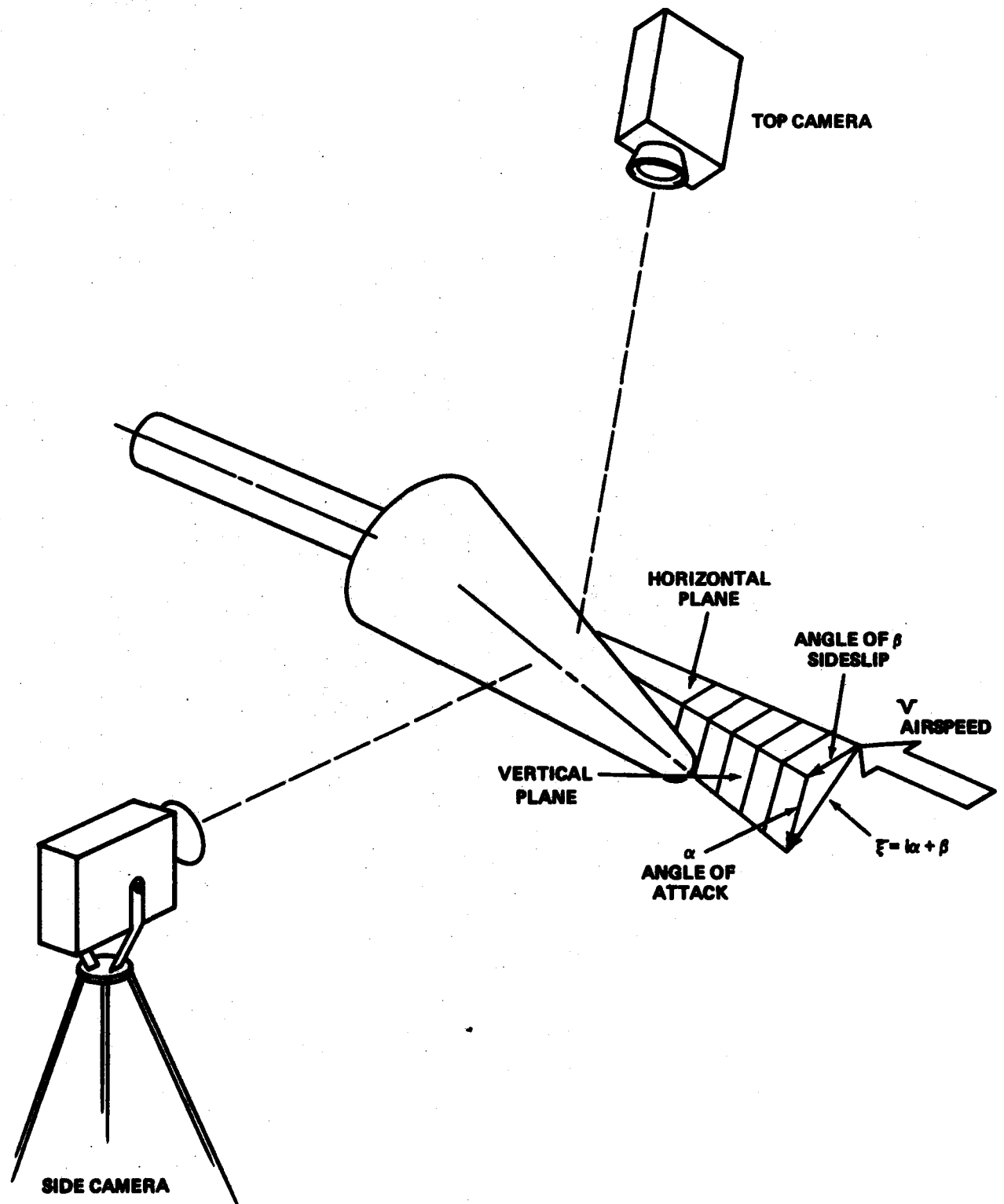


FIGURE 6 ORTHOGONAL CAMERA COVERAGE OF MODEL MOTION.

If equation (1) is assumed linear in angle of attack, α , and sideslip, β and the spin rate, p , is constant, then various formalisms are available to effect a solution. One approach might be to reduce the differential equation to an algebraic equation through the Laplace Transform. If the existence of rotational symmetry of the model is accepted the consequence is a set of relationships among the derivatives of Table 1 (and equations (1)) as:

$$\begin{aligned} M_{\alpha} &= N_{\beta} \\ M_q &= N_r \\ M_{\alpha} &= -N_{\beta} \\ M_{p\beta} &= N_{p\alpha} \end{aligned} \quad (2)$$

The procedure taken here to solve equations (1) is not to use the Laplace Transform but rather to remain in the time domain. First, equations (1) may be combined by introducing the complex angle of attack, ξ , as

$$\xi = i\alpha + \beta \quad (3)$$

Equations (1) can now be expressed as a single differential equation in the complex variable, ξ , as:

$$\ddot{\xi} + \left[-ip \left(\frac{I_x}{I} \right) - \frac{M_q + M_{\dot{\alpha}}}{I} \right] \dot{\xi} + \left[-ip \frac{M_{p\beta}}{I} - \frac{M_{\alpha}}{I} \right] \xi - \frac{M_{\delta}}{I} \left(-\sin pt + i \cos pt \right) \delta = 0 \quad (4)$$

After some protracted analysis, the solution of equation (4) takes the form,

$$\xi = k_1 e^{(\lambda_1 + i\omega_1)t} + k_2 e^{(\lambda_2 + i\omega_2)t} + k_3 e^{ipt} \quad (5)$$

where the three additive terms on the right might be described as vectors (or "arms") in the complex plane. The arms rotate at frequencies ω_1 (nutation), ω_2 (precession) and p (spin rate). Because of the real terms in the exponents of first two arms (nutation and precession respectively) these arms also diminish or grow depending upon the sign of λ_1 and λ_2 . Since k_1 , k_2 and k_3 are complex, each will in general contain two real constants. Thus, writing the equivalent of equation (5) in real variables, α and β , we would expect six unspecified

constants. In addition, of course, there are the two damping terms λ_1 and λ_2 and the two frequency terms ω_1 and ω_2 . (The spin rate, p , will be treated as a measurable quantity.) Writing equation (5) as two real equations gives,

$$\alpha = (A_1 \cos \omega_1 t + B_1 \sin \omega_1 t)e^{\lambda_1 t} + (A_2 \cos \omega_2 t + B_2 \sin \omega_2 t)e^{\lambda_2 t} + (A_3 \cos pt + B_3 \sin pt) \quad (6a)$$

$$\beta = (B_1 \cos \omega_1 t - A_1 \sin \omega_1 t)e^{\lambda_1 t} + (B_2 \cos \omega_2 t - A_2 \sin \omega_2 t)e^{\lambda_2 t} + (B_3 \cos pt - A_3 \sin pt) \quad (6b)$$

It then appears that a data reduction scheme will require the record of angular displacements α and β to be "fitted" in some way to provide numerical values of the ten constants: $A_1, B_1, A_2, B_2, A_3, B_3, \lambda_1, \lambda_2, \omega_1, \omega_2$.

In spite of the requirement of evaluating ten constants only four, $\lambda_1, \lambda_2, \omega_1, \omega_2$ have any practical value in the evaluation of the aerodynamic derivatives. The first four constants A_1, B_1, A_2, B_2 contain in addition to the stability derivatives, initial conditions in the variables $\alpha, \dot{\alpha}, \beta, \dot{\beta}$ at whatever point (in time) the $\alpha(t), \beta(t)$ record is begun. Since it is not practical to evaluate precisely the above mentioned initial conditions, the constants A_1, B_1, A_2, B_2 have no utility in establishing the stability derivatives. For example, A_1 may be written as,

$$A_1 = \left[\frac{[\dot{\alpha}_0 - \lambda_2 \alpha_0 - \omega_2 \beta_0 + \lambda_2 A_3 - (p - \omega_2) B_2](\lambda_1 - \lambda_2)}{(\omega_1 - \omega_2)^2 + (\lambda_1 - \lambda_2)^2} \right] \quad (7)$$

The dependence upon initial conditions $\dot{\alpha}_0, \alpha_0$ is clear. Similar relationship might be written for B_1, A_2, B_2 ; A_3 and B_3 are expressions for configurational asymmetries.

The frequency and damping terms $\omega_1, \omega_2, \lambda_1, \lambda_2$ are the constants of interest since they contain all the aerodynamic stability derivatives except the asymmetry

moment, M_δ . First define the two parameters, s , and τ :

$$s = \frac{\left(\frac{pI_x}{2I}\right)^2}{\left(\frac{M_\alpha}{I}\right)} \quad (8)$$

$$\tau = \frac{1}{\sqrt{1 - \frac{1}{s}}} = \frac{\left(\frac{pI_x}{2I}\right)}{\sqrt{\left(\frac{pI_x}{2I}\right)^2 - \frac{M_\alpha}{I}}} \quad (9)$$

The parameter, s , is called the "gyroscopic stability factor" and is a measure of the relative presence of aerodynamic stiffness, M_α/I , and gyroscopic stiffness, $(pI_x/2I)$. For our purposes the parameter, τ , will be used to convey essentially the same information, i.e. the relative importance of spin or gyroscopic effects to aerodynamic effects. It should be noted that for statically stable missiles (center of pressure aft of center of gravity) the stability derivative, M_α , in equation (9) is negative. Thus τ must always be real. Further note the asymptotic values of τ with spin rate, p .

$$\lim_{p \rightarrow 0} \tau \rightarrow 0$$

$$p \rightarrow 0$$

$$\lim_{p \rightarrow \infty} \tau \rightarrow 1$$

$$p \rightarrow \infty$$

Using the parameter, τ , it is easy to show

$$\omega_1 = \frac{pI_x}{2I} \left(1 + \frac{1}{\tau}\right) \quad (10a)$$

$$\omega_2 = \frac{pI_x}{2I} \left(1 - \frac{1}{\tau}\right) \quad (10b)$$

$$\lambda_1 = \frac{M_\alpha}{2I} (1 + \tau) + \left(\frac{M_\alpha p \beta}{I_x}\right) \tau \quad (10c)$$

$$\lambda_2 = \frac{M_q}{2I} (1 - \tau) - \left(\frac{M_{p\beta}}{I_x} \right) \tau \quad (10d)$$

Also it is important to realize that the sign of τ is that of spin rate, p . Assuming that p is positive it is clear from equation (10a,b) that ω_1 is positive and ω_2 is negative; further, the magnitude of ω_1 is greater than that of ω_2 . Under conditions of positive, p , the greater frequency is ω_1 and identified as nutation and the lesser frequency is ω_2 and identified as precession. In the data to be given, the spin rate is negative with the result that the nutational frequency is negative and the precessional frequency is positive. Regardless of the sign, the frequency having the greater magnitude is the nutation, while the frequency having the lesser magnitude is the precessional.

Equations (10) present the four constants ω_1 , ω_2 , λ_1 , λ_2 in terms of the aerodynamic derivatives M_α , M_q and $M_{p\beta}$ and the spin rate, p (through the parameter, τ). It is relatively straightforward to evaluate the terms M_α , M_q , $M_{p\beta}$ and p (and τ) in terms of the four constants ω_1 , ω_2 , λ_1 , λ_2 . Multiplying equations (10a,b) together and using equation (9) gives:

$$M_\alpha = -I\omega_1\omega_2 \quad (11a)$$

Next adding equations (10c,d) provides:

$$M_q = I(\lambda_1 + \lambda_2) \quad (11b)$$

Equations (10a,b) may then be added to give:

$$p = \frac{I}{I_x} (\omega_1 + \omega_2) \quad (11c)$$

Next subtract equation (10b) from (10a) and using (11c) above gives:

$$\tau = \frac{\omega_1 + \omega_2}{\omega_1 - \omega_2} \quad (11d)$$

If equation (10d) is subtracted from (10c) and equation (11b) is used, the result is:

$$\lambda_1 - \lambda_2 = (\lambda_1 + \lambda_2)\tau + \frac{M_{p\beta}}{I} (2\tau)$$

Next replacing τ from equation (11d) gives after some manipulation:

$$M_{p\beta} = - \left[\frac{\lambda_1 \omega_2 + \lambda_2 \omega_1}{\omega_1 + \omega_2} \right] I_x \quad (11e)$$

Thus equations (11a,b,e) provide a means for calculating the dimensional aerodynamic derivatives M_α , M_q , $M_{p\beta}$ from the four constants ω_1 , ω_2 , λ_1 , λ_2 . In addition it will be noted that the spin rate, p , may be calculated from the reduced data. The conclusion that spin rate need not be measured is a bit misleading: a good estimate of spin rate is quite helpful in initiating parameter estimation during data reduction. After the data reduction process has converged a measured spin rate and a computed spin rate from equation (11c) will indicate by their agreement a check on the validity of the reduced data.

It will be noted in equation (11c) that if the spin rate, p , is zero that

$$\omega_1 = -\omega_2 = \omega$$

and if $p = 0$, then $\tau = 0$; it follows from equations (10c,d) that:

$$\lambda_1 = \lambda_2 = \lambda$$

Consequently equations (11a,b,e) become:

$$M_\alpha = -I\omega^2 \quad (12a)$$

$$M_q = 2I\lambda \quad (12b)$$

$$M_{p\beta} = \text{INDETERMINATE} \quad (12c)$$

Equation (12c) indicates that in the absence of spin rate, p , equation (11e) takes on an indeterminate form. It should be appreciated that $M_{p\beta}$, the Magnus derivative, is dependent upon configuration and not upon spin rate. However, in the absence of spin it is impossible to measure the Magnus derivative.

If the motion of the model is dynamically stable, then $\lambda_1, \lambda_2 < 0$, i.e. both the nutational and precessional damping exponents must be negative. Hence, at large values of time, equations (6) become,

$$\alpha_{\infty} = A_3 \cos pt + B_3 \sin pt \quad (13a)$$

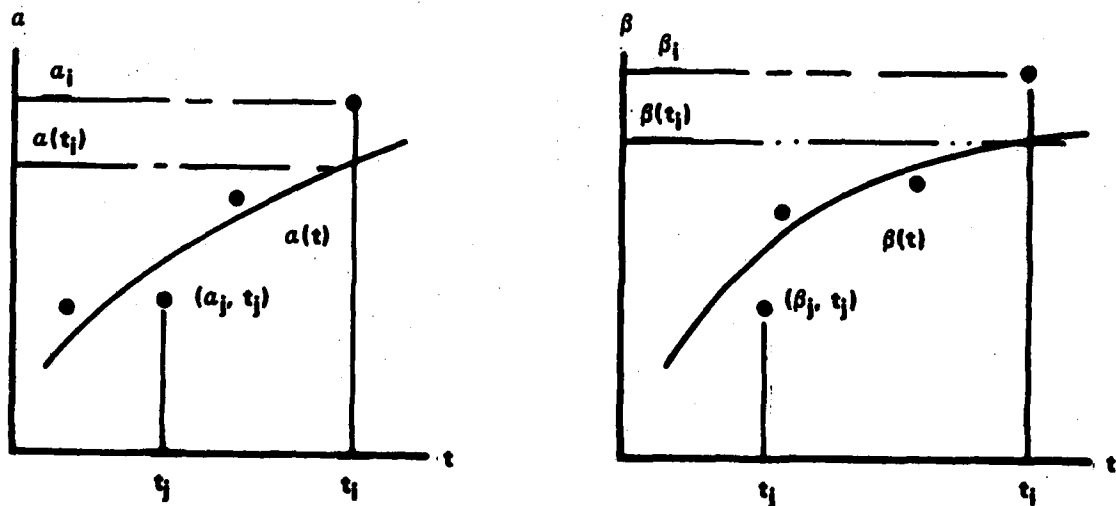
$$\beta_{\infty} = B_3 \cos pt - A_3 \sin pt \quad (13b)$$

Assuming that the angles α_{∞} and β_{∞} are small, it is justifiable to square both sides of the equations (13), add, and finally take the root to give:

$$\alpha_T = \sqrt{\alpha_{\infty}^2 + \beta_{\infty}^2} = \sqrt{A_3^2 + B_3^2} \quad (14)$$

where α_T is the trim angle of attack. Thus the constants A_3 and B_3 will provide an indication of configurational asymmetries causing a non-zero trim angle.

3.2 DATA REDUCTION EQUATIONS. The basis of the data reduction method is a variation of the familiar least squares technique.⁴ In the sketch below on the



⁴Nielsen, Kaj L., Methods in Numerical Analysis, 2nd Edition (New York: The Macmillan Co., 1964), pp. 309-313.

left is shown a series of angle of attack measurements and the corresponding value of time. The function $\alpha(t)$ is the best-fitted function (of the assumed form) to the succession of data points (α_1, t_1) . The fit is "best" in the least-squares sense. In other words for each data point (α_1, t_1) there is a "residual" which for the angle of attack is designated by r_1 . Similar remarks apply to the angle of sideslip, β , shown to the right in the above sketch. The residual or the difference between the assumed best-fit function and data point at the same time is indicated by the variable, q_1 . Thus we may express analytically the residuals r_1 and q_1 as,

$$r_1 = \alpha(t_1; A_1, B_1, A_2, B_2, A_3, B_3, \omega_1, \omega_2, \lambda_1, \lambda_2) - \alpha_1 \quad (15a)$$

$$q_1 = \beta(t_1; A_1, B_1, A_2, B_2, A_3, B_3, \omega_1, \omega_2, \lambda_1, \lambda_2) - \beta_1 \quad (15b)$$

The residual is shown as the difference between the fitted curve and the data point at the time $t = t_1$. The residuals r_1 and q_1 are shown to depend upon the ten parameters A_1, \dots, λ_2 . The heart of the least squares technique then is the method for establishing ten linearly independent equations for the determination of these ten constants. These equations are established by minimizing the sum of the squares of the residuals with respect to each of the ten constants. Since there are two variables i.e. α and β , the quantity to be minimized is the sum of each of the residuals squared as,

$$\sum_1 r_1^2 + \sum_1 q_1^2 \equiv \sum_1 (r_1^2 + q_1^2) \quad (16)$$

Then the derivative of the above quantity is taken in turn with respect to each of the ten constants A_1, \dots, λ_2 ; these derivatives are each set equal to zero to provide ten independent algebraic equations that can be solved simultaneously for each of the ten constants. For example for the A_1 and B_1 constants, the derivative operation will be:

$$\frac{\partial}{\partial A_1} \sum_1 [r_1^2 + q_1^2] = 0 \quad (17a)$$

$$\frac{\partial}{\partial B_1} \sum_i \left(r_i^2 + q_i^2 \right) = 0 \quad (17b)$$

If the analytic expression for model motion were linear in all ten of the constants, the ten equations which follow from the differentiation (see equations (17)) might be solved as linear algebraic equations. A glance at equations (6) shows that six constants A_1 , B_1 , A_2 , B_2 , A_3 and B_3 do vary linearly. However, the four remaining constants ω_1 , ω_2 , λ_1 , λ_2 do not vary linearly: ω_1 , ω_2 are arguments of transcendental functions and λ_1 , λ_2 are arguments of exponential functions. Thus, the direct method of least squares must be extended to an iterative method known as "differential corrections."

The residuals have been designated in equation (15); the functions $\alpha(t)$ and $\beta(t)$ given in these residual expressions can be expanded in a Taylor series in the constants ω_1 , ω_2 , λ_1 , λ_2 . The remaining six constants, A_1 , B_1 , A_2 , B_2 , A_3 , B_3 could also be evaluated by this iterative differential corrections procedure, but since the residuals vary linearly with these six constants, the more direct least squares procedure will be used in their evaluation. The least squares method will be covered in more detail after the differential corrections method has been described. Replacing $\alpha(t)$ and $\beta(t)$ in equations (15) by a Taylor expansion in each of the variables ω_1 , ω_2 , λ_1 , λ_2 gives:

$$\begin{aligned} r_1 = & \alpha(t_1; \bar{A}_1, \bar{B}_1, \dots, \bar{\omega}_1, \bar{\omega}_2, \bar{\lambda}_1, \bar{\lambda}_2) \\ & + \frac{\partial \alpha}{\partial \omega_1} \omega_1 + \frac{\partial \alpha}{\partial \omega_2} \omega_2 + \frac{\partial \alpha}{\partial \lambda_1} \lambda_1 + \frac{\partial \alpha}{\partial \lambda_2} \lambda_2 - \alpha_1 \end{aligned} \quad (18a)$$

$$\begin{aligned} q_1 = & \beta(t_1; \bar{A}_1, \bar{B}_1, \dots, \bar{\omega}_1, \bar{\omega}_2, \bar{\lambda}_1, \bar{\lambda}_2) \\ & + \frac{\partial \beta}{\partial \omega_1} \omega_1 + \frac{\partial \beta}{\partial \omega_2} \omega_2 + \frac{\partial \beta}{\partial \lambda_1} \lambda_1 + \frac{\partial \beta}{\partial \lambda_2} \lambda_2 - \beta_1 \end{aligned} \quad (18b)$$

where α and β have been expanded about estimated values $\bar{\omega}_1$, $\bar{\omega}_2$, $\bar{\lambda}_1$, $\bar{\lambda}_2$. The

quantities or variables ω_1 , ω_2 , λ_1 , λ_2 represent the incremental changes in the estimated values (see equation (26)).

New residuals R_1 and Q_1 may be defined as:

$$R_1 = \alpha(t_1; \bar{A}_1, \dots, \bar{\lambda}_2) - \alpha_1 = \bar{\alpha} - \alpha_1 \quad (19a)$$

$$Q_1 = \beta(t_1; \bar{A}_1, \dots, \bar{\lambda}_2) - \beta_1 = \bar{\beta} - \beta_1 \quad (19b)$$

The residuals R_1 and Q_1 are recognized as the difference between the estimated functions $\alpha(t_1; \bar{A}_1, \dots, \bar{\lambda}_2)$ and $\beta(t_1; \bar{A}_1, \dots, \bar{\lambda}_2)$ and the data points α_1 and β_1 .

Equations (18) and (19) may be combined to give:

$$r_1 = \frac{\partial \alpha}{\partial \omega_1} \omega_1 + \frac{\partial \alpha}{\partial \omega_2} \omega_2 + \frac{\partial \alpha}{\partial \lambda_1} \lambda_1 + \frac{\partial \alpha}{\partial \lambda_2} \lambda_2 + R_1 \quad (20a)$$

$$q_1 = \frac{\partial \beta}{\partial \omega_1} \omega_1 + \frac{\partial \beta}{\partial \omega_2} \omega_2 + \frac{\partial \beta}{\partial \lambda_1} \lambda_1 + \frac{\partial \beta}{\partial \lambda_2} \lambda_2 + Q_1 \quad (20b)$$

The residuals r_1 and q_1 may be squared and summed to give the quantity

$$\sum_1 (r_1^2 + q_1^2)$$

as in identity (16). Now the derivative is taken of the above sum-of-the-square of the residuals with respect to the four variables ω_1 , ω_2 , λ_1 , λ_2 and these derivatives set, in turn, equal to zero. For example the equation which results from taking the derivative with respect to ω_1 is:

$$\begin{aligned}
& \frac{\partial}{\partial \omega_1} \left[\sum_1 \left\{ \left(\frac{\partial \alpha}{\partial \omega_1} \omega_1 + \frac{\partial \alpha}{\partial \omega_2} \omega_2 + \frac{\partial \alpha}{\partial \lambda_1} \lambda_1 + \frac{\partial \alpha}{\partial \lambda_2} \lambda_2 \right)^2 \right. \right. \\
& \quad \left. \left. + \left(\frac{\partial \beta}{\partial \omega_1} \omega_1 + \frac{\partial \beta}{\partial \omega_2} \omega_2 + \frac{\partial \beta}{\partial \lambda_1} \lambda_1 + \frac{\partial \beta}{\partial \lambda_2} \lambda_2 \right)^2 \right\} \right] \\
& + 2 \frac{\partial}{\partial \omega_1} \left[\sum_1 \left(R_1 \frac{\partial \alpha}{\partial \omega_1} \omega_1 + R_1 \frac{\partial \alpha}{\partial \omega_2} \omega_2 + R_1 \frac{\partial \alpha}{\partial \lambda_1} \lambda_1 + R_1 \frac{\partial \alpha}{\partial \lambda_2} \lambda_2 \right) \right. \\
& \quad \left. + \sum_1 \left(Q_1 \frac{\partial \beta}{\partial \omega_1} \omega_1 + Q_1 \frac{\partial \beta}{\partial \omega_2} \omega_2 + Q_1 \frac{\partial \beta}{\partial \lambda_1} \lambda_1 + Q_1 \frac{\partial \beta}{\partial \lambda_2} \lambda_2 \right) \right] \\
& + \frac{\partial}{\partial \omega_1} \left[\sum_1 R_1^2 + \sum_1 Q_1^2 \right] = 0
\end{aligned} \tag{21}$$

giving,

$$\begin{aligned}
& \sum_1 \left[\left(\frac{\partial \alpha}{\partial \omega_1} \right)^2 + \left(\frac{\partial \beta}{\partial \omega_1} \right)^2 \right] \omega_1 + \sum_1 \left[\left(\frac{\partial \alpha}{\partial \omega_1} \frac{\partial \alpha}{\partial \omega_2} \right) + \left(\frac{\partial \beta}{\partial \omega_1} \frac{\partial \beta}{\partial \omega_2} \right) \right] \omega_2 \\
& + \sum_1 \left[\left(\frac{\partial \alpha}{\partial \omega_1} \frac{\partial \alpha}{\partial \lambda_1} \right) + \left(\frac{\partial \beta}{\partial \omega_1} \frac{\partial \beta}{\partial \lambda_1} \right) \right] \lambda_1 + \sum_1 \left[\left(\frac{\partial \alpha}{\partial \omega_1} \frac{\partial \alpha}{\partial \lambda_2} \right) + \left(\frac{\partial \beta}{\partial \omega_1} \frac{\partial \beta}{\partial \lambda_2} \right) \right] \lambda_2 \\
& - \sum_{i=1} \left[R_i \frac{\partial \alpha}{\partial \omega_1} + Q_i \frac{\partial \beta}{\partial \omega_1} \right]
\end{aligned} \tag{22}$$

It should be appreciated that the various partial derivatives in equation (21) such as $\partial a / \partial \omega_1$ are evaluated at the estimated values $\bar{\omega}_1, \bar{\omega}_2, \bar{\lambda}_1, \bar{\lambda}_2$ and hence are constants for any differentiation with respect to $\omega_1, \omega_2, \lambda_1, \lambda_2$.

The development of the remaining three equations is obvious. The result is that four equations linear in the variables $\omega_1, \omega_2, \lambda_1, \lambda_2$ are available for the calculation of these variables. Matrix algebra may be used to advantage in programming these equations for solution on a digital computer. Let C_j be the j th subscripted variable representing $\omega_1, \omega_2, \lambda_1, \lambda_2$ for the four consecutive subscripts as

$$\begin{vmatrix} C_1 \\ C_2 \\ C_3 \\ C_4 \end{vmatrix} = \begin{vmatrix} \omega_1 \\ \omega_2 \\ \lambda_1 \\ \lambda_2 \end{vmatrix} = C_j$$

The algebraic equation given in equation (22) and the equivalent equations for the remaining variables may be represented by the following matrix equation:

$$F_{kj} C_j = Rl_k \quad (23)$$

F_{kj} represents the coefficients of equation (23) and the equivalent equations; Rl_k contains the sum of the residuals. For example the 4×4 F_{kj} matrix has the following elemental values:

$$F_{11} = \sum_i \left[\left(\frac{\partial \alpha}{\partial \omega_1} \right)^2 + \left(\frac{\partial \beta}{\partial \omega_1} \right)^2 \right]$$

$$F_{12} = \sum_i \left[\frac{\partial \alpha}{\partial \omega_1} \frac{\partial \alpha}{\partial \omega_2} + \frac{\partial \beta}{\partial \omega_1} \frac{\partial \beta}{\partial \omega_2} \right]$$

$$F_{13} = \sum_i \left[\frac{\partial \alpha}{\partial \omega_1} \frac{\partial \alpha}{\partial \lambda_1} + \frac{\partial \beta}{\partial \omega_1} \frac{\partial \beta}{\partial \lambda_1} \right]$$

$$F_{14} = \sum_i \left[\frac{\partial \alpha}{\partial \omega_1} \frac{\partial \alpha}{\partial \lambda_2} + \frac{\partial \beta}{\partial \omega_1} \frac{\partial \beta}{\partial \lambda_2} \right]$$

$$F_{21} = \sum_i \left[\frac{\partial \alpha}{\partial \omega_2} \frac{\partial \alpha}{\partial \omega_1} + \frac{\partial \beta}{\partial \omega_2} \frac{\partial \beta}{\partial \omega_1} \right]$$

$$F_{22} = \sum_i \left[\left(\frac{\partial \alpha}{\partial \omega_2} \right)^2 + \left(\frac{\partial \beta}{\partial \omega_2} \right)^2 \right]$$

$$F_{23} = \sum_i \left[\frac{\partial \alpha}{\partial \omega_2} \frac{\partial \alpha}{\partial \lambda_1} + \frac{\partial \beta}{\partial \omega_2} \frac{\partial \beta}{\partial \lambda_1} \right]$$

$$F_{24} = \sum_i \left[\frac{\partial \alpha}{\partial \omega_2} \frac{\partial \alpha}{\partial \lambda_2} + \frac{\partial \beta}{\partial \omega_2} \frac{\partial \beta}{\partial \lambda_2} \right]$$

$$F_{31} = \sum_i \left[\frac{\partial \alpha}{\partial \lambda_1} \frac{\partial \alpha}{\partial \omega_1} + \frac{\partial \beta}{\partial \lambda_1} \frac{\partial \beta}{\partial \omega_1} \right]$$

$$F_{32} = \sum_i \left[\frac{\partial \alpha}{\partial \lambda_1} \frac{\partial \alpha}{\partial \omega_2} + \frac{\partial \beta}{\partial \lambda_1} \frac{\partial \beta}{\partial \omega_2} \right]$$

$$F_{33} = \sum_i \left[\left(\frac{\partial \alpha}{\partial \lambda_1} \right)^2 + \left(\frac{\partial \beta}{\partial \lambda_1} \right)^2 \right]$$

$$F_{34} = \sum_i \left[\frac{\partial \alpha}{\partial \lambda_1} \frac{\partial \alpha}{\partial \lambda_2} + \frac{\partial \beta}{\partial \lambda_1} \frac{\partial \beta}{\partial \lambda_2} \right]$$

$$F_{41} = \sum_i \left[\frac{\partial \alpha}{\partial \lambda_2} \frac{\partial \alpha}{\partial \omega_1} + \frac{\partial \beta}{\partial \lambda_2} \frac{\partial \beta}{\partial \omega_1} \right]$$

$$F_{42} = \sum_i \left[\frac{\partial \alpha}{\partial \lambda_2} \frac{\partial \alpha}{\partial \omega_2} + \frac{\partial \beta}{\partial \lambda_2} \frac{\partial \beta}{\partial \omega_2} \right]$$

$$\begin{aligned}
 F_{43} &= \sum_i \left[\frac{\partial \alpha}{\partial \lambda_2} \frac{\partial \alpha}{\partial \lambda_1} + \frac{\partial \beta}{\partial \lambda_2} \frac{\partial \beta}{\partial \lambda_1} \right] \\
 F_{44} &= \sum_i \left[\left(\frac{\partial \alpha}{\partial \lambda_2} \right)^2 + \left(\frac{\partial \beta}{\partial \lambda_2} \right)^2 \right]
 \end{aligned} \tag{24a}$$

The residual term Rl_k may be written as

$$\begin{aligned}
 Rl_1 &= \sum_i \left[\frac{\partial \alpha}{\partial \omega_1} R_i + \frac{\partial \beta}{\partial \omega_1} Q_i \right] \\
 Rl_2 &= \sum_i \left[\frac{\partial \alpha}{\partial \omega_2} R_i + \frac{\partial \beta}{\partial \omega_2} Q_i \right] \\
 Rl_3 &= \sum_i \left[\frac{\partial \alpha}{\partial \lambda_1} R_i + \frac{\partial \beta}{\partial \lambda_1} Q_i \right] \\
 Rl_k &= \sum_i \left[\frac{\partial \alpha}{\partial \lambda_2} R_i + \frac{\partial \beta}{\partial \lambda_2} Q_i \right]
 \end{aligned} \tag{24b}$$

Equations (26) may be treated as a matrix equation and a solution for C_j may be indicated the inverse formalism:

$$\begin{bmatrix} \omega_1 \\ \omega_2 \\ \lambda_1 \\ \lambda_2 \end{bmatrix} \equiv C_j = (F_{kj})^{-1} Rl_k = Fl_{jk} Rl_k \tag{25}$$

For most applications the matrix F_{kj} is not singular so the inverse exists.

However this matrix is not orthogonal so the inverse has been indicated as Fl_{jk} .

Once the variables ω_1 , ω_2 , λ_1 , λ_2 have been obtained a new estimate on these variables can be made as

$$\begin{aligned}
 \bar{\omega}_1 + \omega_1 &\rightarrow \bar{\omega}_1 \\
 \bar{\omega}_2 + \omega_2 &\rightarrow \bar{\omega}_2 \\
 \bar{\lambda}_1 + \lambda_1 &\rightarrow \bar{\lambda}_1 \\
 \bar{\lambda}_2 + \lambda_2 &\rightarrow \bar{\lambda}_2
 \end{aligned} \tag{26}$$

In other words the new estimates of the variables shown on the right hand side are formed by adding algebraically the incremental variables to the present estimates. After each iteration new estimates become available; these new estimates are used to reevaluate the various derivatives appearing in the elements of the F_{kj} and Rl_j matrices (see equations (24)). After a sufficient number of iterations a "best estimate" (in the least-square sense) is available for the variables $\omega_1, \omega_2, \lambda_1, \lambda_2$. Obviously selecting the number of iterations is arbitrary. However, the probable error of fit, E , can be used as an index of convergence. E may be given as:

$$E = 0.6745 \left[\sum_1 \frac{(R_1^2 + Q_1^2)}{(2N - n)} \right]^{\frac{1}{2}} \quad (27)$$

where N is the total number of data points to be fitted and n is the number of parameters. In the case under discussion n is obviously equal to four.

The derivatives of α and β with respect to the four parameters $\omega_1, \omega_2, \lambda_1, \lambda_2$ have not been defined. However these derivatives are easy to form. From equation (6) the eight required derivatives are:

$$\frac{\partial \alpha}{\partial \omega_1} = (t)(B_1 \cos \omega_1 t - A_1 \sin \omega_1 t)e^{\lambda_1 t} \quad (28a)$$

$$\frac{\partial \alpha}{\partial \omega_2} = (t)(B_2 \cos \omega_2 t - A_2 \sin \omega_2 t)e^{\lambda_2 t} \quad (28b)$$

$$\frac{\partial \alpha}{\partial \lambda_1} = (t)(A_1 \cos \omega_1 t + B_1 \sin \omega_1 t)e^{\lambda_1 t} \quad (28c)$$

$$\frac{\partial \alpha}{\partial \lambda_2} = (t)(A_2 \cos \omega_2 t + B_2 \sin \omega_2 t)e^{\lambda_2 t} \quad (28d)$$

$$\frac{\partial \beta}{\partial \omega_1} = (-t)(B_1 \sin \omega_1 t + A_1 \cos \omega_1 t)e^{\lambda_1 t} \quad (28e)$$

$$\frac{\partial \beta}{\partial \omega_2} = (-t)(B_2 \sin \omega_2 t + A_2 \cos \omega_2 t)e^{\lambda_2 t} \quad (28f)$$

$$\frac{\partial \beta}{\partial \lambda_1} = (t)(B_1 \cos \omega_1 t - A_1 \sin \omega_1 t)e^{\lambda_1 t} \quad (28g)$$

$$\frac{\partial \beta}{\partial \lambda_2} = (t)(B_2 \cos \omega_2 t - A_2 \sin \omega_2 t)e^{\lambda_2 t} \quad (28h)$$

Once a set of values for ω_1 , ω_2 , λ_1 , λ_2 emerge from the data reduction process, it is possible to calculate the aerodynamic derivatives and spin rate from equations (11a,b,c,e).

The remaining question concerns the evaluation of the six constants A_1 , B_1 , A_2 , B_2 , A_3 , B_3 , which up to now have been assumed available. As pointed out earlier these six constants must be evaluated to complete the fit of equations (6) to the data even though such constants (with the exception of A_3 and B_3) contain no new aerodynamic data. It will be noted in equation (6) that the angle of attack, α , and side slip, β , are linear functions of the constants A_1 , B_1 , A_2 , B_2 , A_3 , B_3 ; hence the direct least squares technique can be applied rather than the iterative differential correction method just developed for the computation of ω_1 , ω_2 , λ_1 , λ_2 .

As before (in equation (15)) we may write for the residuals

$$r_1 = \alpha(t) - \alpha_1$$

$$q_1 = \beta(t) - \beta_1$$

where $\alpha(t)$ and $\beta(t)$ are the functions given in equation (6) and α_1 and β_1 are the data points at time $t=t_1$. The functions $\alpha(t)$ and $\beta(t)$ are also evaluated at time $t=t_1$. Of course at this point $\alpha(t)$ and $\beta(t)$ cannot be numerically evaluated because A_1 , B_1 , A_2 , B_2 , A_3 , B_3 have not been assigned numerical values although the remaining four constants, ω_1 , ω_2 , λ_1 , λ_2 have been given estimated values. Now if

the residuals are squared and added the derivative of the resulting expression may be taken in turn with respect to each of the unknowns $A_1, B_1, A_2, B_2, A_3, B_3$ to provide six independent equations for the evaluation of the unknowns.

It will be noted in equations (6) that the coefficients of the unknowns $A_1, B_1, A_2, B_2, A_3, B_3$ are the derivatives of α and β with respect to these unknowns. Thus equation (6) might be written as

$$\alpha = \left(\frac{\partial \alpha}{\partial A_1} \right) A_1 + \left(\frac{\partial \alpha}{\partial B_1} \right) B_1 + \left(\frac{\partial \alpha}{\partial A_2} \right) A_2 + \left(\frac{\partial \alpha}{\partial B_2} \right) B_2 + \left(\frac{\partial \alpha}{\partial A_3} \right) A_3 + \left(\frac{\partial \alpha}{\partial B_3} \right) B_3 \quad (29a)$$

$$\beta = \left(\frac{\partial \beta}{\partial A_1} \right) A_1 + \left(\frac{\partial \beta}{\partial B_1} \right) B_1 + \left(\frac{\partial \beta}{\partial A_2} \right) A_2 + \left(\frac{\partial \beta}{\partial B_2} \right) B_2 + \left(\frac{\partial \beta}{\partial A_3} \right) A_3 + \left(\frac{\partial \beta}{\partial B_3} \right) B_3 \quad (29b)$$

where the derivatives are given below as :

$$\begin{aligned} \frac{\partial \alpha}{\partial A_1} &= \cos(\omega_1 t) e^{\lambda_1 t} & \frac{\partial \beta}{\partial A_1} &= (-1) \sin(\omega_1 t) e^{\lambda_1 t} \\ \frac{\partial \alpha}{\partial B_1} &= \sin(\omega_1 t) e^{\lambda_1 t} & \frac{\partial \beta}{\partial B_1} &= \cos(\omega_1 t) e^{\lambda_1 t} \\ \frac{\partial \alpha}{\partial A_2} &= \cos(\omega_2 t) e^{\lambda_2 t} & \frac{\partial \beta}{\partial A_2} &= (-1) \sin(\omega_2 t) e^{\lambda_2 t} \\ \frac{\partial \alpha}{\partial B_2} &= \sin(\omega_2 t) e^{\lambda_2 t} & \frac{\partial \beta}{\partial B_2} &= \cos(\omega_2 t) e^{\lambda_2 t} \\ \frac{\partial \alpha}{\partial A_3} &= \cos(pt) & \frac{\partial \beta}{\partial A_3} &= -\sin(pt) \\ \frac{\partial \alpha}{\partial B_3} &= \sin(pt) & \frac{\partial \beta}{\partial B_3} &= \cos(pt) \end{aligned} \quad (30)$$

The residuals may be summed over the data points to give:

$$\sum_1 \left[r_1^2 + q_1^2 \right] = \sum_1 \left[\left(\alpha(t) - \alpha_1 \right)^2 + \left(\beta(t) - \beta_1 \right)^2 \right] \quad (31)$$

Six linearly independent algebraic equations may now be obtained by taking the derivative of the above residual sum with respect to each of the parameters $A_1, B_1,$

A_2, B_2, A_3, B_3 and then setting to zero. As an example the derivative of the above identity with respect to A_1 is:

$$\frac{\partial}{\partial A_1} \left\{ \sum_i \left[\left[\alpha(t) - \alpha_i \right]^2 + \left[\beta(t) - \beta_i \right]^2 \right] \right\} = 0 \quad (32a)$$

Rewriting slightly using equation (29) gives:

$$\frac{\partial}{\partial A_1} \left\{ \sum_i \left[\left[\frac{\partial \alpha}{\partial A_1} A_1 + \dots + \frac{\partial \alpha}{\partial B_3} B_3 - \alpha_i \right]^2 + \sum_i \left[\left[\frac{\partial \beta}{\partial A_1} A_1 + \dots + \frac{\partial \beta}{\partial B_3} B_3 - \beta_i \right]^2 \right] \right\} = 0 \quad (32b)$$

Carrying out the differentiation gives,

$$\sum_i \left[\frac{\partial \alpha}{\partial A_1} A_1 + \dots + \frac{\partial \alpha}{\partial B_3} B_3 \right] \left(\frac{\partial \alpha}{\partial A_1} \right) + \sum_i \left[\frac{\partial \beta}{\partial A_1} A_1 + \dots + \frac{\partial \beta}{\partial B_3} B_3 \right] \left(\frac{\partial \beta}{\partial A_1} \right) = 0$$

Rearranging the above expression gives the first of six equations for determining the constants $A_1, B_1, A_2, B_2, A_3, B_3$.

$$\begin{aligned} A_1 \left\{ \sum_i \left[\left(\frac{\partial \alpha}{\partial A_1} \right)^2 + \left(\frac{\partial \beta}{\partial A_1} \right)^2 \right] \right\} + B_1 \left\{ \sum_i \left[\left(\frac{\partial \alpha}{\partial A_1} \right) \left(\frac{\partial \alpha}{\partial B_1} \right) + \left(\frac{\partial \beta}{\partial A_1} \right) \left(\frac{\partial \beta}{\partial B_1} \right) \right] \right\} + \dots \\ + B_3 \left\{ \sum_i \left[\left(\frac{\partial \alpha}{\partial A_1} \right) \left(\frac{\partial \alpha}{\partial B_3} \right) + \left(\frac{\partial \beta}{\partial A_1} \right) \left(\frac{\partial \beta}{\partial B_3} \right) \right] \right\} = \sum_i \left[\frac{\partial \alpha}{\partial A_1} \alpha_i + \frac{\partial \beta}{\partial A_1} \beta_i \right] \end{aligned} \quad (33)$$

The solution of the six equations for the six constants may be written as a matrix equation as:

$$G_{kj} D_j = Q1_k \quad (34)$$

The solution for the column matrix, D_j , is:

$$\begin{bmatrix} A_1 \\ B_1 \\ A_2 \\ B_2 \\ A_3 \\ B_3 \end{bmatrix} \equiv D_j = (G_{kj})^{-1} Q1_k \quad (35)$$

The matrix G_{kj} has 36 elements. Rather than writing all of these elements a typical element will be given; construction of the remaining elements should be fairly obvious. First it will be noted that the column matrix D_j has been formed by assigning numbers 1 through 6 in order to the constants $A_1, B_1, A_2, B_2, A_3, B_3$; then the element G_{mn} of the matrix G_{kj} is formed from the derivative of α with respect to the m -th variable times the derivative of α with respect to the n -th variable added to the product of the derivatives of β with respect to the same variables. For example the element where $m=3$ and $n=5$, i.e. G_{35} , the variables are A_2 and A_3 (see column matrix in equation (35)). Thus,

$$G_{35} = \sum_i \left[\frac{\partial \alpha}{\partial A_3} \frac{\partial \alpha}{\partial A_5} + \frac{\partial \beta}{\partial A_3} \frac{\partial \beta}{\partial A_5} \right] \quad (36)$$

Clearly the matrix G_{kj} is symmetric (as is the matrix F_{kj} discussed earlier in equation (23)). The matrix Ql_k follows a form identical to that for Rl_k (equations (24b)). Again if $k=4$, i.e. $D_4 = B_2$, then,

$$Ql_4 = \sum_i \left[\frac{\partial \alpha}{\partial B_2} \alpha_i + \frac{\partial \beta}{\partial B_2} \beta_i \right] \quad (37)$$

The elements of the matrix D_j can be computed by equation (35). Once D_j is available then the constants $A_1, B_1, A_2, B_2, A_3, B_3$, are also available. With the availability of these six constants it is possible to use the method of differential corrections to obtain the remaining four constants $\omega_1, \omega_2, \lambda_1, \lambda_2$. The various first order partial derivatives used in forming the elements of G_{kj} and Ql_k (see equations (30)) required a guess or estimate of the four constants $\omega_1, \omega_2, \lambda_1, \lambda_2$. The method of differential corrections is now followed to improve these estimates. The iterations continue until convergence is sufficient according to some external criterion such as that stated in equation (27).

The main features of the data reduction procedure might be reviewed in the following statements

- (a) Estimate "reasonable" values of the constants $\omega_1, \omega_2, \lambda_1, \lambda_2$.
- (b) Evaluate the derivatives given in equations (30) at each data point.
- (c) Carry out the products and summations to form the elements of the matrices G_{kj} and Ql_k .
- (d) Carry out the matrix inversion and multiplication as indicated in equation (35) to solve for $A_1, B_1, A_2, B_2, A_3, B_3$.
- (e) Evaluate the derivatives given in equations (28) at each data point.
- (f) Carry out the products and summations to form the elements of the matrices F_{kj} and Rl_k .
- (g) Carry out the matrix inversion and multiplication as indicated in equation (25) to solve for $\omega_1, \omega_2, \lambda_1, \lambda_2$.
- (h) Update (improve) the present estimates of $\omega_1, \omega_2, \lambda_1, \lambda_2$ (equations (26)).
- (i) Return to step (e) and repeat the process to step (h) either a preset number of times or until some convergence criterion is satisfied.
- (j) Return to step (a) with new estimates of $\omega_1, \omega_2, \lambda_1, \lambda_2$ from step (i) and repeat procedure until convergence satisfies some external criterion.

In the application of the method discussed in this report step (i) is omitted. In other words after the first update to the parameters $\omega_1, \omega_2, \lambda_1, \lambda_2$ has been completed an immediate return is made to step (a).

3.3 COMPUTER PROGRAM. A computer program has been written to carry out the data reduction procedure developed in the preceding section. This program has been listed in Table 2. Where appropriate equations of section 3.2 will be related to the equivalent line(s) in the program.

In lines 100 through 270 some descriptive remarks are contained; most of these remarks are a brief restatement of the last few paragraphs of section 3.2.

TABLE 2
DATA REDUCTION PROGRAM

```

00100 REN THIS PROGRAM IS A DATA REDUCTION PROCEDURE BASED UPON
00110 REN LEAST SQUARES/DIFFERENTIAL CORRECTIONS FOR EVALUATING THE
00120 REN TEN CONSTANTS DESCRIBING ROLL-PITCH-YAW MOTION MEASURED IN
00130 REN THE WIND TUNNEL USING THE THREE-D GAS BEARING. THESE CONSTANTS
00140 REN ARE (A) CONSTANTS OF INTEGRATION A1,B1,A2,B2; (B) ASYMMETRY
00150 REN CONSTANTS A3,B3; (C) NUTATION/PRECESSION FREQUENCY
00160 REN CONSTANTS U3,U4; (D) NUTATION/PRECESSION DAMPING CONSTANTS
00170 REN L3,L4. I1,AND I2 ARE THE LONGITUDINAL AND TRANSVERSE MOMENTS
00180 REN OF INERTIA AND P IS THE SPIN RATE. L1 AND L2 ARE THE
00190 REN STARTING AND ENDING DATA POINT NUMBERS. VARIABLES
00200 REN U3,U4,L3,L4 ARE FITTED BY DIFFERENTIAL CORRECTIONS.
00210 REN PROCEDURE IS TO ESTIMATE THE VARIABLES U3,U4,L3,L4 AND
00220 REN CALCULATE A1,B1,A2,B2,A3,B3 FROM STRAIGHT LEAST SQUARES ;
00230 REN USING ESTIMATES ON A1,B1,A2,B2,A3,B3 FROM LEAST SQUARES,
00240 REN DIFFERENTIAL CORRECTIONS ARE USED TO IMPROVE ESTIMATES
00250 REN OF U3,U4,L3,L4. THIS PROCEDURE MAY BE REPEATED AN ARBITRARY
00260 REN NUMBER OF ITERATIONS. A PRINT OUT OF THE STANDARD DEVIATION,E,
00270 REN IS USED A A MEASURE OF THE DEGREE OF FIT.
00280 I1 = .02476
00290 I2 = 0.1925
00300 BASE 1
00310 DIM A(1000),B(1000),AO(1000),BO(1000),T(1000)
00320 DIM G(6,6),G1(6,6),F(4,4),F1(4,4)
00330 DIM R1(4),G1(6),D(6),R(1000),B(1000),C(4)
00340 FILE #1 = "TAPE1"
00350 INPUT #1,R9,N
00360 PRINT "ENTER; L1= STARTING LINE NO AND L2 = ENDING LINE NO."
00370 INPUT L1,L2
00380 S = L1 -1
00390 IF S<=0 THEN 00430
00400 FOR I = 1 TO S
00410 INPUT #1,B,D,D
00420 NEXT I
00430 N = L2-L1+1
00440 FOR I = 1 TO N
00450 INPUT #1,T(I),A(I),B(I)
00460 NEXT I
00470 PRINT "STARTING AND ENDING VALUES"
00480 PRINT T(1),A(1),B(1)
00490 PRINT T(N),A(N),B(N)
00500 U3 = 10.62
00510 U4 = (-1)*13.655

```

TABLE 2 (CONTINUED)
DATA REDUCTION PROGRAM

```

00520 L3 = (-1)*.12
00530 L4 = (-1)*.0475
00540 P = (I2/I1)*(U3+U4)
00550 FOR K = 1 TO 15
00560 DEF FNA(T) = COS(U3*T)*EXP(L3*T)
00570 DEF FNB(T) = SIN(U3*T)*EXP(L3*T)
00580 DEF FNC(T) = COS(U4*T)*EXP(L4*T)
00590 DEF FND(T) = SIN(U4*T)*EXP(L4*T)
00600 DEF FNE(T) = COS(P*T)
00610 DEF FNF(T) = SIN(P*T)
00620 DEF FNB(T) = (B4*COS(U3*T)-A4*SIN(U3*T))*T*EXP(L3*T)
00630 DEF FNH(T) = (B5*COS(U4*T)-A5*SIN(U4*T))*T*EXP(L4*T)
00640 DEF FNI(T) = (A4*COS(U3*T)+B4*SIN(U3*T))*T*EXP(L3*T)
00650 DEF FNJ(T) = (A5*COS(U4*T)+B5*SIN(U4*T))*T*EXP(L4*T)
00660 DEF FNN(T) = (-1)*SIN(U3*T)*EXP(L3*T)
00670 DEF FNN(T) = COS(U3*T)*EXP(L3*T)
00680 DEF FNP(T) = (-1)*SIN(U4*T)*EXP(L4*T)
00690 DEF FNP(T) = COS(U4*T)*EXP(L4*T)
00700 DEF FNR(T) = (-1)*SIN(P*T)
00710 DEF FNS(T) = COS(P*T)
00720 DEF FNT(T) = (-T)*(B4*SIN(U3*T)+A4*COS(U3*T))*EXP(L3*T)
00730 DEF FNU(T) = (-T)*(B5*SIN(U4*T)+A5*COS(U4*T))*EXP(L4*T)
00740 DEF FNV(T) = (T)*(B4*COS(U3*T)-A4*SIN(U3*T))*EXP(L3*T)
00750 DEF FNV(T) = (T)*(B5*COS(U4*T)-A5*SIN(U4*T))*EXP(L4*T)
00760 FOR I = 1 TO 6
00770 FOR J = 1 TO 6
00780 G(I,J) = 0
00790 NEXT J
00800 NEXT I
00810 FOR I = 1 TO 6
00820 G1(I) = 0
00830 NEXT I
00840 FOR I = 1 TO N
00850 H = T(I)
00860 G(1,1) = FNA(H)*FNA(H)+FNN(H)*FNN(H)+G(1,1)
00870 G(1,2) = FNA(H)*FNB(H)+FNN(H)*FNN(H)+G(1,2)
00880 G(1,3) = FNA(H)*FNC(H)+FNN(H)*FNP(H)+G(1,3)
00890 G(1,4) = FNA(H)*FND(H)+FNN(H)*FNP(H)+G(1,4)
00900 G(1,5) = FNA(H)*FNE(H)+FNN(H)*FNR(H)+G(1,5)
00910 G(1,6) = FNA(H)*FNF(H)+FNN(H)*FNS(H)+G(1,6)
00920 G(2,1) = FNB(H)*FNA(H)+FNN(H)*FNN(H)+G(2,1)
00930 G(2,2) = FNB(H)*FNB(H)+FNN(H)*FNN(H)+G(2,2)

```

TABLE 2 (CONTINUED)
DATA REDUCTION PROGRAM

```

00940 B(2,3) = FNB(H)*FNC(H)+FNN(H)*FNP(H)+B(2,3)
00950 B(2,4) = FNB(H)*FND(H)+FNN(H)*FNQ(H)+B(2,4)
00960 B(2,5) = FNB(H)*FNE(H)+FNN(H)*FNR(H)+B(2,5)
00970 B(2,6) = FNB(H)*FNF(H)+FNN(H)*FNS(H)+B(2,6)
00980 B(3,1) = FNC(H)*FNA(H)+FNP(H)*FNN(H)+B(3,1)
00990 B(3,2) = FNC(H)*FNB(H)+FNP(H)*FNN(H)+B(3,2)
01000 B(3,3) = FNC(H)*FNC(H)+FNP(H)*FNP(H)+B(3,3)
01010 B(3,4) = FNC(H)*FND(H)+FNP(H)*FNQ(H)+B(3,4)
01020 B(3,5) = FNC(H)*FNE(H)+FNP(H)*FNR(H)+B(3,5)
01030 B(3,6) = FNC(H)*FNF(H)+FNP(H)*FNS(H)+B(3,6)
01040 B(4,1) = FND(H)*FNA(H)+FNQ(H)*FNN(H)+B(4,1)
01050 B(4,2) = FND(H)*FNB(H)+FNQ(H)*FNN(H)+B(4,2)
01060 B(4,3) = FND(H)*FNC(H)+FNQ(H)*FNP(H)+B(4,3)
01070 B(4,4) = FND(H)*FND(H)+FNQ(H)*FNQ(H)+B(4,4)
01080 B(4,5) = FND(H)*FNE(H)+FNQ(H)*FNR(H)+B(4,5)
01090 B(4,6) = FND(H)*FNF(H)+FNQ(H)*FNS(H)+B(4,6)
01100 B(5,1) = FNE(H)*FNA(H)+FNR(H)*FNN(H)+B(5,1)
01110 B(5,2) = FNE(H)*FNB(H)+FNR(H)*FNN(H)+B(5,2)
01120 B(5,3) = FNE(H)*FNC(H)+FNR(H)*FNP(H)+B(5,3)
01130 B(5,4) = FNE(H)*FND(H)+FNR(H)*FNQ(H)+B(5,4)
01140 B(5,5) = FNE(H)*FNE(H)+FNR(H)*FNR(H)+B(5,5)
01150 B(5,6) = FNE(H)*FNF(H)+FNR(H)*FNS(H)+B(5,6)
01160 B(6,1) = FNF(H)*FNA(H)+FNS(H)*FNN(H)+B(6,1)
01170 B(6,2) = FNF(H)*FNB(H)+FNS(H)*FNN(H)+B(6,2)
01180 B(6,3) = FNF(H)*FNC(H)+FNS(H)*FNP(H)+B(6,3)
01190 B(6,4) = FNF(H)*FND(H)+FNS(H)*FNQ(H)+B(6,4)
01200 B(6,5) = FNF(H)*FNE(H)+FNS(H)*FNR(H)+B(6,5)
01210 B(6,6) = FNF(H)*FNF(H)+FNS(H)*FNS(H)+B(6,6)
01220 Q1(1) = FNA(H)*A(I)+FNN(H)*B(I)+Q1(1)
01230 Q1(2) = FNB(H)*A(I)+FNN(H)*B(I)+Q1(2)
01240 Q1(3) = FNC(H)*A(I)+FNP(H)*B(I)+Q1(3)
01250 Q1(4) = FND(H)*A(I)+FNQ(H)*B(I)+Q1(4)
01260 Q1(5) = FNE(H)*A(I)+FNR(H)*B(I)+Q1(5)
01270 Q1(6) = FNF(H)*A(I)+FNS(H)*B(I)+Q1(6)
01280 NEXT I
01290 MAT B1 = INV(B)
01300 MAT D = B1*Q1
01310 A4 = D(1)
01320 B4 = D(2)
01330 A5 = D(3)
01340 B5 = D(4)
01350 A6 = D(5)

```

TABLE 2 (CONTINUED)
DATA REDUCTION PROGRAM

```

01360 B6 = B(6)
01370 FOR I = 1 TO N
01380 T = T(I)
01390 A0(I) = (A4*COS(U3*T)+B4*SIN(U3*T))*EXP(L3*T)
01400 A0(I) = A0(I)+(A5*COS(U4*T)+B5*SIN(U4*T))*EXP(L4*T)
01410 A0(I) = A0(I)+A6*COS(P*T)+B6*SIN(P*T)
01420 B0(I) = (B4*COS(U3*T)-A4*SIN(U3*T))*EXP(L3*T)
01430 B0(I) = B0(I)+(B5*COS(U4*T)-A5*SIN(U4*T))*EXP(L4*T)
01440 B0(I) = B0(I)+B6*COS(P*T)-A6*SIN(P*T)
01450 NEXT I
01460 HAT R = A0-A
01470 HAT Q = B0-B
01480 FOR I = 1 TO 4
01490 FOR J = 1 TO 4
01500 F(I,J) = 0
01510 NEXT J
01520 NEXT I
01530 FOR I = 1 TO 4
01540 R1(I) = 0
01550 NEXT I
01560 Z8 = 0
01570 FOR I = 1 TO N
01580 H = T(I)
01590 F(1,1) = FNB(H)*FNB(H)+FNT(H)*FNT(H)+F(1,1)
01600 F(1,2) = FNB(H)*FNN(H)+FNT(H)*FNU(H)+F(1,2)
01610 F(1,3) = FNB(H)*FNI(H)+FNT(H)*FNV(H)+F(1,3)
01620 F(1,4) = FNB(H)*FNJ(H)+FNT(H)*FNW(H)+F(1,4)
01630 F(2,1) = FNN(H)*FNB(H)+FNU(H)*FNT(H)+F(2,1)
01640 F(2,2) = FNN(H)*FNN(H)+FNU(H)*FNU(H)+F(2,2)
01650 F(2,3) = FNN(H)*FNI(H)+FNU(H)*FNV(H)+F(2,3)
01660 F(2,4) = FNN(H)*FNJ(H)+FNU(H)*FNW(H)+F(2,4)
01670 F(3,1) = FNI(H)*FNB(H)+FNV(H)*FNT(H)+F(3,1)
01680 F(3,2) = FNI(H)*FNN(H)+FNV(H)*FNU(H)+F(3,2)
01690 F(3,3) = FNI(H)*FNI(H)+FNV(H)*FNV(H)+F(3,3)
01700 F(3,4) = FNI(H)*FNJ(H)+FNV(H)*FNW(H)+F(3,4)
01710 F(4,1) = FNJ(H)*FNB(H)+FNU(H)*FNT(H)+F(4,1)
01720 F(4,2) = FNJ(H)*FNN(H)+FNU(H)*FNU(H)+F(4,2)
01730 F(4,3) = FNJ(H)*FNI(H)+FNU(H)*FNV(H)+F(4,3)
01740 F(4,4) = FNJ(H)*FNJ(H)+FNU(H)*FNW(H)+F(4,4)
01750 R1(1) = (-1)*(FNB(H)*R(I)+FNT(H)*Q(I))+R1(1)
01760 R1(2) = (-1)*(FNN(H)*R(I)+FNU(H)*Q(I))+R1(2)
01770 R1(3) = (-1)*(FNI(H)*R(I)+FNV(H)*Q(I))+R1(3)

```

TABLE 2 (CONTINUED)
DATA REDUCTION PROGRAM

```
01780 R1(4) = (-1)*(FNJ(H)*R(I)+FNU(H)*Q(I))+R1(4)
01790 Z8 = R(I)*R(I)+Q(I)*Q(I)+Z8
01800 NEXT I
01810 MAT F1 = INV(F)
01820 MAT C = F1*R1
01830 U3 = U3+C(1)
01840 U4 = U4+C(2)
01850 L3 = L3+C(3)
01860 L4 = L4+C(4)
01870 E = 0.6745*SQR(Z8/(2*N-4))
01880 IF K>1 THEN 01930
01890 PRINT "RUN NUMBER =",R9
01900 PRINT
01910 PRINT "STAND.DEV.-E","NU-FREQ","PREC-FREQ","NU-BAND","PREC-BAND"
01920 PRINT
01930 PRINT E,U3,U4,L3,L4
01940 P = (12/I1)*(U3+U4)
01950 NEXT K
01960 PRINT
01970 PRINT "A1","B1","A2","B2","A3"
01980 PRINT A4,B4,A5,B5,A6
01990 PRINT
02000 PRINT "B3","U1","U2","L1","L2"
02010 PRINT B6,U3,U4,L3,L4
02020 END
```

In lines 280 and 290 the transverse and longitudinal moments of inertia of the model are given. Line 300 may not be necessary with all computer systems; here the term "BASE I" indicates that all subscripted variables begin with "one" rather than "zero." Some BASIC compilers assume, in default, that a matrix dimensioned D(4) has five elements. The statement of line 300 means that a dimension of D(4) has four elements.

Various matrices are dimensioned in lines 310 to 340. The matrices A, B, AO, BO and T have been dimensioned in excess of any encountered data length. However, all five column matrices should have the same dimension number. This remark also applies to column matrices R and Q in line 330. All other matrices are dimensioned to the exact value needed in the program.

Lines 340 through 490 are for data input. All material in these lines can be omitted provided that some other way is chosen to input data. Data must be input as three column matrices: angle of attack, $\alpha(t_1) = A(I)$, angle of side slip, $\beta(t_1) = B(I)$ and time $t_1 = T(I)$, where I is data count. The data triplet A(I), B(I), T(I) need not be at equal time intervals, but the triplet must be complete. In the illustrated arrangement, data is available from a file. The symbol R9 in line 350 is used to designate the file, here taken as a programmer's identification number. The symbol N, also in the same line, indicates the number of data point, i.e. how many triplets $\alpha(t)$, $\beta(t)$, t are in the list. In line 370, an input statement permits restricted input from the data file. Thus L1 is the data point number at which the file begins and L2 is the data point number at which the file ends. To enter the total data file, L1 = 1, L2 = N (numerical equal to total number of data points).

In lines 500 through 530 initial estimates of the four constants $\omega_1 = W3$, $\omega_2 = W4$, $\lambda_1 = L3$ and $\lambda_2 = L4$, according to step (a) in the summary given at the end of section 3.2. An estimated value of spin rate, p, is given in line 540, which is

based upon the estimates of ω_1 and ω_2 and equation (11c).

Line 550 sets the number of iterations that the program will undergo. Obviously this number is arbitrary; a conditional transfer might be entered near the end of the program based upon some selected value of E; however, this was not done.

The functions defined in lines 560 through 750 are easily related to the twelve derivatives given in equation (30). Lines 860 through 1270 define the 36 elements of the G_{kj} matrix and the six elements of the $Q1_j$ matrix of equations (34). Both of these matrices are initialized in lines 760 through 830. The solution of the matrix equation (equation (35)) is given in line 1300. The elements, i.e. $A_1, B_1, A_2, B_2, A_3, B_3$ are obtained in lines 1310 through 1360; $A_1, B_1, A_2, B_2, A_3, B_3$ are equal in turn to A4, B4, A5, B5, A6, B6.

In lines 1390 through 1440 the initial estimates on $\alpha(t)$ and $\beta(t)$ are given. According to equations (18) these initial estimates are represented by $\alpha(t_1; \bar{A}_1, \dots, \bar{\lambda}_2)$ and $\beta(t_1; \bar{A}_1, \dots, \bar{\lambda}_2)$ and are formed by using the estimated parameters in equations (6). The residuals R_1 and Q_1 of equations (19) are set in lines 1460 and 1470. The elements of the four by four matrix, F_{kj} , of equation (23) are calculated in lines 1590 through lines 1780. The various functions used in calculating the elements of F_{kj} are defined in lines 1620 through 1650 and lines 1720 through 1750. The RL_k column matrix, defined in equations (24b) is calculated in lines 1750 through 1780. The matrix inversion indicated in equation (25) is carried out in line 1810. The elements of matrix C_j are calculated in line 1820. The iterations of equation (26) is given in lines 1830 through 1860 where $\omega_1, \omega_2, \lambda_1, \lambda_2$ are represented in turn by W4, W5, L4, L5. The probable error of fit expressed in equation (29) is calculated in line 1930.

The iterative process is repeated by indexing K in line 1950. The index variable, K, is set at 20 in line 550. As pointed out earlier the number of iterations are arbitrary and might in some applications be keyed to the probable error

TABLE 3
STABILITY DERIVATIVE PROGRAM.

```

00100 REM THIS PROGRAM CALCULATES THE STATIC STABILITY,
00110 REM DYNAMIC STABILITY AND MAGNUS DERIVATIVES,
00120 REM SPIN RATE AND CENTER OF PRESSURE FROM THE NUTATIONAL AND
00130 REM PRECESSIONAL FREQUENCIES AND EXPONENTIAL DAMPING.
00140 REM WIND TUNNEL MACH NUMBER (M), TOTAL PRESSURE (P0),PSF,
00150 REM TOTAL TEMPERATURE (T0), DEG-F, NUTATIONAL/PRECESSIONAL
00160 REM FREQUENCIES/DAMPING U1,U2,L1,L2 ARE ENTERED. D,I,I1
00170 REM ARE REFERENCE LENGTH (DIAMETER),FT, AND TRANSVERSE AND
00180 REM AXIAL MOMENTS OF INERTIA. N IS THE NORMAL
00190 REM FORCE DERIVATIVE (PER RADIAN).
00200 U1 = 14.2148
00210 U2 = (-1)*10.3401
00220 L1 = (-1)*2.15461E-2
00230 L2 = (-1)*2.53824E-2
00240 M = 1.35
00250 D = .5045
00260 I = .02476
00270 I1 = .1925
00280 N = 7.95
00290 P0 = 1.8144E5
00300 T0 = 955
00310 S = 3.14159*(D*D)/4
00320 T0 = T0*459.6
00330 Q = ((1+(M*2)/5)+((-1)*7/2))*0.7*(M*2)*P0
00340 V = 49.0143*SQRT(T0)
00350 V = V*N*((1+(M*2)/5)+((-1)/2))
00360 M1 = I1*U1*U2
00370 M2 = I1*(L1+L2)
00380 M3 = (-1)*I*((L1*U2+L2*U1)/(U1+U2))
00390 P = (I1/I)*(U1+U2)
00400 C1 = M1/(Q*S*D)
00410 C2 = 2*M2*V/(Q*S*D*D)
00420 C3 = 2*M3*V/(Q*S*D*D)
00430 X = ((-1)*C1+.3059)/N
00440 P1 = P*D/(2*V)
00450 PRINT "STATIC","DYNAMIC","MAGNUS","SPIN","C.P."
00460 PRINT "CHA","CHQ","CHPA","P(RAD/SEC)","X(BODY-LENGTH)"
00470 PRINT
00480 PRINT C1,C2,C3,P,X
00490 END

```

of fit, E.

The computer program just discussed provides the nutational and precessional frequencies ω_1 and ω_2 and the nutational and precessional exponents, λ_1 and λ_2 . However these four quantities are only intermediate values; final data must be in the form of the aerodynamic derivatives: the pitching moment derivative, C_{m_α} , the pitch damping derivative, C_{m_q} , the Magnus derivative, $C_{m_{p\alpha}}$; and the spin rate, p. A second program has been written to convert the nutational and precessional frequencies and damping exponents, along with relevant wind tunnel flow measurements into these derivatives. This program is listed in Table 3.

In Table 3 the frequencies and damping exponents are entered in lines 190 through 220 with ω_1 , ω_2 , λ_1 , λ_2 equal in turn to W1, W2, L1, L2. Model diameter is entered in line 230. Axial and transverse moments of inertia are entered respectively in lines 240 and 250. Mach number, total pressure and total temperature are entered in lines 260, 270 and 280 respectively. The derivatives C_{m_α} , C_{m_q} , $C_{m_{p\alpha}}$, p and $pd/2V$ printed out in order in line 450.

In Table 4 to follow the symbols used in this analysis are given, both the symbol as it appears in the analytic expressions and as it appears in the computer program. The number of the first equation in which the symbol appears and the first line in which it appears in the program are also given. Line numbers indicated with an asterisk refer to the computer program given in Table 3; lines without such a designation refer to the data reduction program given in Table 2.

In the next section some sample wind tunnel data is presented. These data will indicate the utility of the analytic methods just developed in reducing data from the angular motion of gas-bearing-supported models.

TABLE 4 SYMBOL DEFINITION

ANALYTIC SYMBOL	COMPUTER SYMBOL	FIRST EQUATION	FIRST LINE	DEFINITION
A_1	A4	(6a,b)	1310	Initial Condition (sym.) in α
A_2	A5	(6a,b)	1330	Initial Condition (sym.) in α
A_3	A6	(6a,b)	1350	Initial Condition (asym) in α
B_1	B4	(6a,b)	1320	Initial Condition (sym) in β
B_2	B5	(6a,b)	1340	Initial Condition (sym) in β
B_3	B6	(6a,b)	1360	Initial Condition (asym) in β
C_j	C	(23)	1820	Frequency/damping matrix
$C_{m\alpha}$	C1	--	380*	Pitching Moment derivative
C_{mq}	C2	--	390*	Pitch damping derivative
$C_{mp\beta}$	C3	--	400*	Magnus derivative
d, D	D	--	230*	Body Diameter
D_j	D(J)	(35)	1300	Initial Condition Matrix
E	E	(27)	1870	Probable Error of fit
F_{jk}	F(J,K)	(23)	1590	Normal matrix-differential corrections
G_{jk}	G(J,K)	(34)	860	Normal matrix-least squares
I, I_y	I2	(4)	280	Transverse moment of inertia
I_x	I1	(4)	290	Axial moment of inertia
M	M	--	260*	Mach number
n	N	--	350	Number of data points
--	I	--	400	Index variable
--	J	--	770	Index variable
--	K	--	550	Index variable
p	P	(11c)	540	Spin rate
pd/2V	P1	--	410*	Reduced spin rate

TABLE 4 (Cont.)

ANALYTIC SYMBOL	COMPUTER SYMBOL	FIRST EQUATION	FIRST LINE	DEFINITION
P_o	PO	--	270*	Total pressure
\bar{q}	Q	--	310*	Dynamic pressure
q_1	--	(15b)	--	Residual - least squares
Q_1	Q(I)	(19b)	1470	Residual - differential corrections
$Q1_k$	Q1(K)	(34)	1220	Residual matrix - least squares
r_1	--	(15a)	--	Residual - least squares
R_1	R(I)	(19a)	1460	Residual - differential corrections
$R1_k$	R1(K)	(23)	1750	Residual matrix - diff. corrections
s	S	--	290*	Body cross-sectional area
t	T(I)	(4)	310	Time
T_o	TO	--	300*	Total temperature
V	V	--	320*	Airspeed
α	A	(6a)	310	Angle of attack
$\bar{\alpha}$	AO	(19a)	1390	Estimate of angle of attack
α_∞	--	--	--	Steady state angle of attack
α_T	--	--	--	Magnitude of trim angle
β	B	(6b)	310	Angle of side slip
$\bar{\beta}$	BO	(19b)	1420	Estimated angle of side slip
β_∞	--	--	--	Steady state angle of side slip
λ	--	(12b)	--	Zero-spin damping exponent
λ_1	L4	(10c)	520	Nutational damping exponent
$\bar{\lambda}_1$	C(3)	(26)	1850	Estimate of Nutational damp. exponent
λ_2	L5	(10d)	530	Precessional damping exponent
$\bar{\lambda}_2$	C(4)	(26)	1860	Estimate of Precessional damp. exponent

TABLE 4 (Cont.)

ANALYTIC SYMBOL	COMPUTER SYMBOL	FIRST EQUATION	FIRST LINE	DEFINITION
ξ	--	(3)	--	Complex angle of attack
τ	--	(9)	--	Inertia/Aerodynamic Coupling parameter
ω	--	(12a)	--	Zero-spin oscillation frequency
ω_1	W3	(10a)	500	Nutational frequency
ω_1	C(1)	(26)	1830	Estimate of nutational frequency
ω_2	W4	(10b)	510	Precessional frequency
ω_2	C(2)	(26)	1840	Estimate of nutational frequency

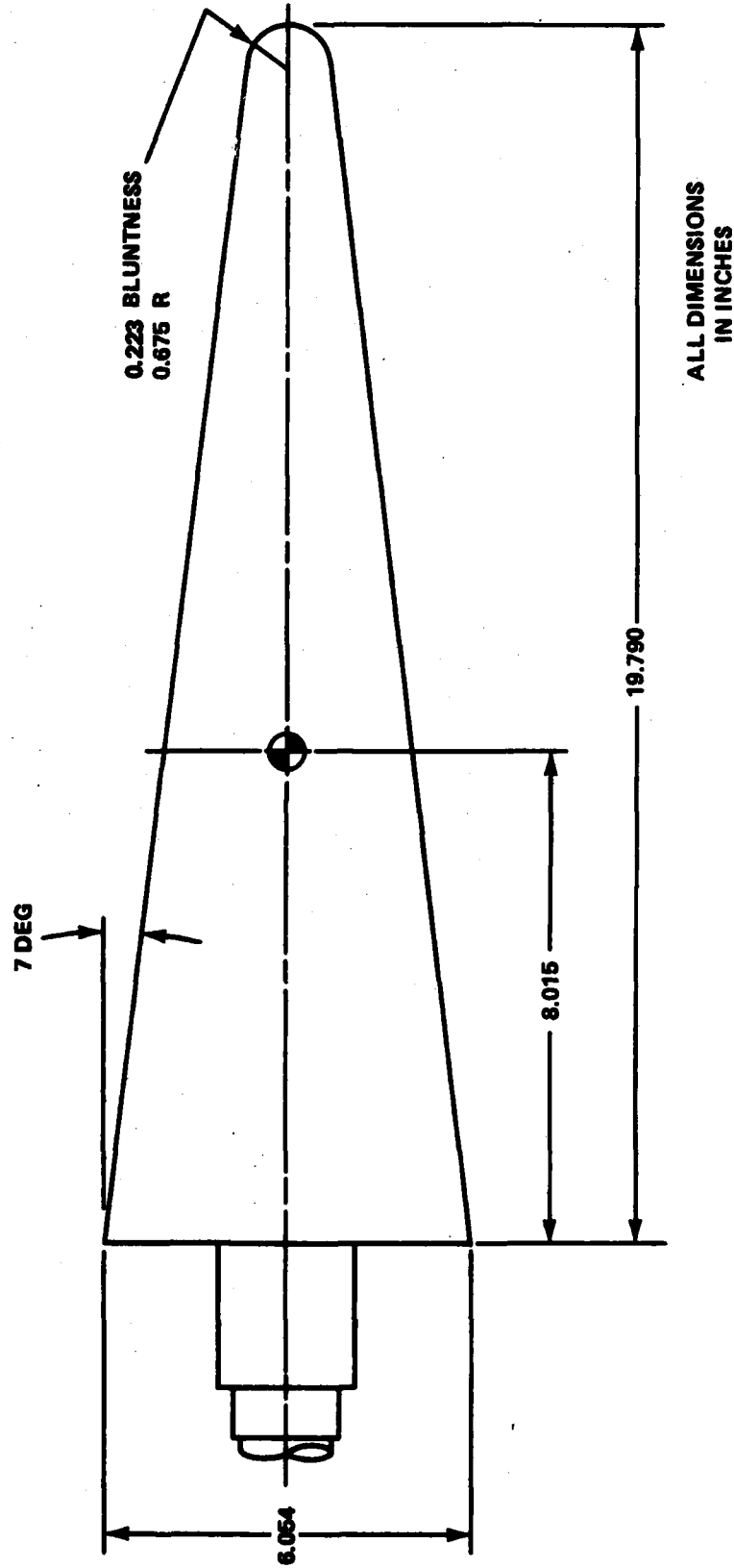


FIGURE 7 EXTERNAL DIMENSIONS OF WIND TUNNEL MODEL.

4.0 WIND TUNNEL TEST

A series of wind tunnel tests were carried out using the sphere cone model depicted in Figure 1. The testing was all done in the Naval Surface Weapon Center's Hypersonic Wind Tunnel. In these tests the model had both a non-ablating and ablating spherical nose. A line drawing of the model is given in Figure 7. It will be noted that the hemispherical nose has a bluntness of 0.223 (nose radius divided by cone base radius). The model oscillates about an axis that is 0.595 body lengths aft of the unablated nose.

Wind tunnel testing of the sphere-cone model is a fairly straightforward procedure. The model is mounted to the gas bearing assembly shown in Figure 2. The configuration as tested is shown fixed to the axial sting support in Figure 1.

With the model mounted in the wind tunnel, the spin turbine is activated by admitting air into the turbine conduit (see Figure 5b). A tachometer reading is used to monitor the spin rate. Minor adjustments are made to turbine air pressure to maintain spin rate after wind tunnel airflow is established. The angular transducers are continuously recorded and the orthogonal cameras are put into operation just prior to initiation of the kicking jet.

Because it is not possible to visually inspect the model during the period of wind tunnel operation, it was found convenient to enter the outputs from the horizontal- β and vertical- α angular transducers into the XY jacks of an oscilloscope. The display is a rough portrait of the α - β motion of the model. This practice enables the project engineer to observe any angular instabilities as well as the more likely damped motion. When the model has damped to a sufficiently small angle or to an obvious trim condition, the kicking jet is again used to activate angular motion.



SIDE CAMERA – VERTICAL MOTION



TOP CAMERA – HORIZONTAL MOTION



FIGURE 8 REPRESENTATIVE MODEL PHOTOGRAPHIC VIEWS APPROXIMATELY 1 SECOND APART.

It was mentioned earlier that while the fiber optic system functioned, the performance was not adequate for data reduction. Consequently the photographic record from the orthogonal camera installation was used. Figure 6 indicates how cameras were positioned. One camera obtains angular motion of the model in the vertical plane, the other, model motion in the horizontal plane. After film reading and time-frame-count correlation the two records $\alpha_1(t)$ and $\beta_1(t)$ are available for the data reduction procedure described in the previous section.

4.1 NON-ABLATING NOSE (NAN) WIND TUNNEL TESTS. In the non-ablating nose (NAN) tests the 7-degree conical model was tested with a steel hemispherical nose in place. The external geometry of the wind tunnel model is shown in Figure 7. The testing procedure was identical to that described in section 4.0. Primary data in this test was over 900 frames of 16mm film of model motion measured at each of the two orthogonal cameras, typical frames of the horizontal (β) and vertical (α) cameras are presented in Figure 8. The total of more than 1800 frames were "read" on a film reader. Film reading consists of setting moveable cross-hairs at two places on the image of the model's edge. The arc-tangent provides the angle of this edge; removal of the cone half-angle then gives the angle of the centerline of the model.

It will be recalled in equations (15) or (19) that the angles of attack and sideslip must be available at the same time, $t=t_1$. Thus it is necessary to designate one angular record, say, $\alpha=\alpha(t)$, as the primary and interpolate the second record, $\beta=\beta(t)$ in this case, to obtain both records at the same values of time. The record of $\alpha(t)$ (primary) and $\beta(t)$ (interpolated) are given in Figure 9. An alternate presentation of essentially the same information is provided in Figure 10. Here α (vertical) is plotted with β (horizontal) to give the familiar α - β petal graphs. The damped character of the motion is more obvious in Figure 10 than it perhaps is in Figure 9.

ANGLE OF ATTACK —————
 ANGLE OF SIDESLIP - - - - -
 TIME: 0 TO 5 SECONDS

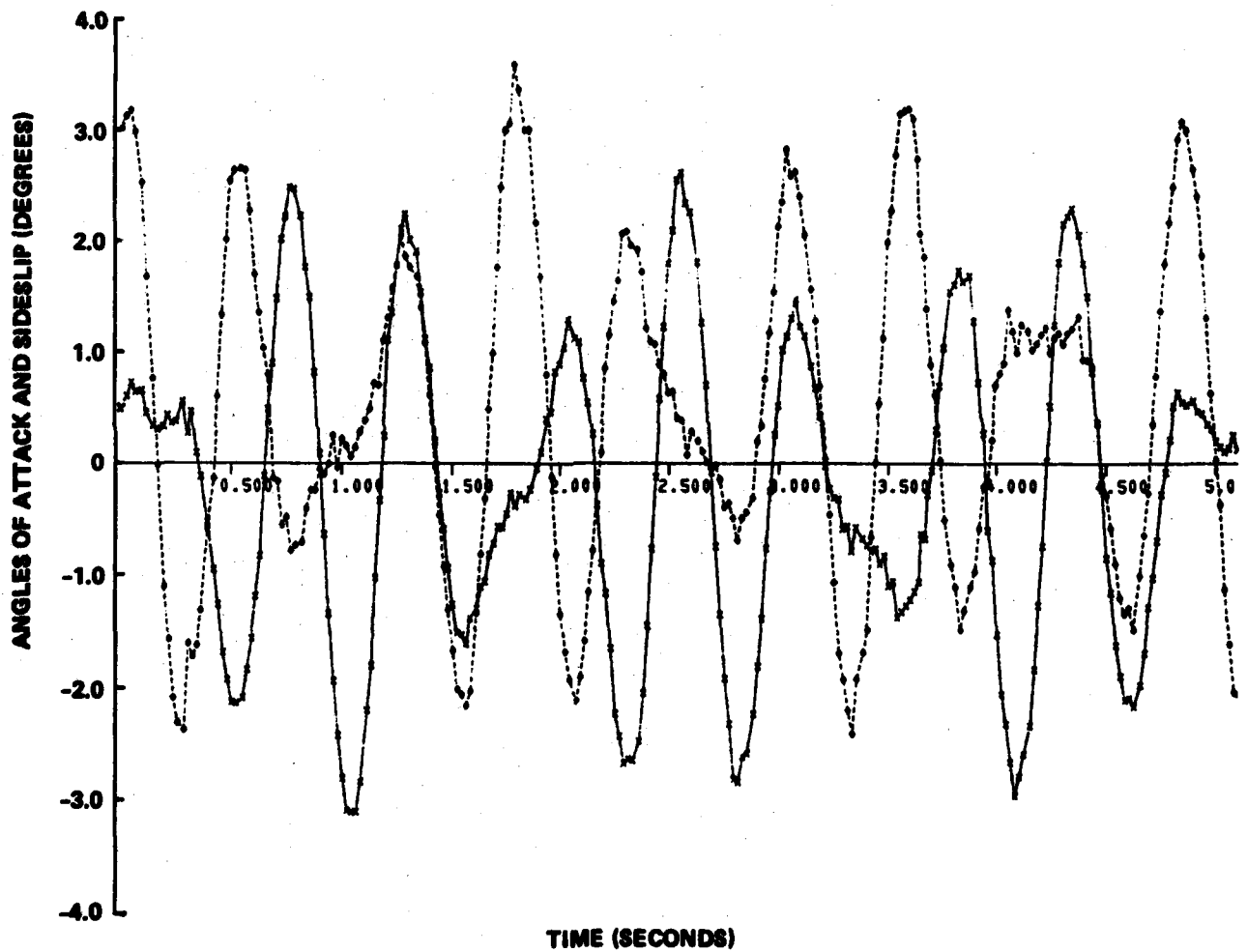


**FIGURE 9 (a) ANGLES OF ATTACK AND SIDESLIP VERSUS TIME
 (HEMI-SPHERICAL NOSE)**

ANGLE OF ATTACK —————
 ANGLE OF SIDESLIP - - - - -
 TIME: 5 TO 10 SECONDS

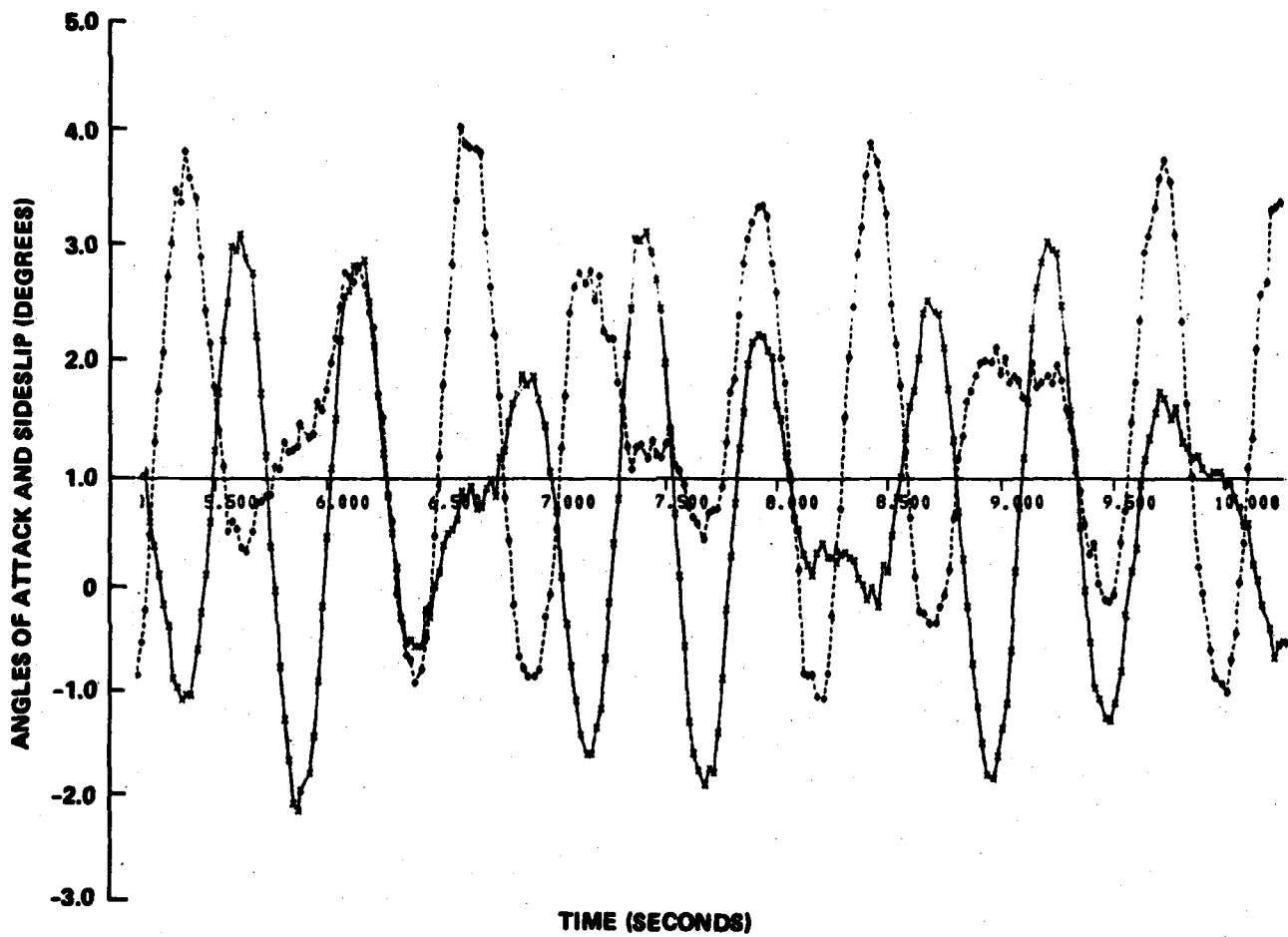


FIGURE 9 (b) ANGLES OF ATTACK AND SIDESLIP VERSUS TIME
 (HEMI-SPHERICAL NOSE)

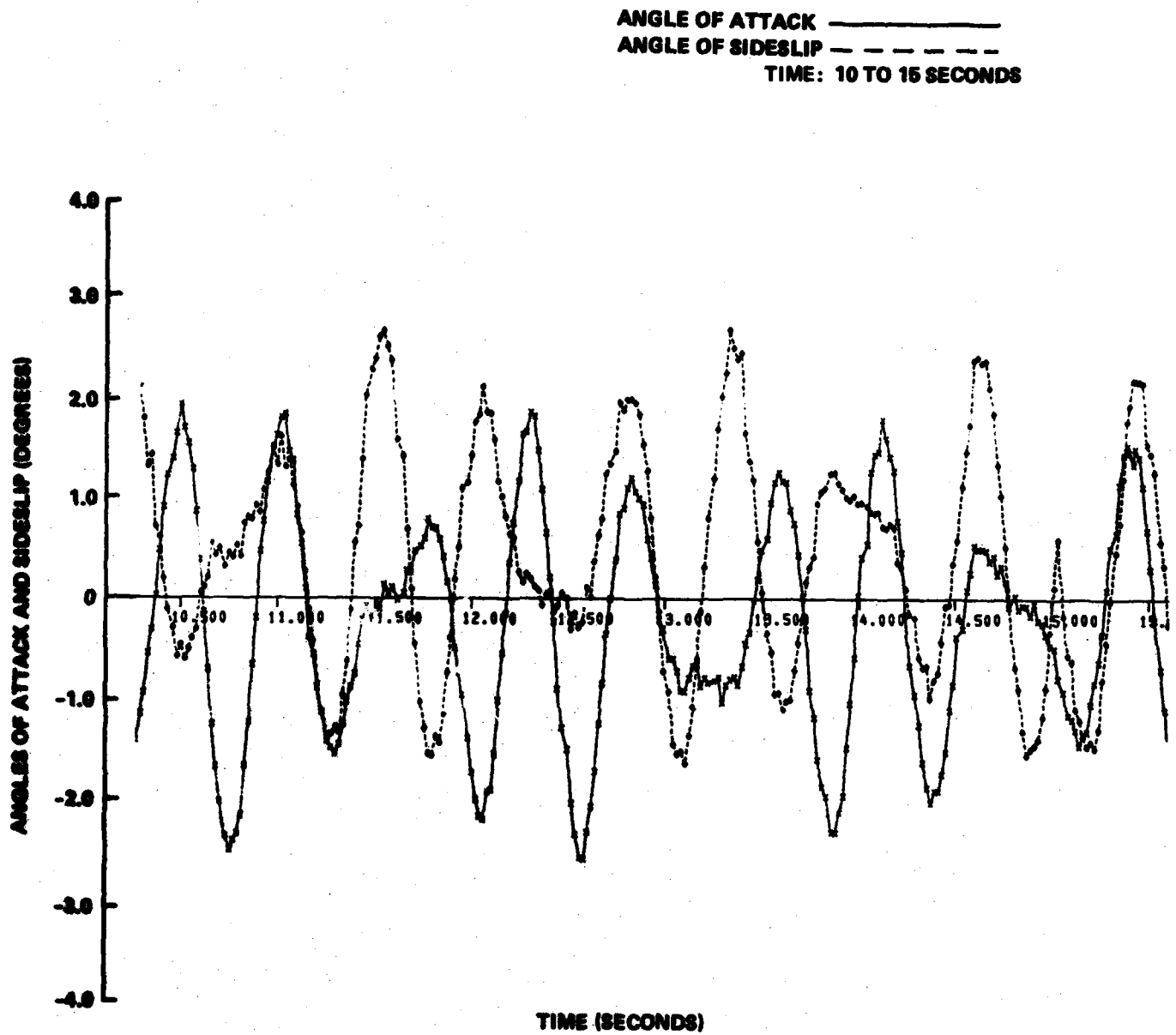


FIGURE 9 (a) ANGLES OF ATTACK AND SIDESLIP VERSUS TIME
 (HEMI-SPHERICAL NOSE)

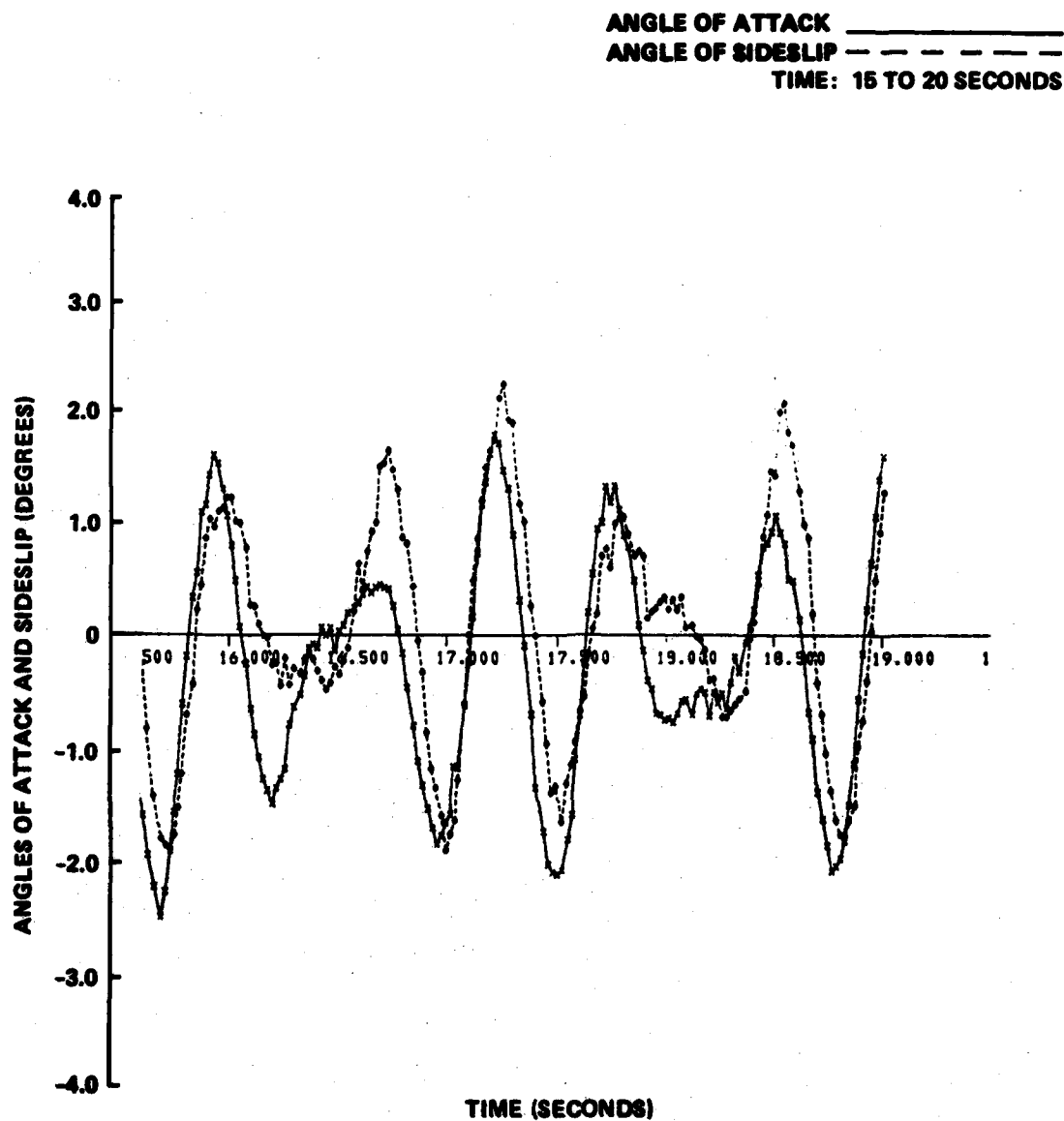


FIGURE 9 (d) ANGLES OF ATTACK AND SIDESLIP VERSUS TIME (HEMI-SPHERICAL NOSE)

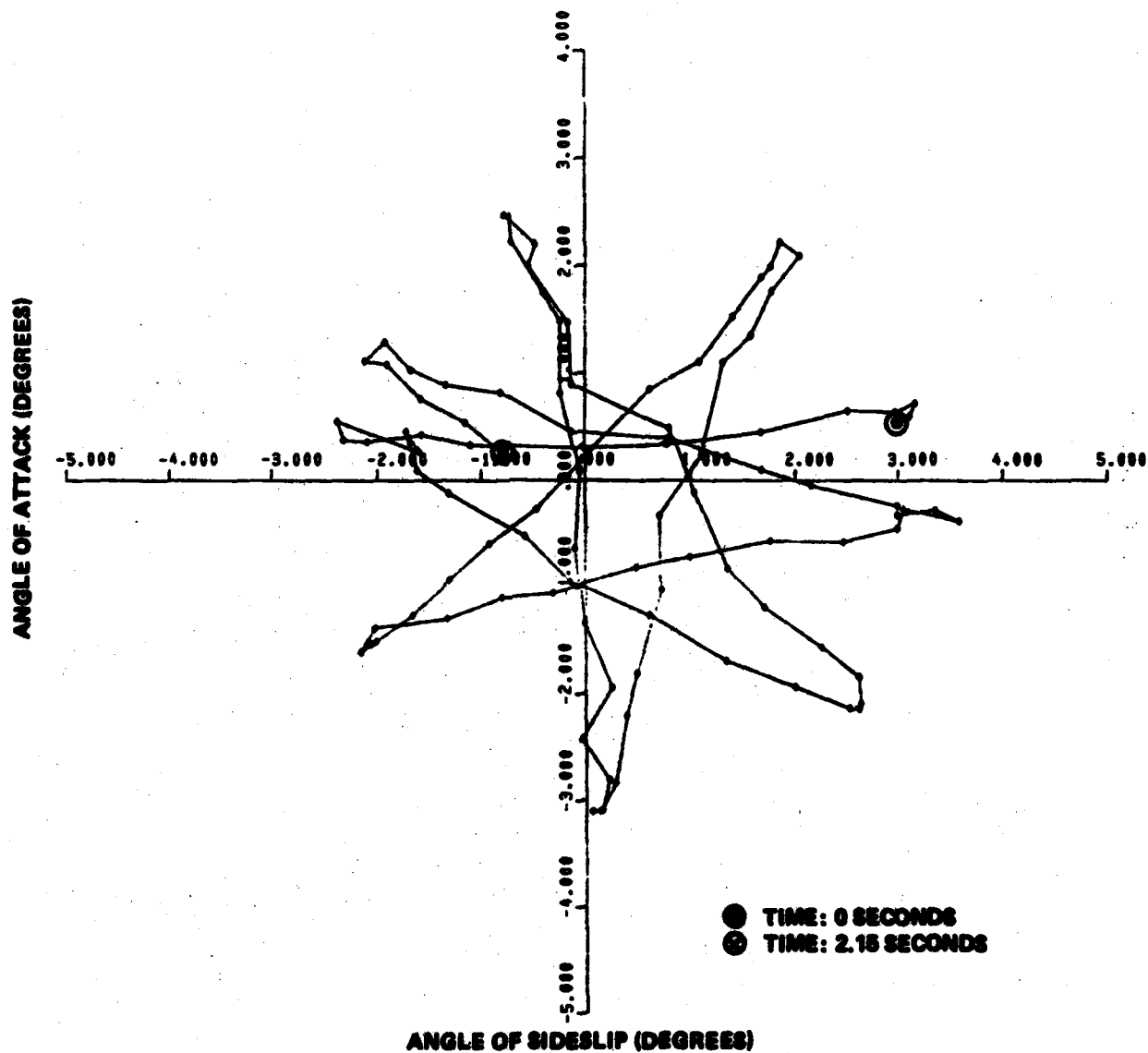


FIGURE 10 (a) ANGLE OF ATTACK VERSUS ANGLE OF SIDESLIP FOR TIME INTERVAL 0 TO 2.15 SECONDS (HEMI-SPHERICAL NOSE)

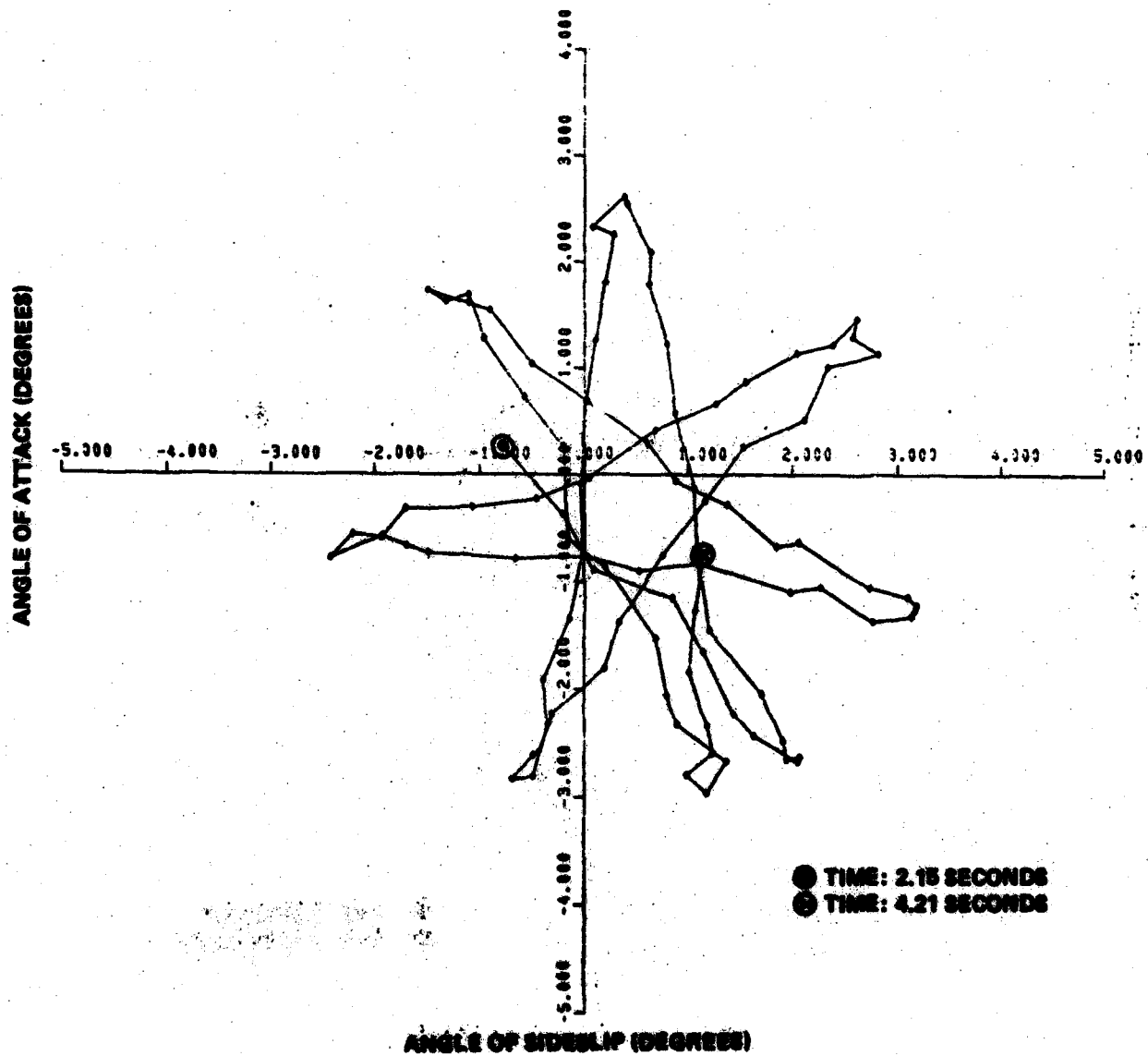


FIGURE 10 (b) ANGLE OF ATTACK VERSUS ANGLE OF SIDESLIP FOR TIME INTERVAL 2.15 TO 4.21 SECONDS (HEMISPHERICAL NOSE)

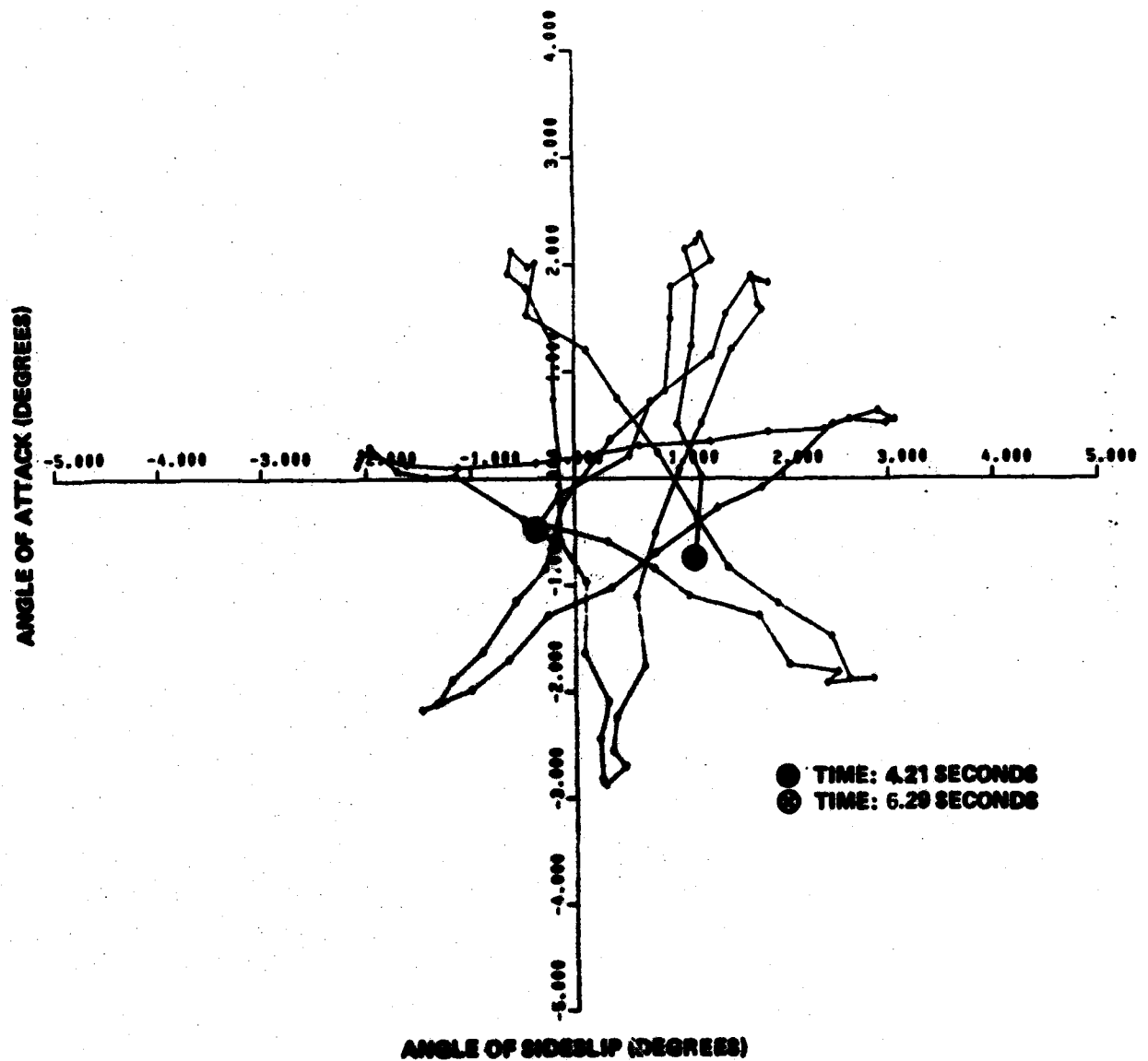


FIGURE 10 (a) ANGLE OF ATTACK VERSUS ANGLE OF SIDESLIP FOR TIME INTERVAL 4.21 TO 6.29 SECONDS (HEMISPHERICAL NOSE)

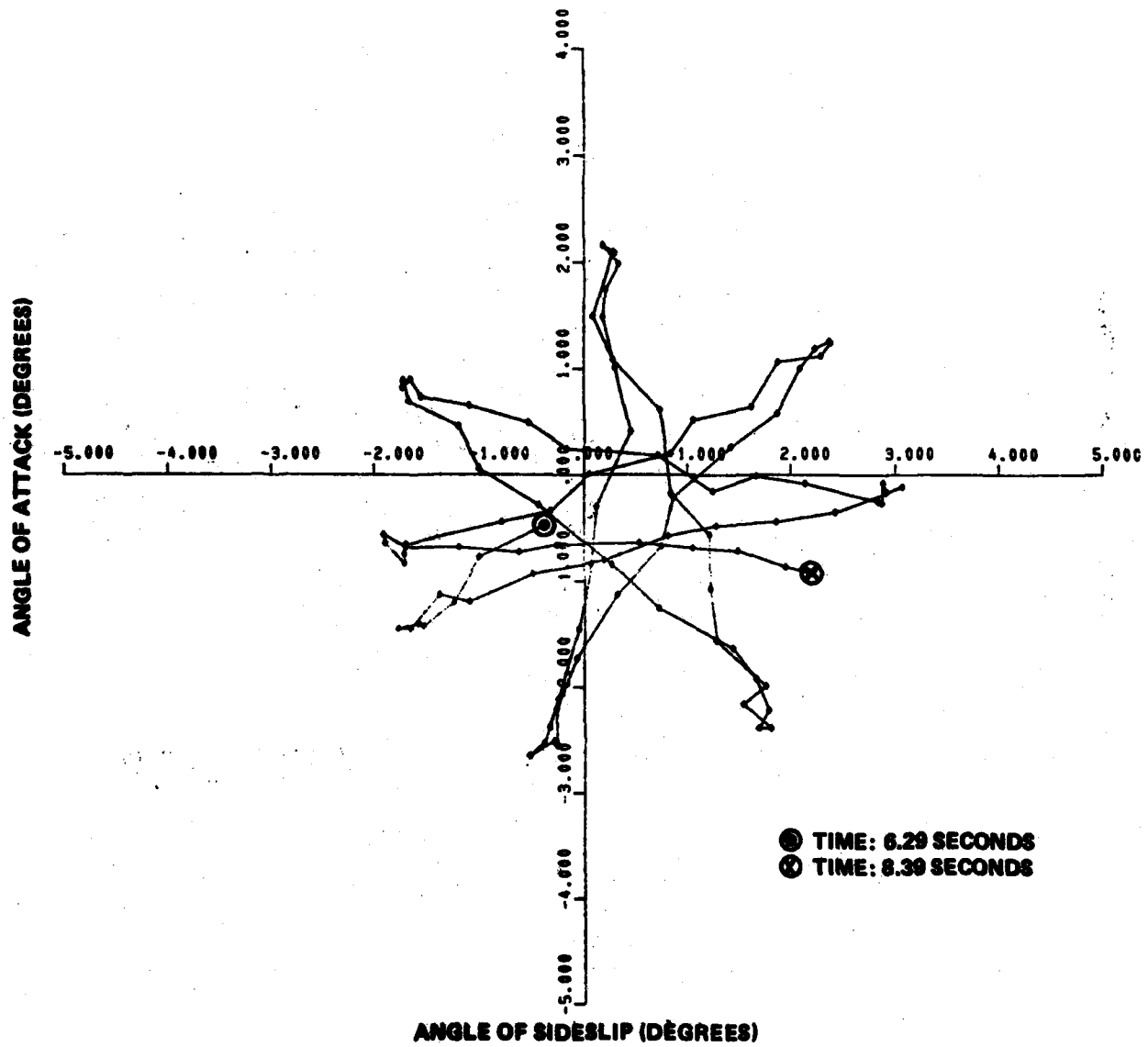


FIGURE 10 (a) ANGLE OF ATTACK VERSUS ANGLE OF SIDESLIP FOR TIME INTERVAL 6.29 TO 8.39 SECONDS (HEMI-SPHERICAL NOSE)

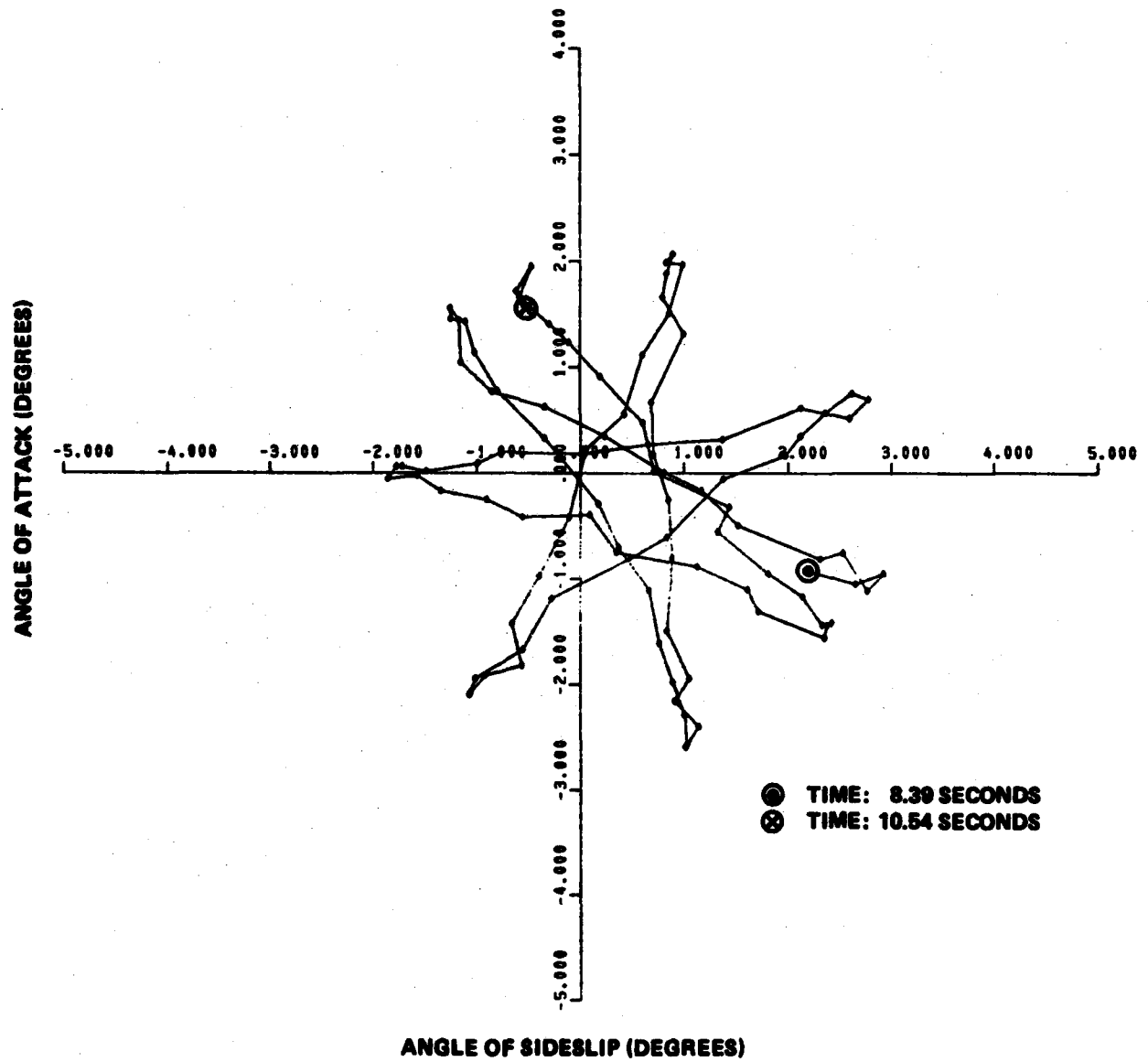


FIGURE 10 (a) ANGLE OF ATTACK VERSUS ANGLE OF SIDESLIP FOR TIME INTERVAL 8.39 TO 10.54 SECONDS (HEMI-SPHERICAL NOSE)

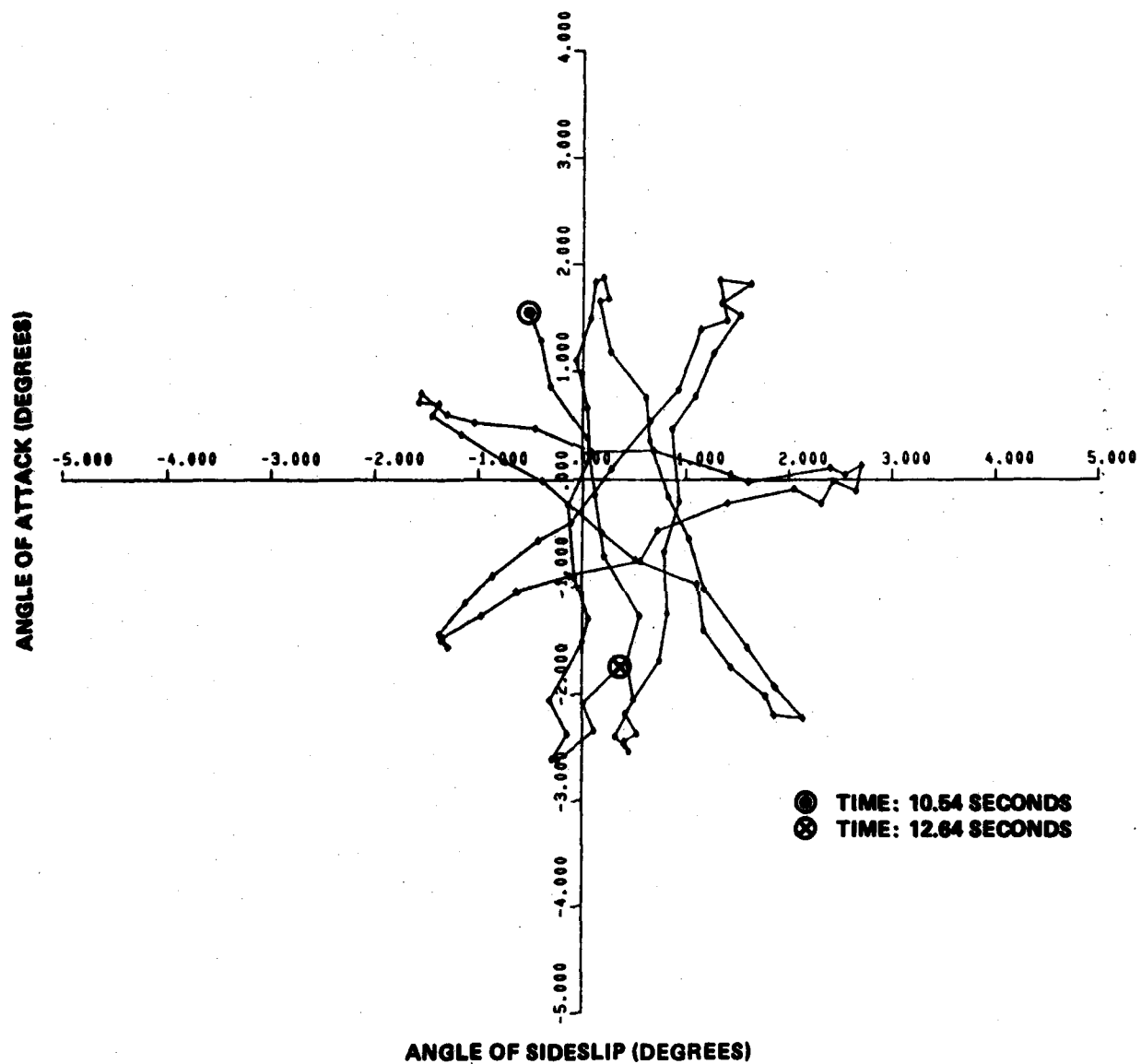


FIGURE 10 (f) ANGLE OF ATTACK VERSUS ANGLE OF SIDESLIP FOR TIME INTERVAL 10.54 TO 12.64 SECONDS (HEMI-SPHERICAL NOSE)

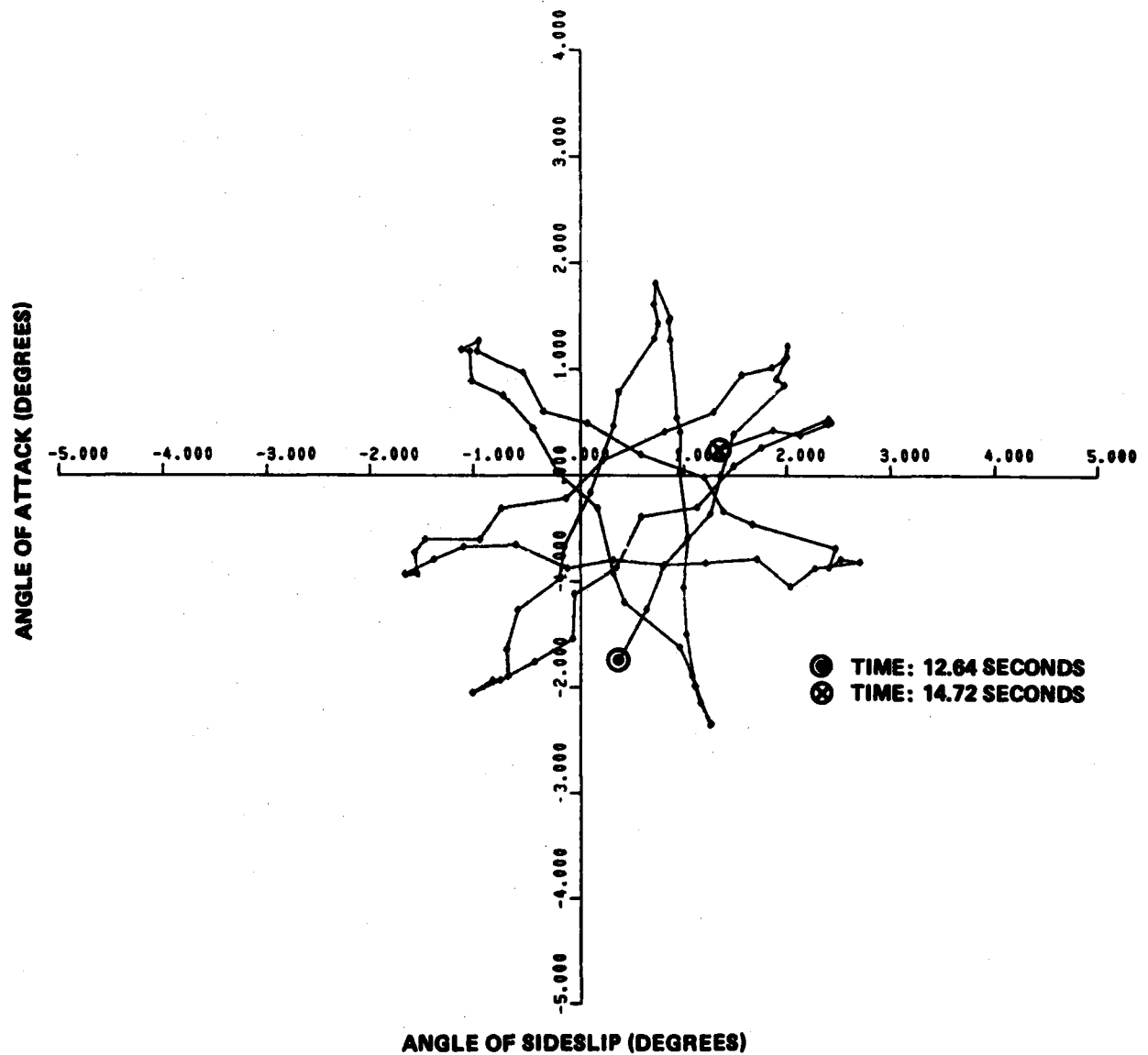


FIGURE 10 (g) ANGLE OF ATTACK VERSUS ANGLE OF SIDESLIP FOR TIME INTERVAL 12.64 TO 14.72 SECONDS (HEMI-SPHERICAL NOSE)

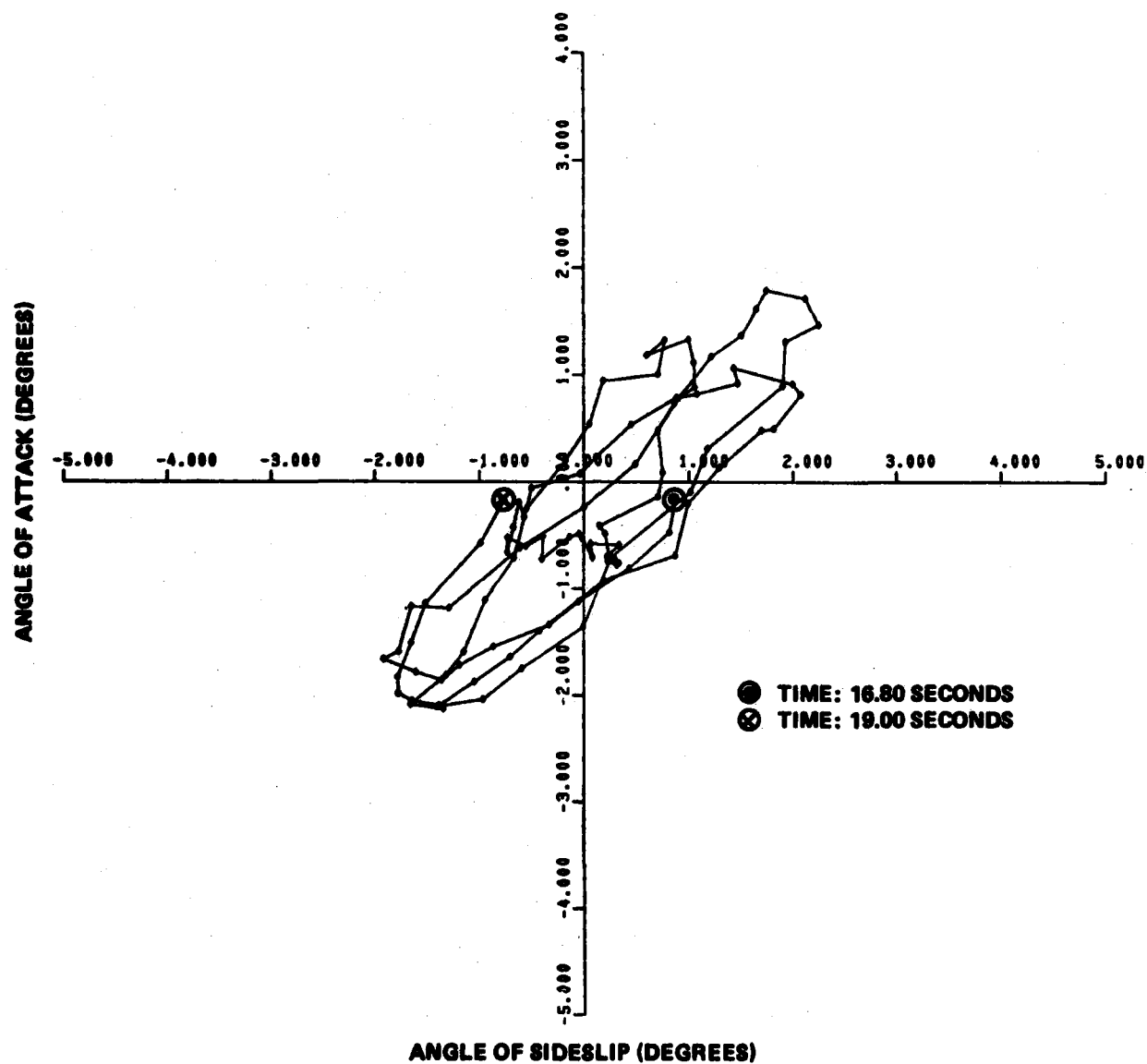


FIGURE 10 (h) ANGLE OF ATTACK VERSUS ANGLE OF SIDESLIP FOR TIME INTERVAL 16.80 TO 19.00 SECONDS (HEMI-SPHERICAL NOSE)

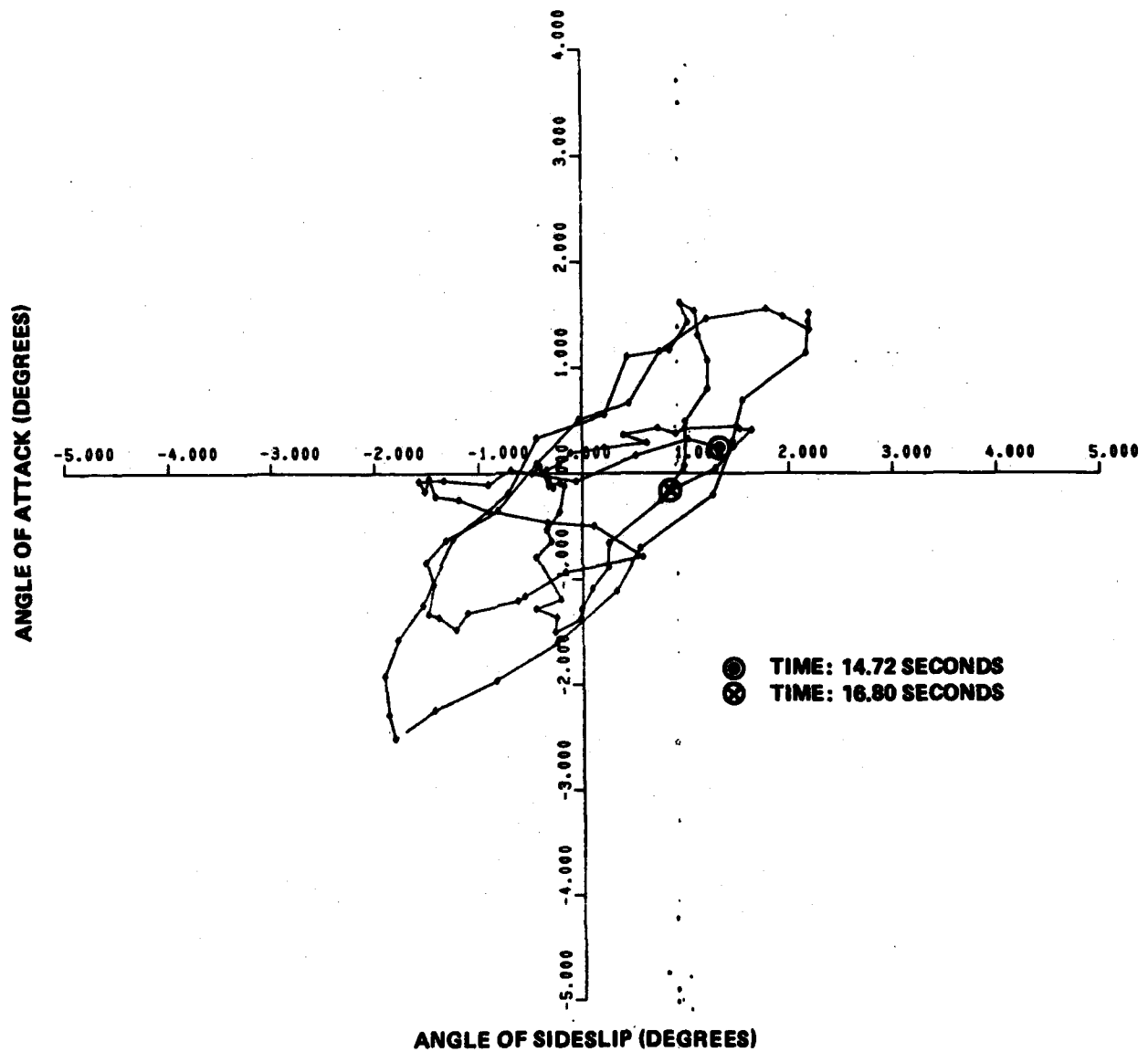


FIGURE 10 (i) ANGLE OF ATTACK VERSUS ANGLE OF SIDESLIP FOR TIME INTERVAL 14.72 TO 16.80 SECONDS (HEMI-SPHERICAL NOSE)

The records $\alpha(t_1)$ and $\beta(t_1)$ were read into the computer in line 350 (see Table 2. The program was iterated 50 times. The last 20 iterative steps are given in Table 5.

A few remarks may be made concerning the final values from the data reduction program. From the discussion in Section 3, it will be recalled that the constants A_1, B_1, A_2, B_2 are of no value in obtaining the aerodynamic stability derivatives. From equation (14) it is possible to calculate trim angle. Applying this equation to the values of A_3 and B_3 of Table 5 it is possible to calculate the trim angle, α_T , as 1.12 degrees. Initially this is surprising since the NAW wind tunnel model does not have any apparent configurational asymmetries. The apparent trim angle is nothing more than an error in the background fiducial marking used for frame alignment.

The frequency and damping constants, $W1, W2, L1, L2$ are of value in computing the three aerodynamic derivatives and the spin rate. Inserting these values as appropriate in the program of Table 3 gives the derivatives presented in Table 4.

The static pitching moment derivative $C_{m\alpha}$ of $-.328$ is the value of this derivative applicable to a non-ablating, spinning conical model (7-degree half angle, 0.223 nose bluntness) undergoing bi-planar angular motion. The location of the static center of pressure aft of the nose (fractions of body length, L) is given by the following:

$$\frac{X}{L} = \frac{C_{m\alpha}}{C_{N\alpha}} \frac{D}{L} + 0.595 \quad (38)$$

With the body length of 19.79 and body diameter of 6.054 inches, $C_{m\alpha}$ as $-.328$ and $C_{N\alpha}$ of 1.35 the center of pressure is 0.669 body lengths aft of the nose and 0.0743 body lengths aft of the c.g. There is no published data applicable to this configuration at a Mach number of 7.95. However, reproduced from an unclassified source is

TABLE 5
DATA REDUCTION FOR DATA POINTS 1 TO 900 FOR SPHERE CONE MODEL.

STAND.DEV.-E	PREC-FREQ	NU-FREQ	PREC-DAMP	NU-DAMP
.294289	10.3601	-14.2185	-2.65331E-2	-2.06467E-2
.294178	10.3601	-14.2175	-2.62024E-2	-2.10517E-2
.294124	10.3602	-14.2167	-2.59674E-2	-2.12998E-2
.294097	10.3602	-14.2162	-2.58002E-2	-2.14477E-2
.294084	10.3602	-14.2158	-2.56809E-2	-2.15323E-2
.294078	10.3601	-14.2155	-2.55957E-2	-2.15779E-2
.294074	10.3601	-14.2153	-2.55348E-2	-2.15999E-2
.294073	10.3601	-14.2152	-2.54913E-2	-2.16081E-2
.294072	10.3601	-14.2151	-.02546	-2.16085E-2
.294072	10.3601	-14.215	-2.54377E-2	-.021605
.294071	10.3601	-14.215	-2.54216E-2	-2.15997E-2
.294071	10.3601	-14.2149	-2.54101E-2	-2.15939E-2
.294071	10.3601	-14.2149	-2.54018E-2	-2.15883E-2
.294071	10.3601	-14.2149	-2.53958E-2	-2.15833E-2
.294071	10.3601	-14.2149	-2.53915E-2	-2.15789E-2
.294071	10.3601	-14.2149	-2.53884E-2	-2.15752E-2
.294071	10.3601	-14.2149	-2.53862E-2	-2.15722E-2
.294071	10.3601	-14.2149	-2.53846E-2	-2.15697E-2
.294071	10.3601	-14.2148	-2.53834E-2	-2.15677E-2
.294071	10.3601	-14.2148	-2.53826E-2	-2.15661E-2
A1	B1	A2	B2	A3
.328411	1.74525	.461837	1.12199	.017397
B3	W1	W2	L1	L2
-9.10809E-3	10.3601	-14.2148	-2.53826E-2	-2.15661E-2

TABLE 6
NON-DIMENSIONAL AERODYNAMIC COEFFICIENTS AND SPIN RATE FOR DATA POINTS 1 TO 900.
(SPHERE-CONE MODEL)

STATIC CMA	DYNAMIC CMB	MAGNUS CNPA	SPIN P(RAD/SEC)	C.P. X(BODY-LENGTH)
-.328249	-1.4462	.160737	29.9689	7.43787E-2

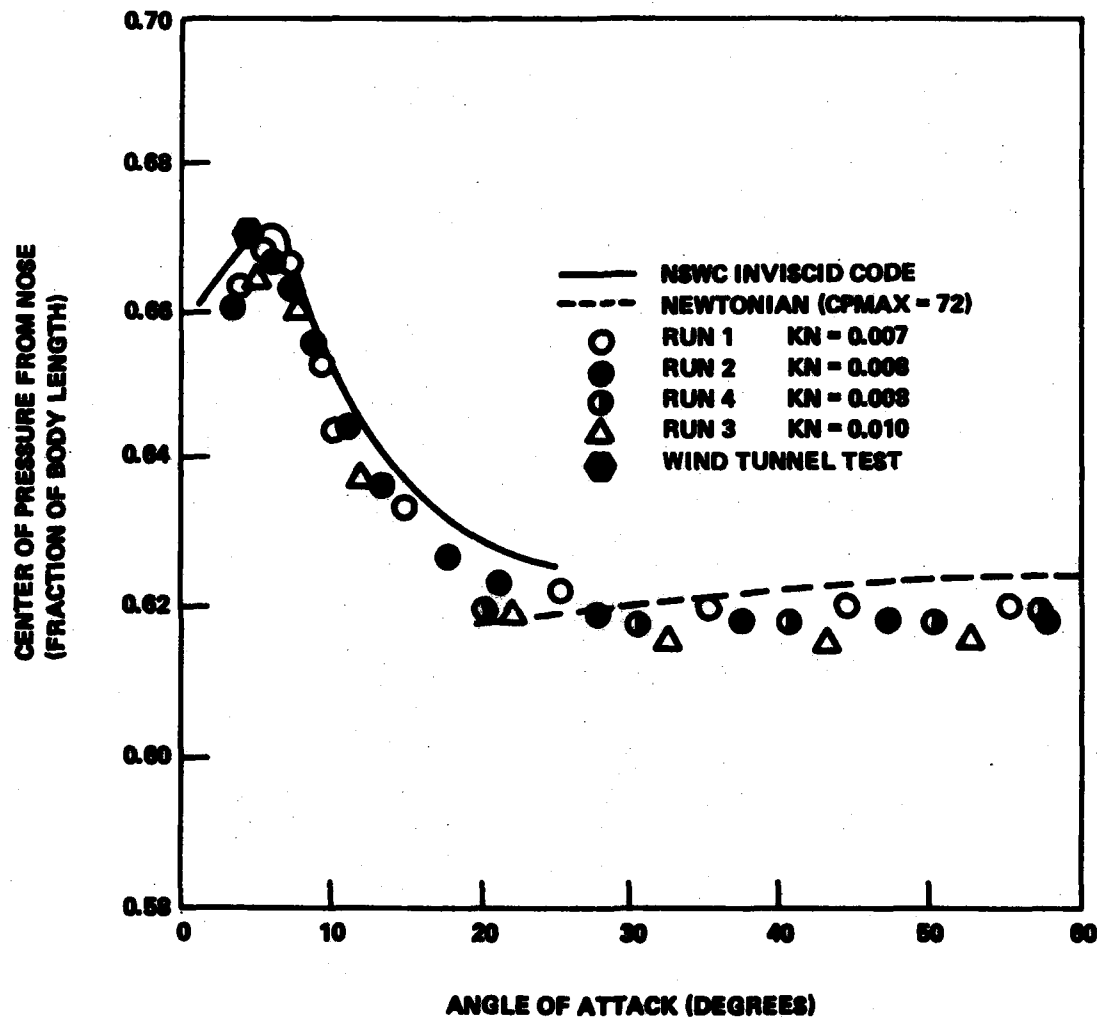


FIGURE 11 PLOTTED FORCE DATA FOR $r_N/r_B = 0.223$ CONFIGURATION WITH STRAIGHT STING

data for this configuration at Mach 10. These data have been reproduced in Figure 11.

It will be noted that the furthest aft that the center of pressure reaches is about 0.67 body lengths. As just noted, the center of pressure measured in these dynamic tests is at 0.669. It is not possible to compare the static (constrained) test results with the dynamic test results since the angle of attack was continuously changing during the dynamic tests. Nevertheless the dynamic testing took place over an angle of attack range of about 3 degrees. Taking an r.m.s. value of angle of attack at something like 2 degrees, it may be seen that correlation of the center of pressure between the two testing techniques is quite satisfactory.

4.2 ABLATING NOSE (AN) WIND TUNNEL TESTS. The Three-Degree-of-Freedom Gas Bearing may be used to study the dynamic motion of a model undergoing surface ablation. Ablation was confined to the hemispherical nose by replacing the steel nose by a camphor hemispherical nose molded over a steel bi-conic substructure. This substructure is shown in Figure 12. The particular shape of this substructure was derived from earlier experimentation, reference (6).

In these wind tunnel tests the low temperature-ablating nose was attached to the model. The testing procedure followed along the lines described in sections 4.0 and 4.4. Photographs were made of the ablating nose throughout the 20 seconds duration of the erosion. Eight sequences in the ablation process are shown in

⁵ Ragsdale, W.C., et al, "Mach 10 IAP Static Force Test Program in the NSWC/WOL Hypersonic Tunnel (WTR 1296)," NSWC/WOL MP 77-33, September 1977.

⁶ Jobe, M.D., et al, "Bi-Modal Flow Field Feasibility Demonstration in the NSWC/WO Hypersonic Tunnel (WTR 1319)," NSWC MP 79-217, May 1979.

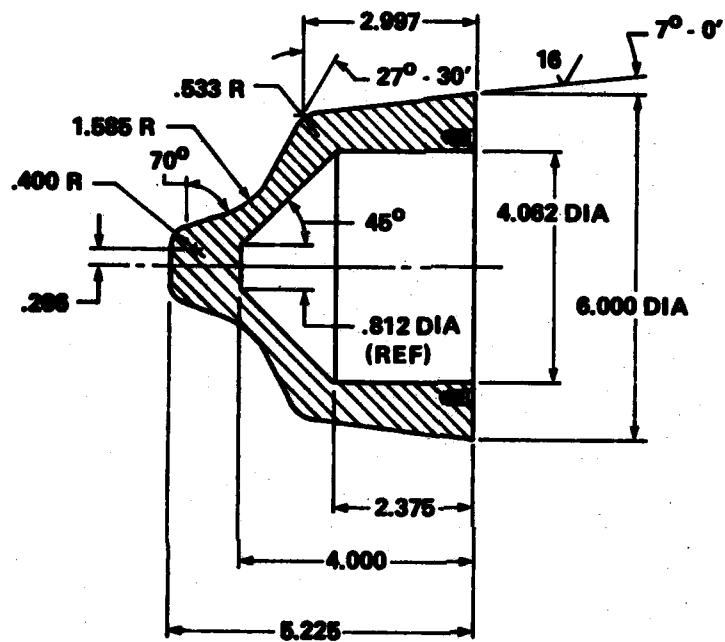


FIGURE 12 ABLATING NOSE SUBSTRUCTURE

Figure 13. Each photograph depicts phenomenon about 2.5 seconds apart. Although not evident in these photographs, the model is undergoing simultaneous pitch, yaw and spin. It may be seen that the ablating shape approaches the bi-conic sub-structure illustrated in Figure 12.

The significant difference between the sphere-cone model and the ablating model is the continuously changing nose shape associated with the ablating model. Changing configuration means that the various aerodynamic derivatives are also continuously changing during the ablation process.

As in the case of the previously discussed sphere-cone test, primary data consists of the triplets (α_1, β_1, t_1) where α_1 and β_1 are the angles of attack and sideslip measured at time t_1 . Probably the most straight forward way of presenting (α_1, β_1, t_1) data points is as a time history. This has been done in Figure 14. As pointed out earlier, the two orthogonal cameras are not synchronized. Since there are some differences in framing rate between the two cameras, the records α_1 and β_1 are not at the same time, t_1 . The data reduction program does require the two angle pairs be at the same value of time. Thus, it is necessary to interpolate one angle record to bring it into coincidence with the other. In the angular history presented in Figures 14, the sideslip record, β_1 , is interpolated to coincide with the angle of attack record, α_1 .

Figures 15 are an alternate form of representing α_1, β_1 . These "petal" plots are given at about 2.0 second intervals. The start of each record is indicated by the symbol \odot and the end by the symbol \otimes . A quick perusal of Figures 15 indicates slight damping until about 10 seconds (Figure 15f). The succeeding figures seem to indicate a slight increase of the angular displacement magnitude. In the reduced data one would expect to find changes in sign of the damping-in-pitch derivative, C_{m_q} .

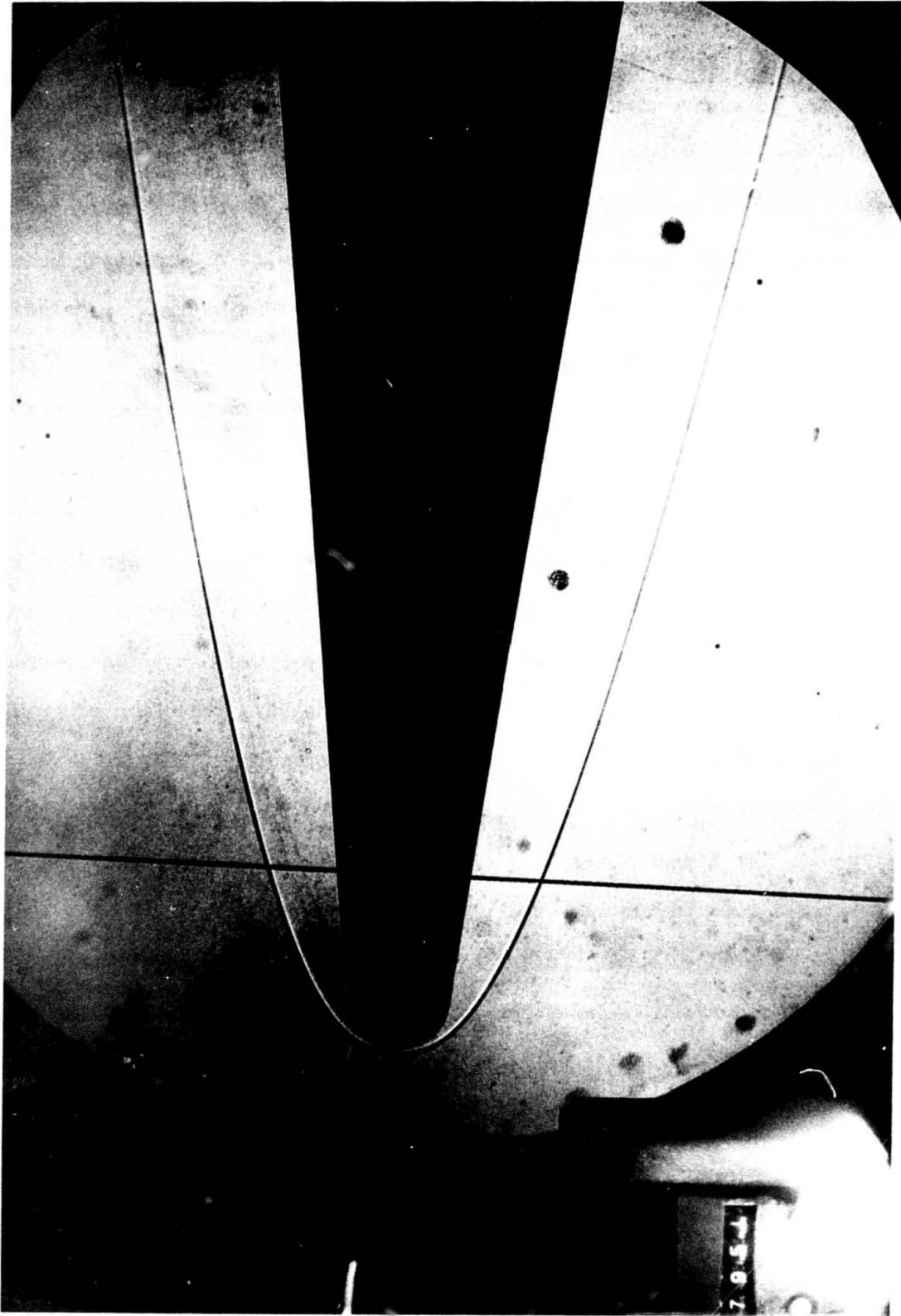


FIGURE 13 NOSE ABLATION SEQUENCE

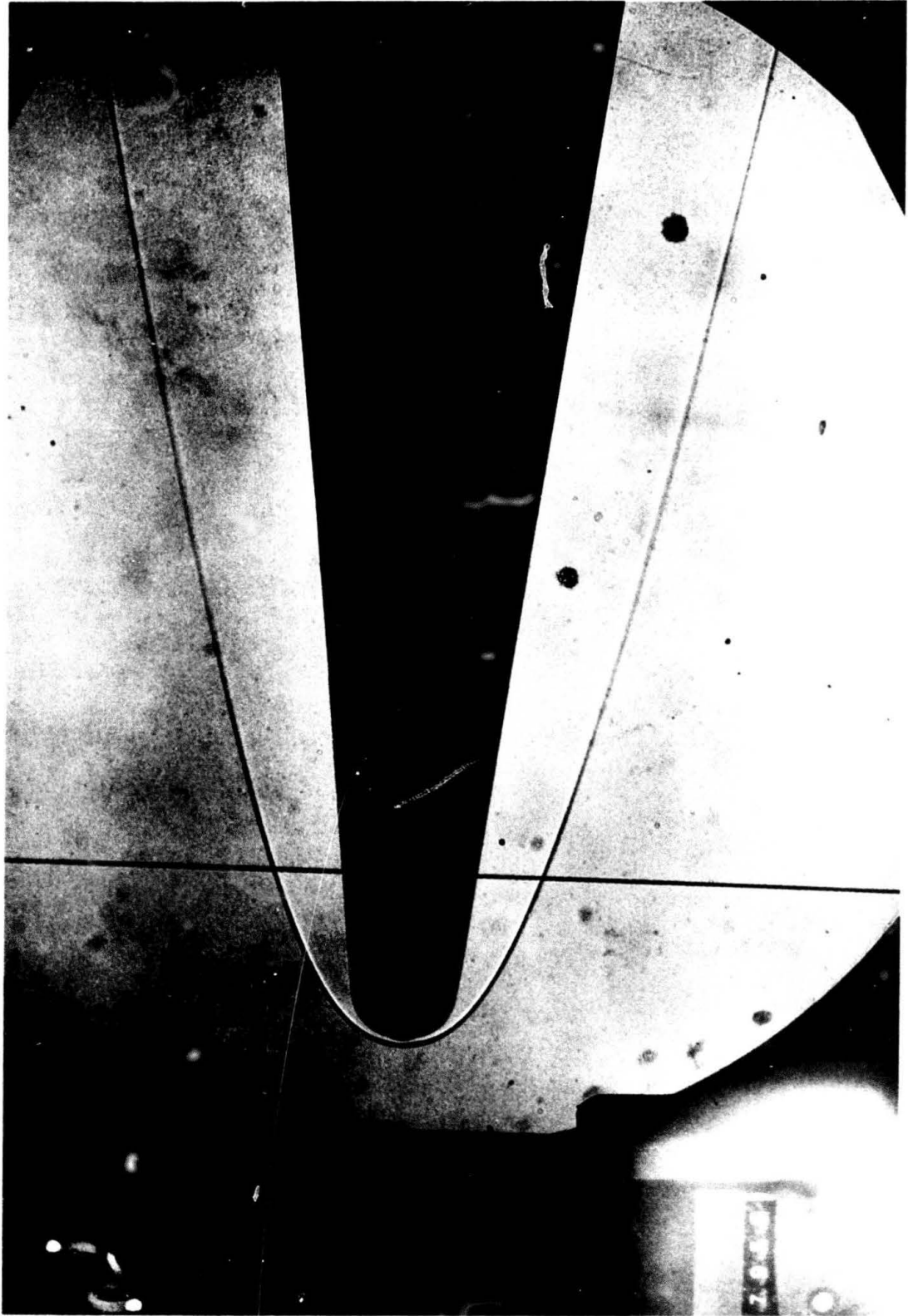


FIGURE 13 (CONTINUED)

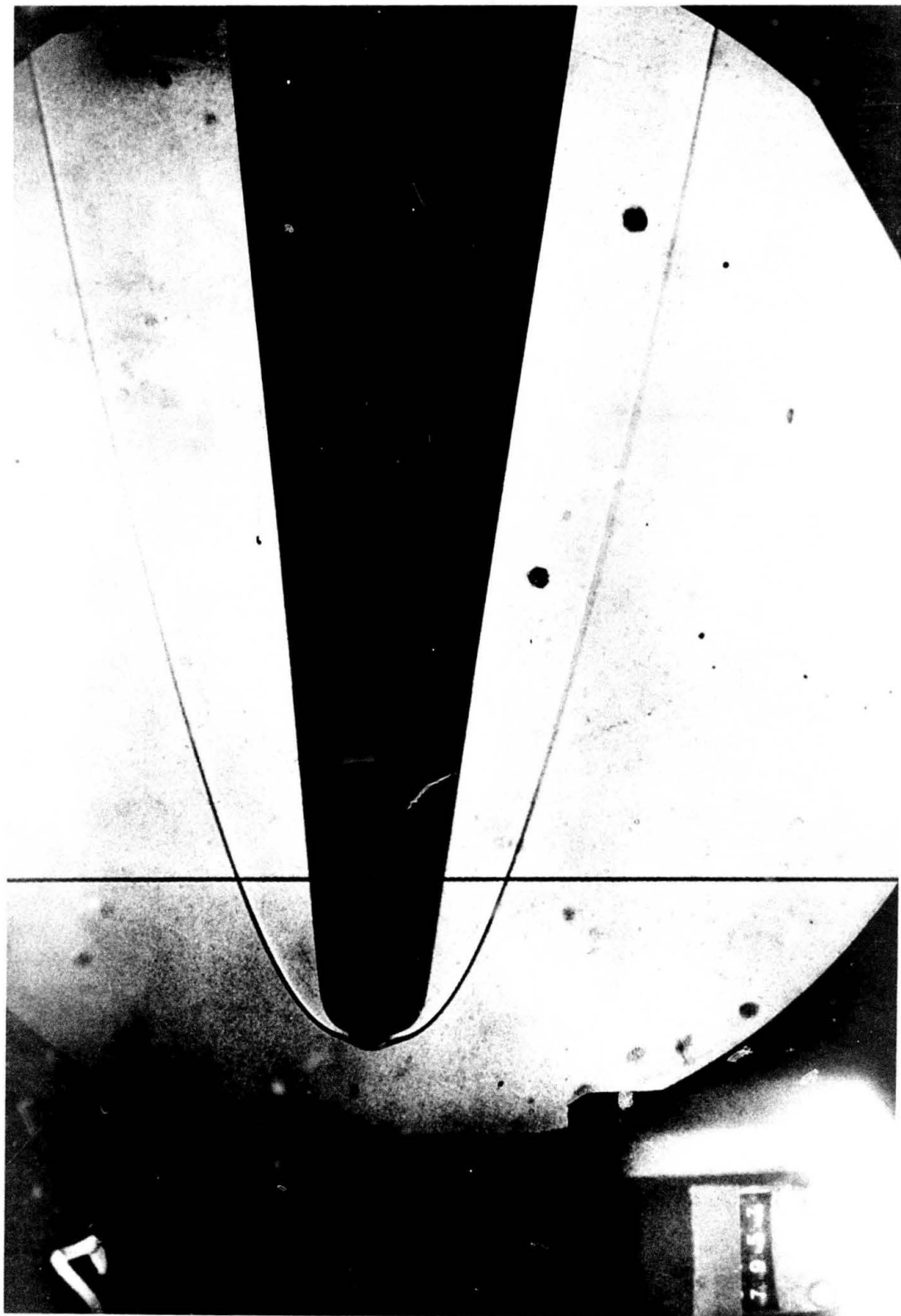


FIGURE 13 (CONTINUED)

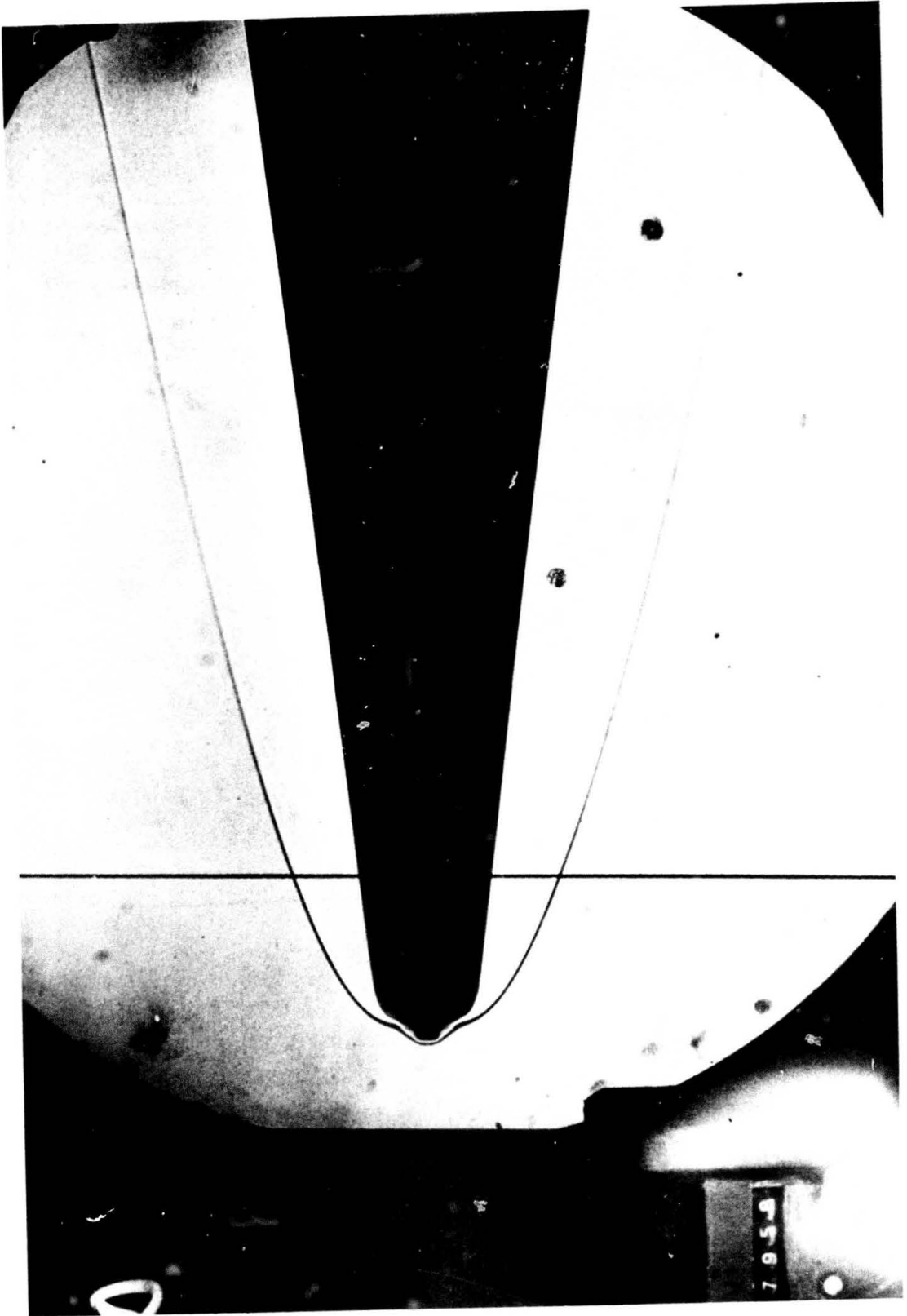


FIGURE 13 (CONTINUED)

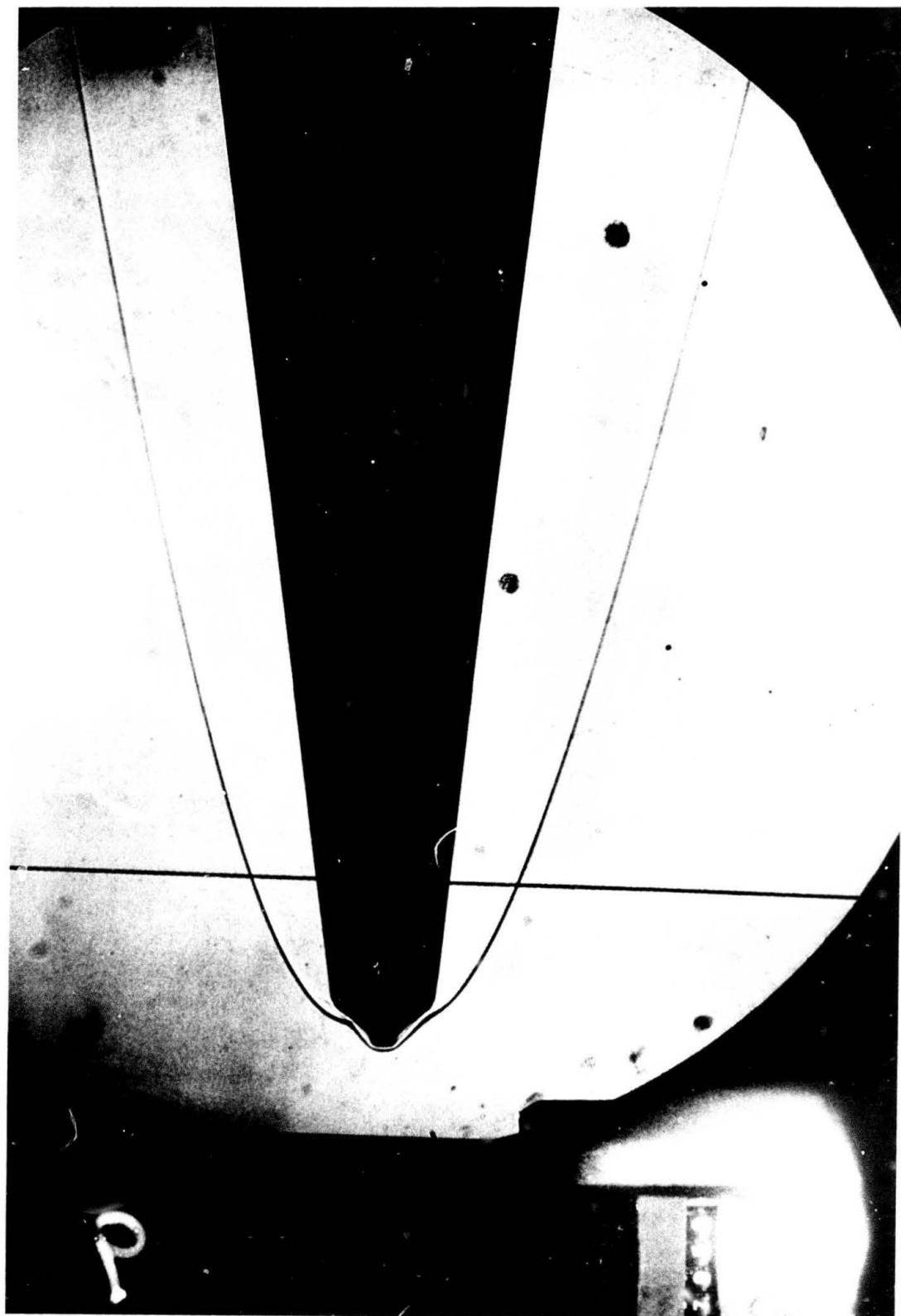


FIGURE 13 (CONTINUED)

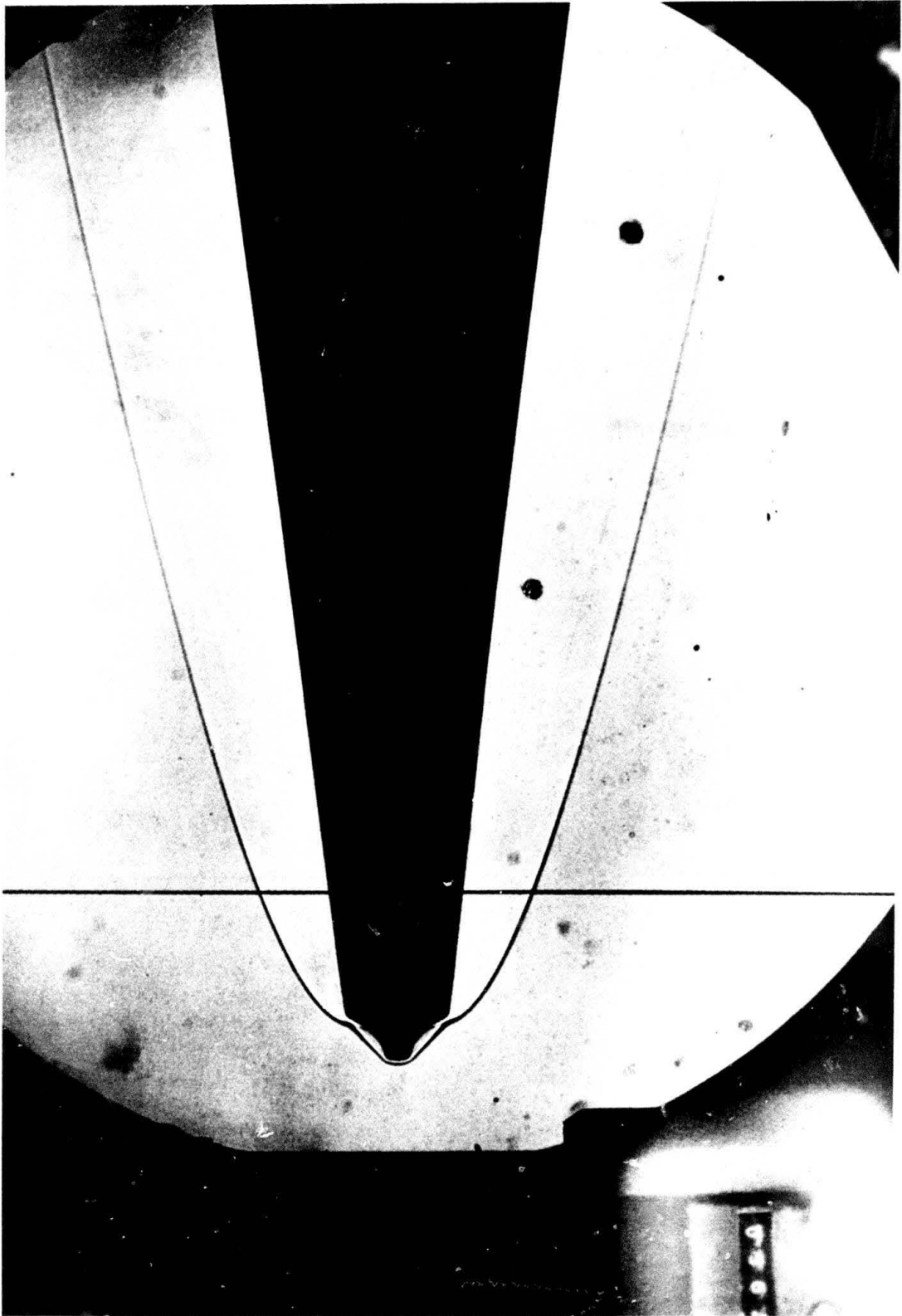


FIGURE 13 (CONTINUED)



FIGURE 13 (CONTINUED)

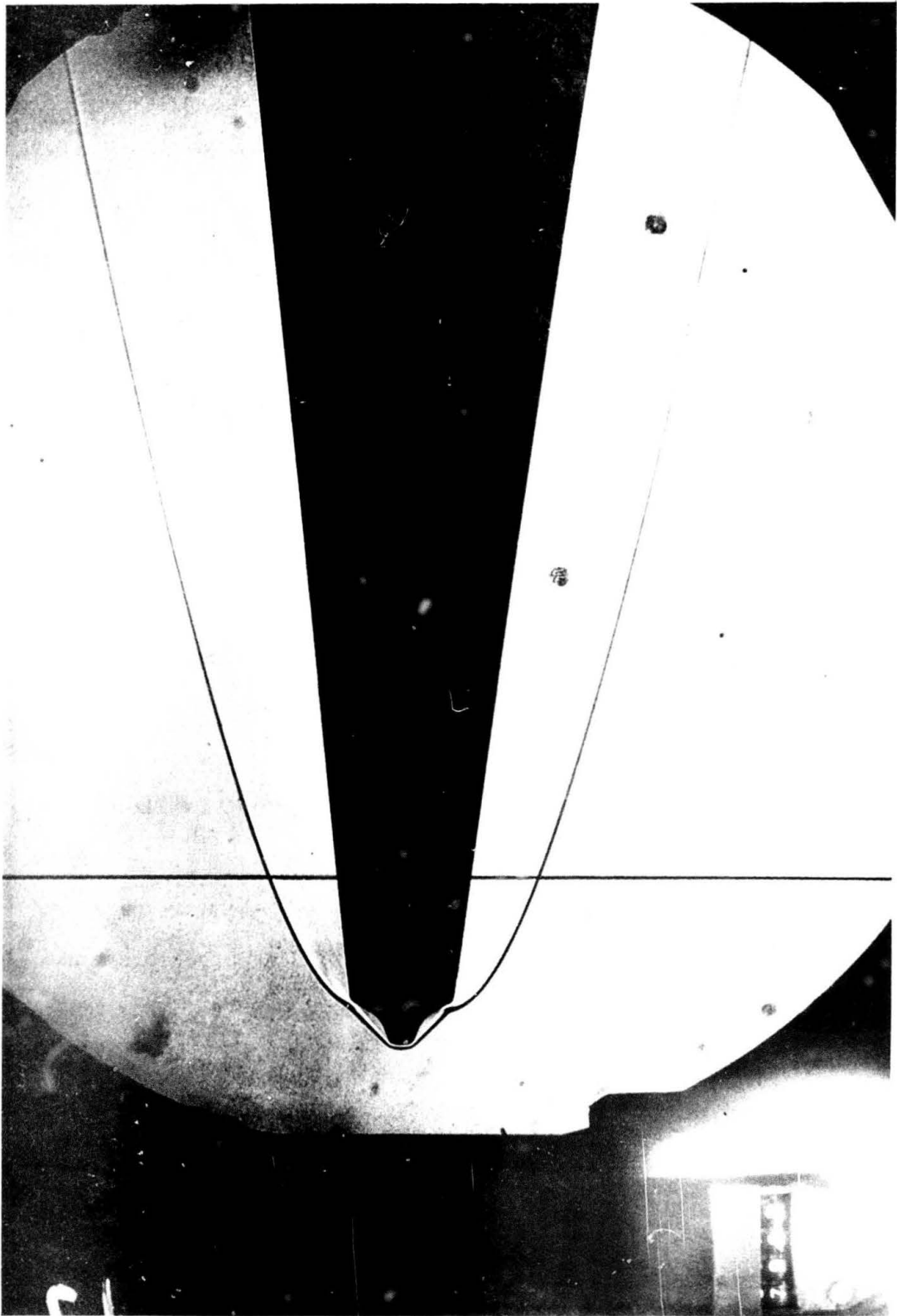


FIGURE 13 (CONTINUED)

In the first reduction of these data the whole record of about 750 data points was divided into sub-intervals of about 50 data points each. Each data point is characterized by the triplets, (α_1, β_1, t_1) , i.e. angle of attack, angle of side slip and time. A data record of 50 data points has a time duration of about one second as has been pointed out. Thus, each petal figure consists of about 100 data points. An examination of the aerodynamic derivatives reduced from these successive, non-overlapping sub-records did indicate a fairly consistent monotonic reduction with time of the static moment derivative, $C_{m\alpha}$. If a constant value is assumed for the normal force derivative, $C_{N\alpha}$, the preceding observation is equivalent to recognizing that the center of pressure moves steadily forward with time. The equivalent statement is that the center of pressure moves forward as the model ablates from a sphere cone to the symmetrical substructure illustrated in Figure 12. As will be seen, the center of pressure moves from a point 0.073 body lengths (or so) aft of the c.g. to a point 0.054 body lengths aft of the c.g. As far as dynamic measurements are concerned it is felt that less than three significant figure accuracy in measurements from the film record combined with low dynamic pressure compromised reliable dynamic data. In addition there is an indication from the petal plots of Figures 15 that there are regions of both damped and undamped motion. From the reduction of the 50-point records the damping in pitch derivative, C_{mq} , varied considerably in both magnitude and sign. Sign changes (from negative to positive) can be used to qualitatively indicate periods of damped and undamped motion.

In order to examine the dynamic measurements in more detail it was decided to apply the data reduction method to overlapping records, still 50 data points in length. This examination using overlapping records was confined to the beginning of the ablation record. Thus, records of data points 1-50, 5-55, 10-60, etc., were reduced. The results of this data reduction, both the

ANGLE OF ATTACK —————
 ANGLE OF SIDESLIP - - - - -
 TIME: 0 TO 5 SECONDS

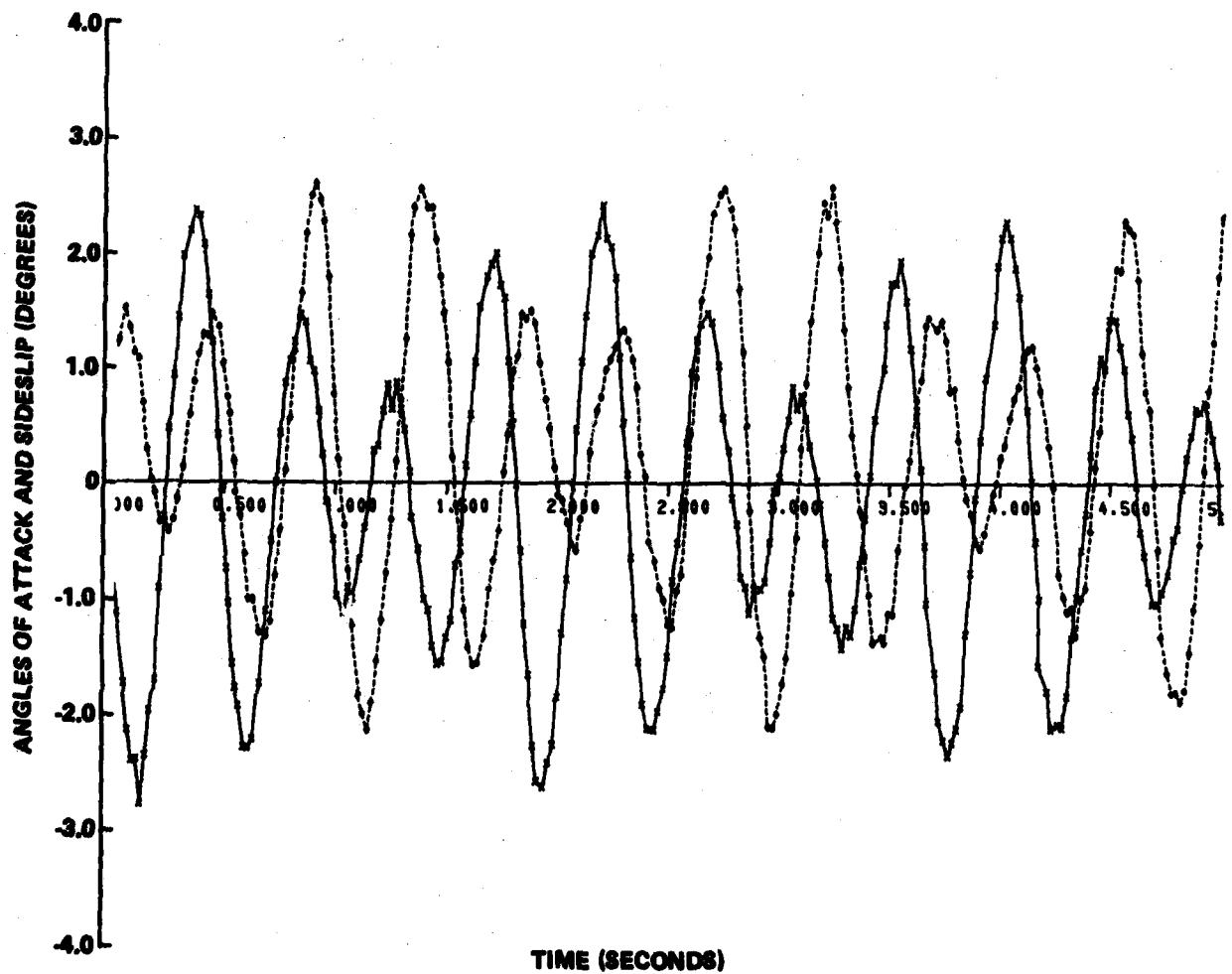


FIGURE 14 (a) ANGLES OF ATTACK AND SIDESLIP VERSUS TIME
 (ABLATING NOSE)

ANGLE OF ATTACK —————
ANGLE OF SIDESLIP - - - - -
TIME: 5 TO 10 SECONDS

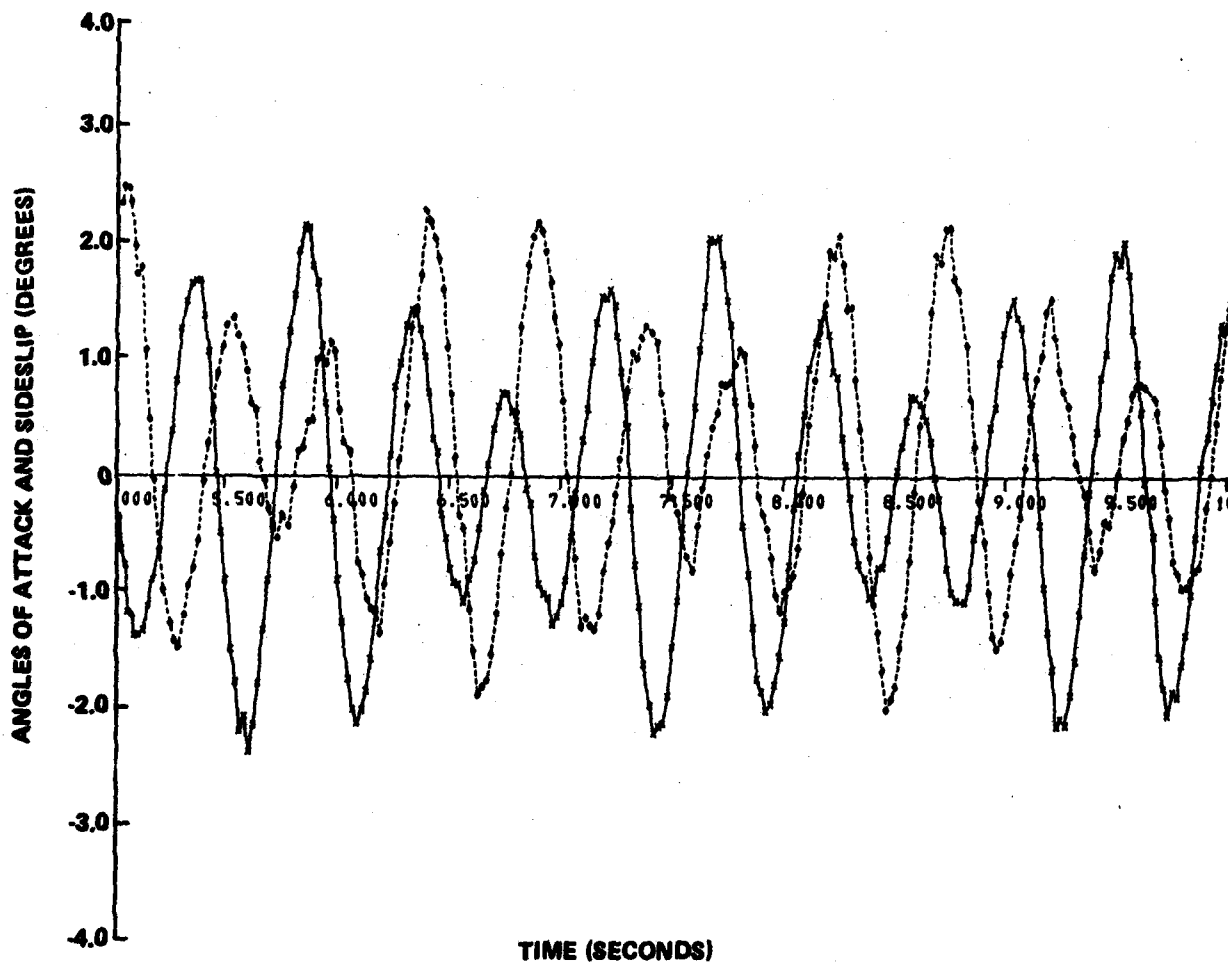


FIGURE 14 (b) ANGLES OF ATTACK AND SIDESLIP VERSUS TIME
(ABLATING NOSE)

ANGLE OF ATTACK —————
 ANGLE OF SIDESLIP - - - - -
 TIME: 10 TO 15 SECONDS

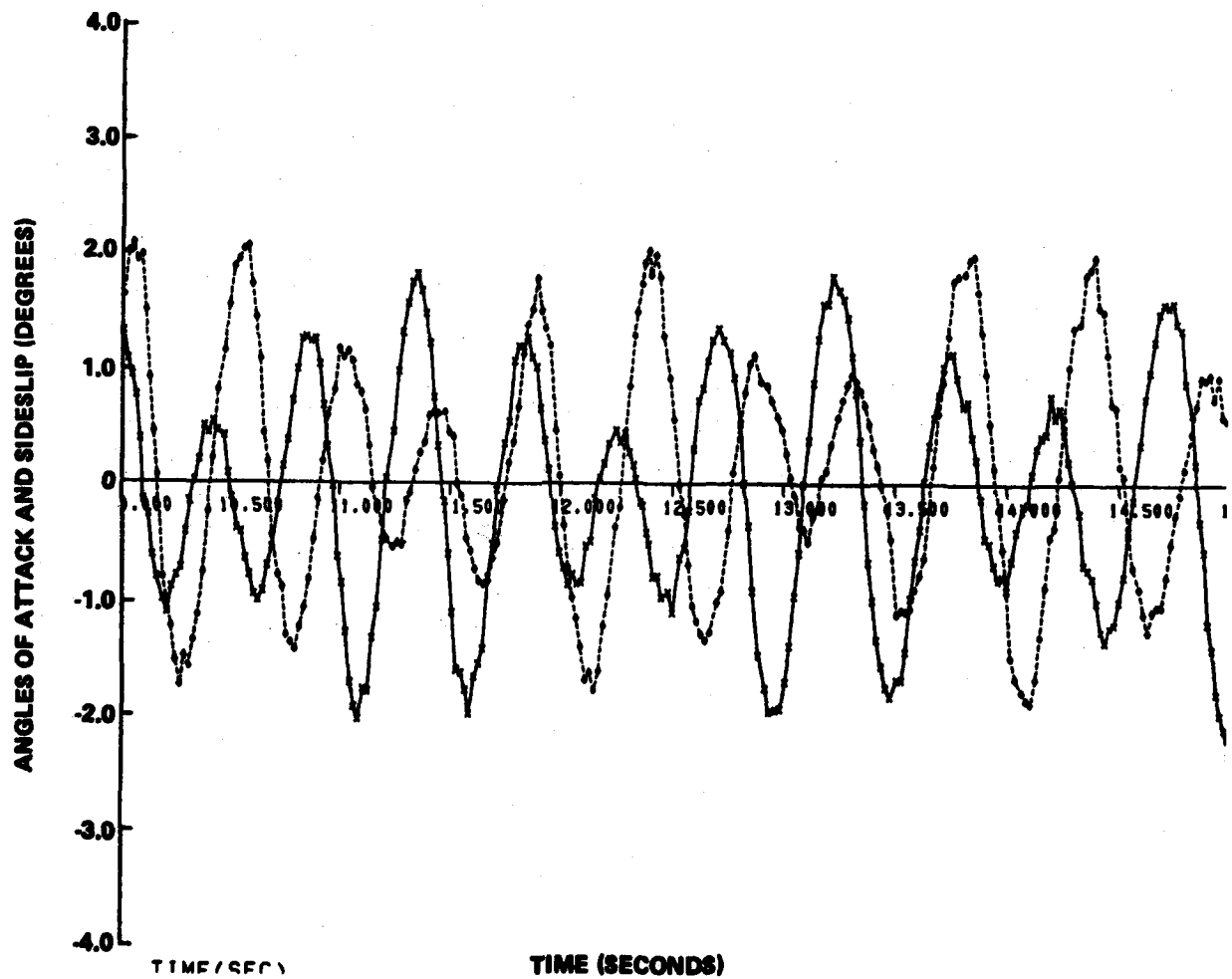


FIGURE 14 (a) ANGLES OF ATTACK AND SIDESLIP VERSUS TIME
 (ABLATING NOSE)

ANGLE OF ATTACK —————
 ANGLE OF SIDESLIP - - - - -
 TIME: 15 TO 20 SECONDS

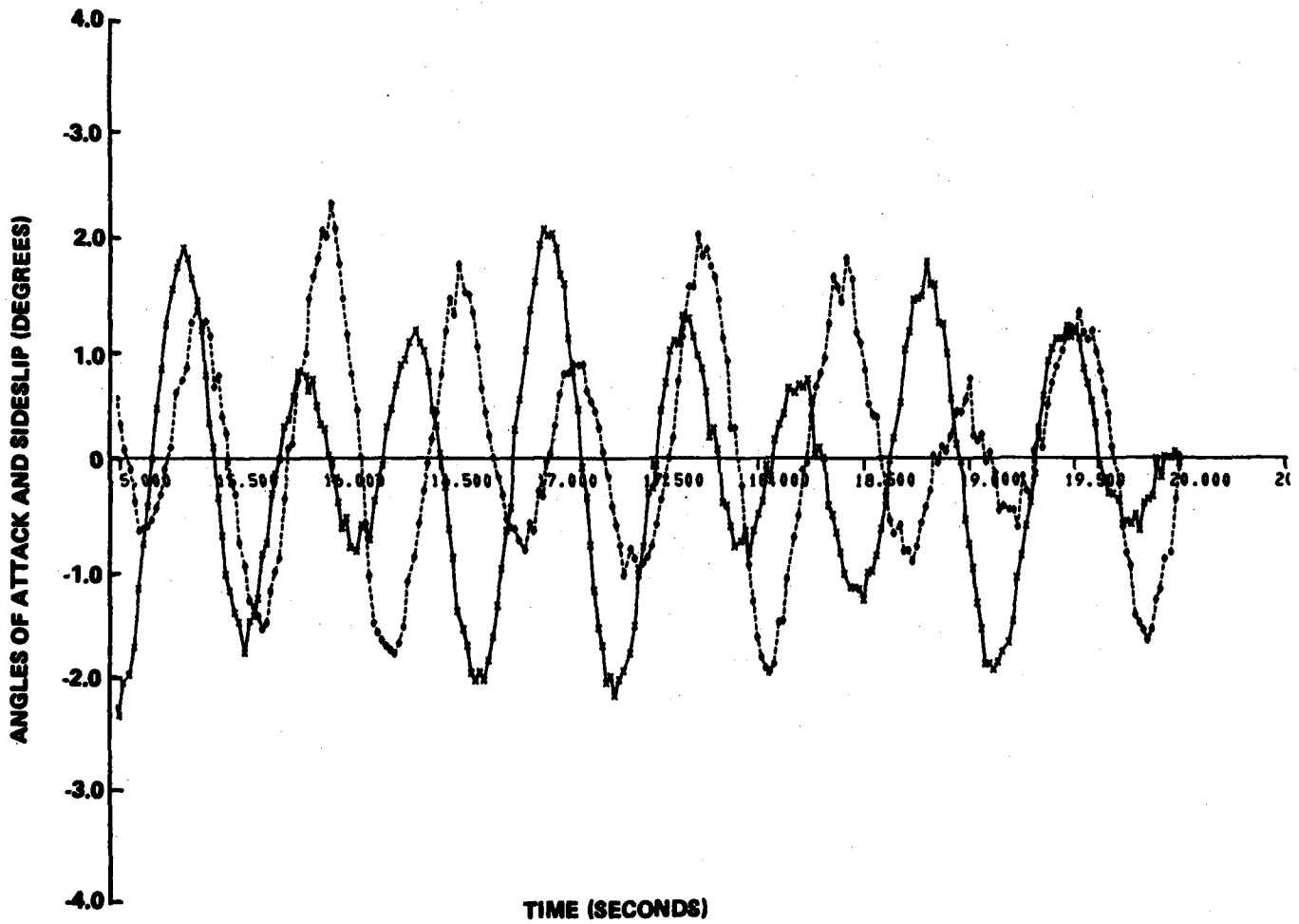


FIGURE 14 (d) ANGLES OF ATTACK AND SIDESLIP VERSUS TIME
 (ABLATING NOSL.)

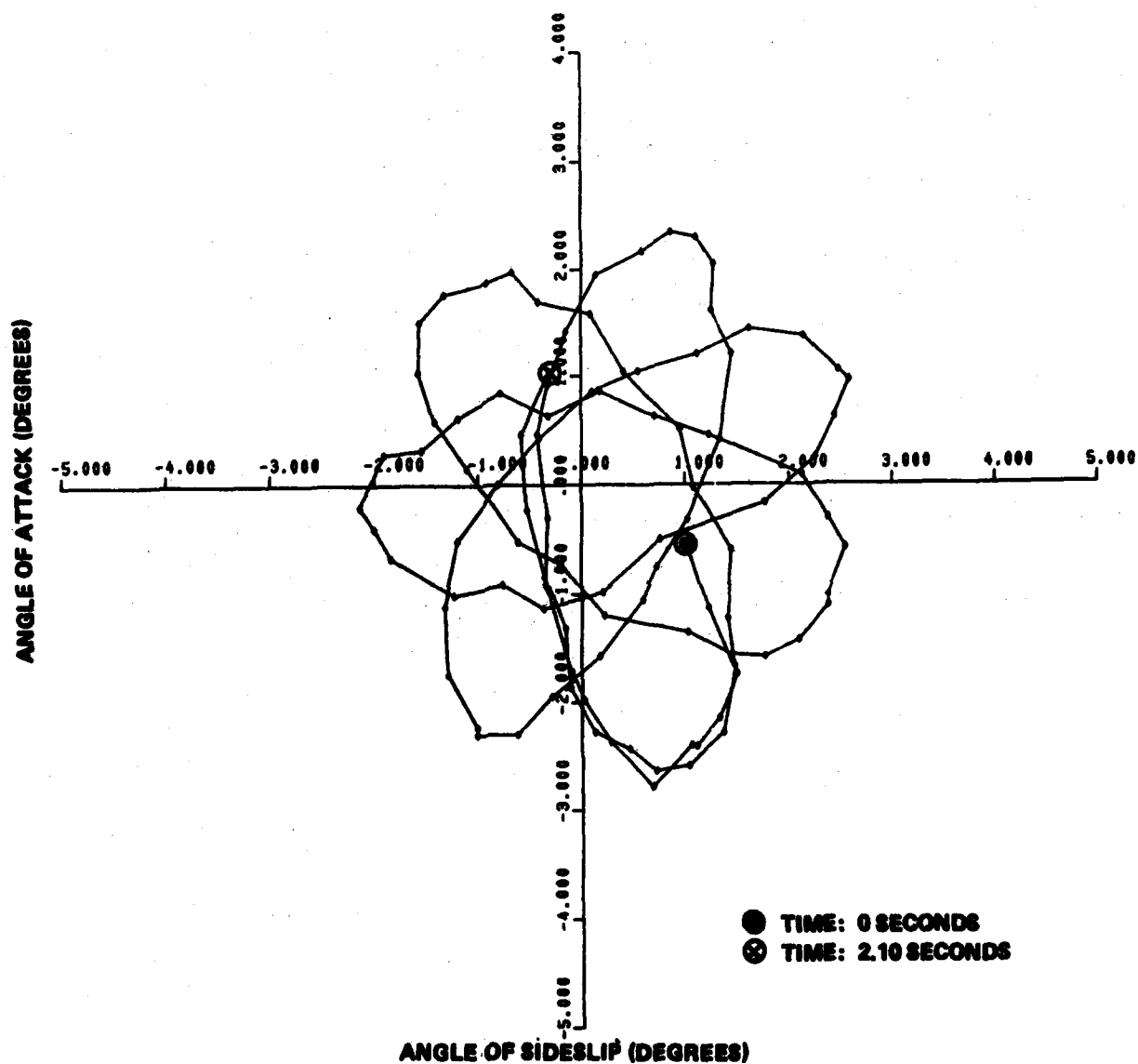


FIGURE 15 (a) ANGLE OF ATTACK VERSUS ANGLE OF SIDE SLIP FOR TIME INTERVAL 0 TO 2.10 SECONDS (ABLATING NOSE)

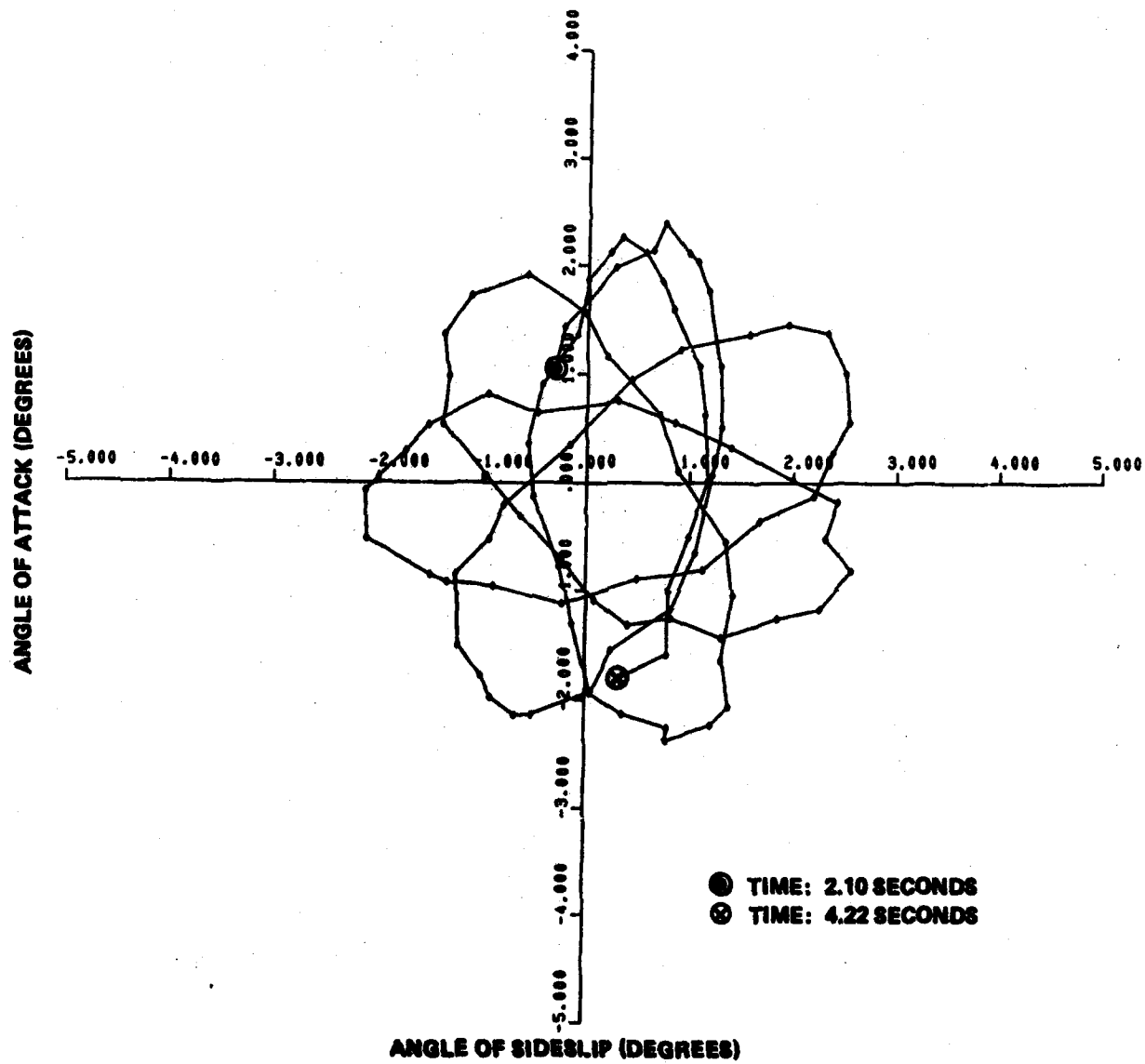


FIGURE 15 (b) ANGLE OF ATTACK VERSUS ANGLE OF SIDE SLIP FOR TIME INTERVAL 2.10 TO 4.22 SECONDS (ABLATING NOSE)

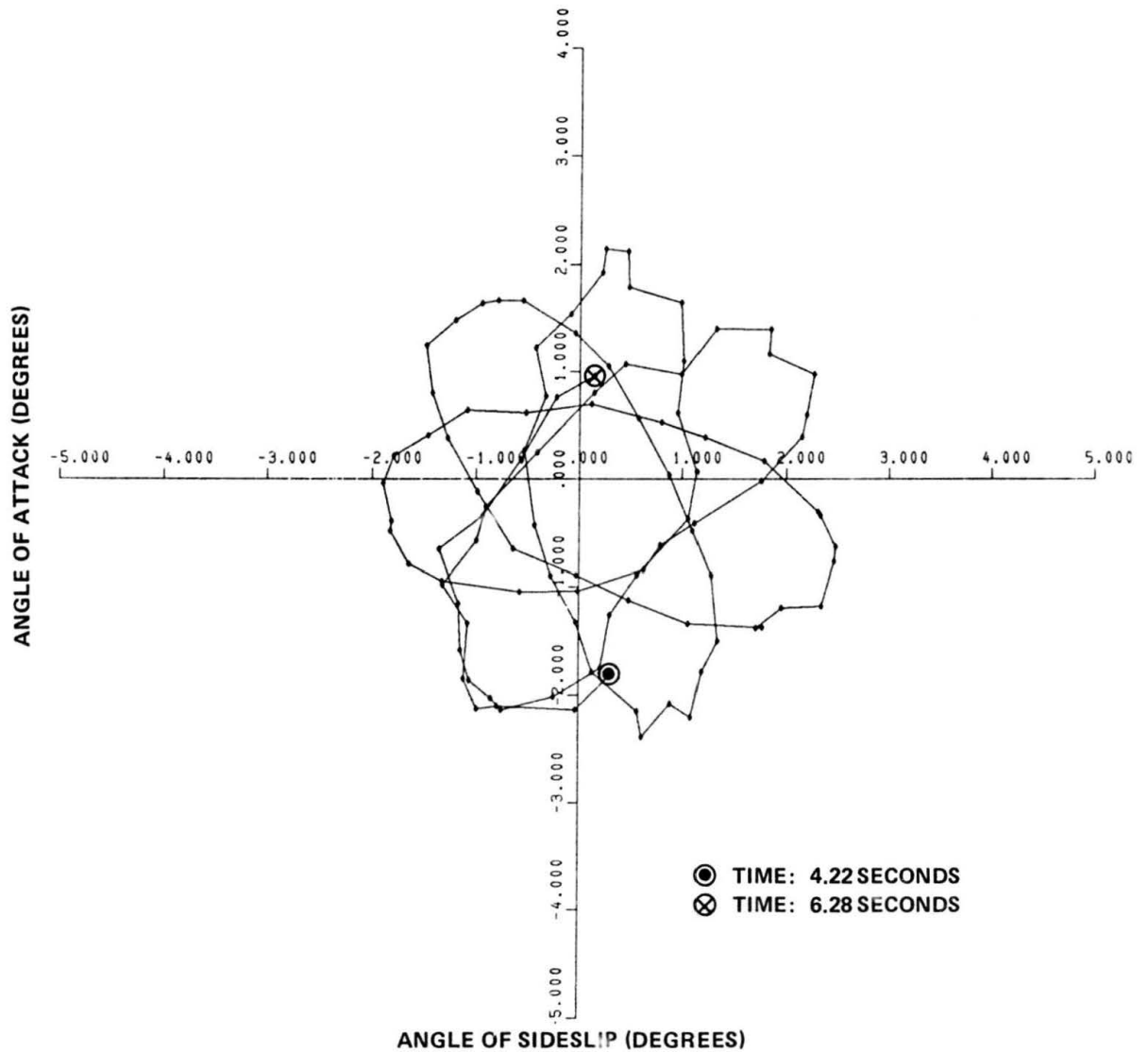


FIGURE 15 (c) ANGLE OF ATTACK VERSUS ANGLE OF SIDE SLIP FOR TIME INTERVAL 4.22 TO 6.28 SECONDS (ABLATING NOSE)

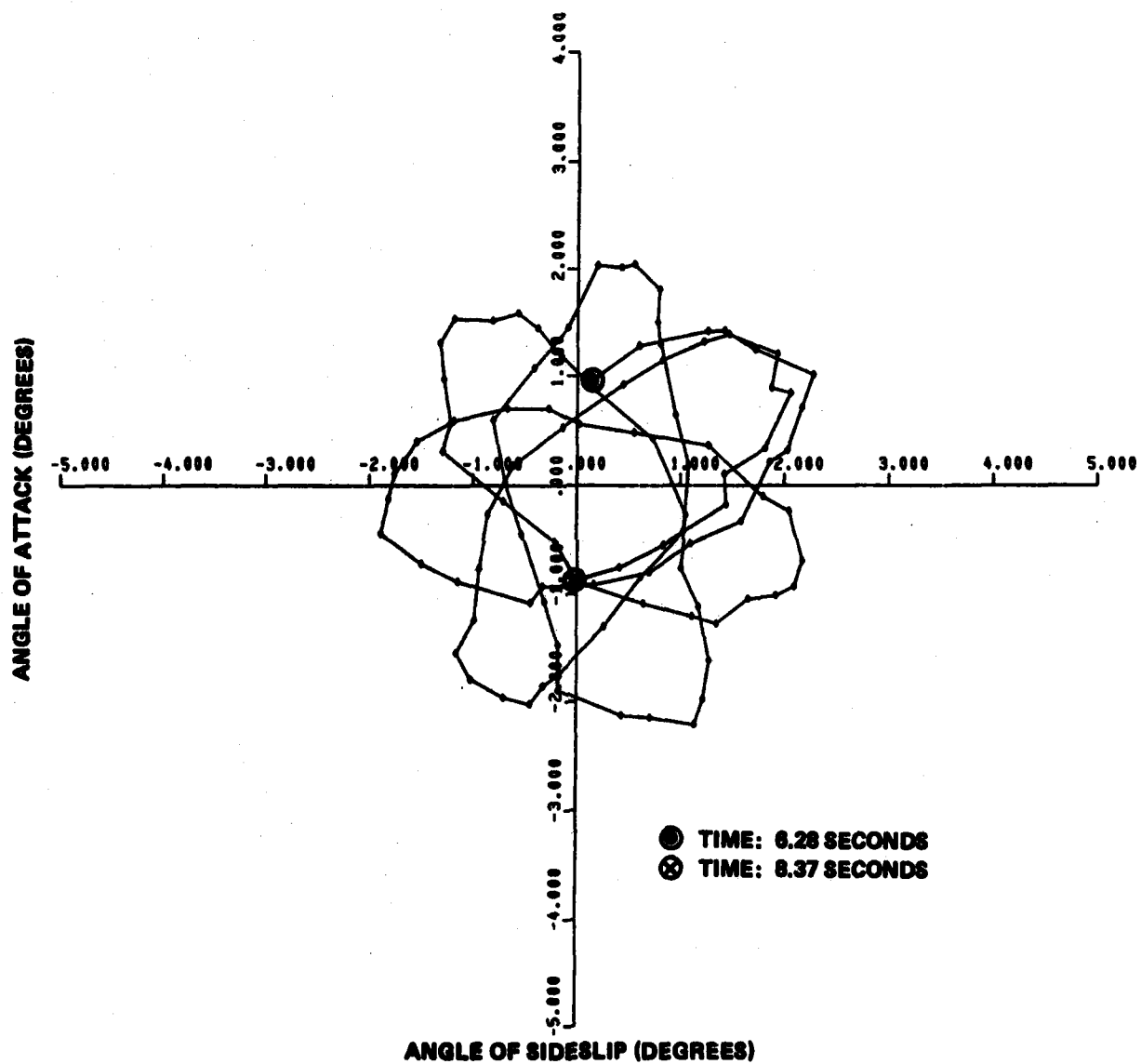


FIGURE 18 (d) ANGLE OF ATTACK VERSUS ANGLE OF SIDE SLIP FOR TIME INTERVAL 6.28 TO 8.37 SECONDS (ABLATING NOSE)

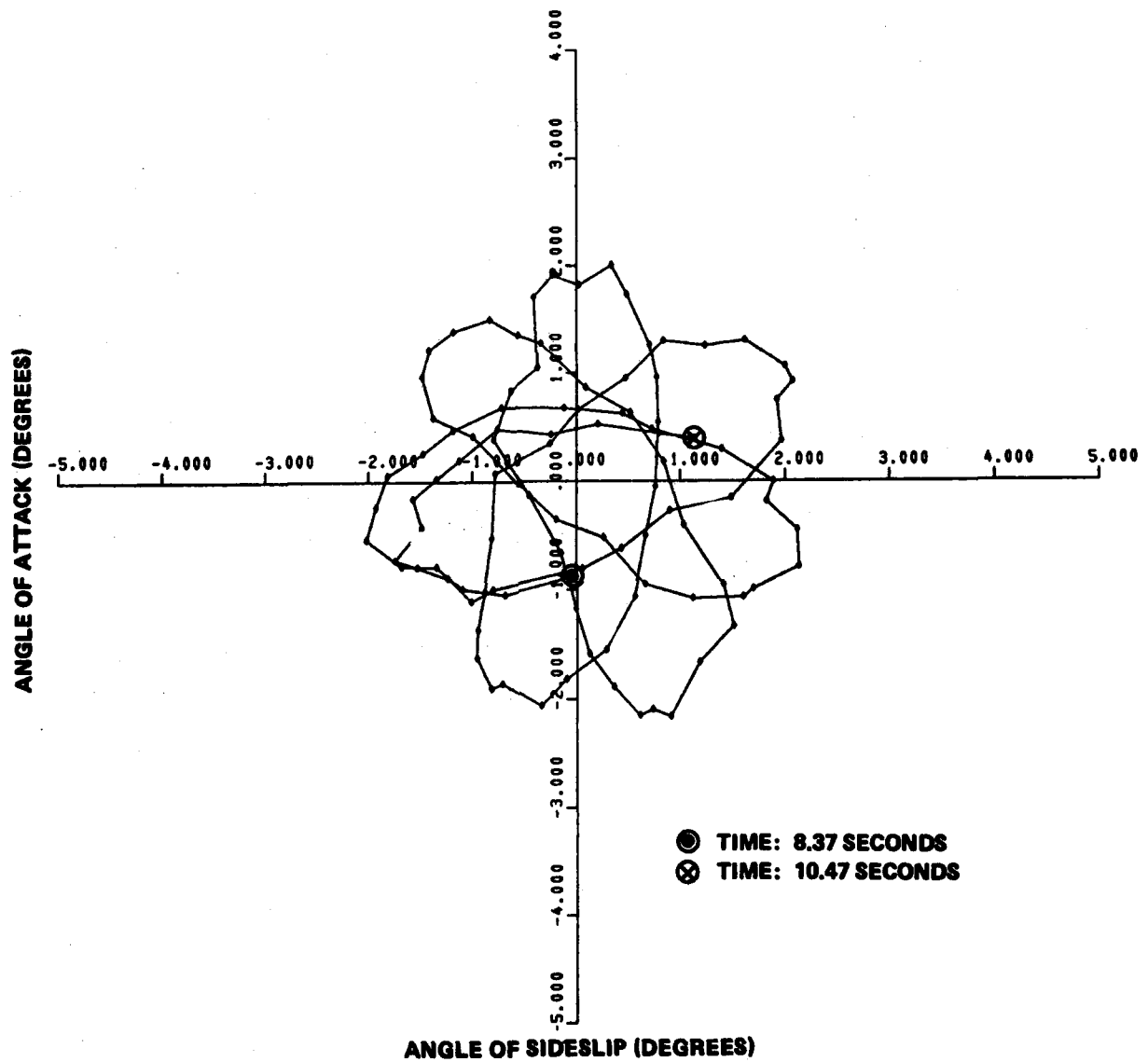


FIGURE 15 (a) ANGLE OF ATTACK VERSUS ANGLE OF SIDE SLIP FOR TIME INTERVAL 8.37 TO 10.47 SECONDS (ABLATING NOSE)

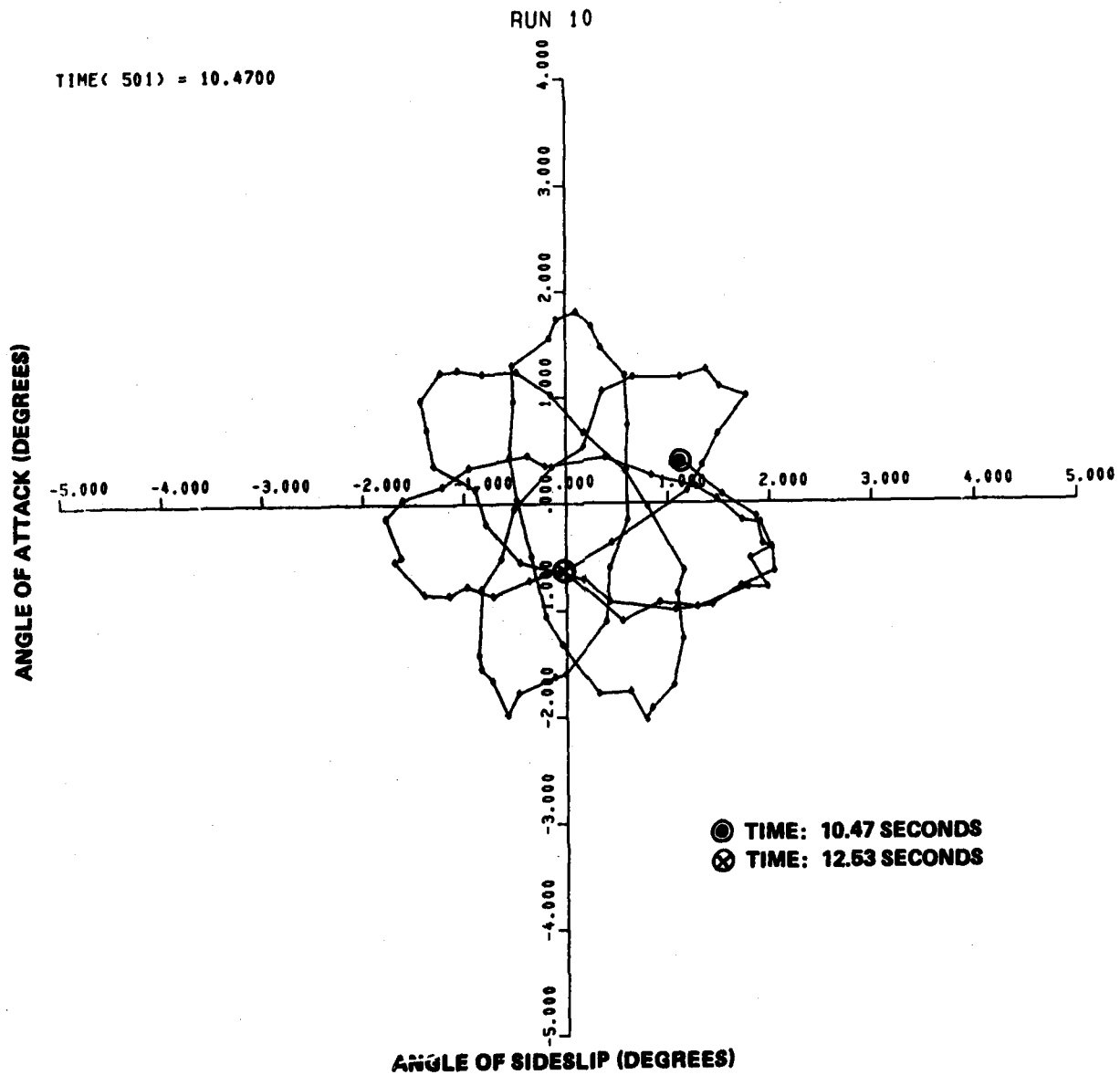


FIGURE 15 (f) ANGLE OF ATTACK VERSUS ANGLE OF SIDE SLIP FOR TIME INTERVAL 10.47 TO 12.53 SECONDS (ABLATING NOSE)

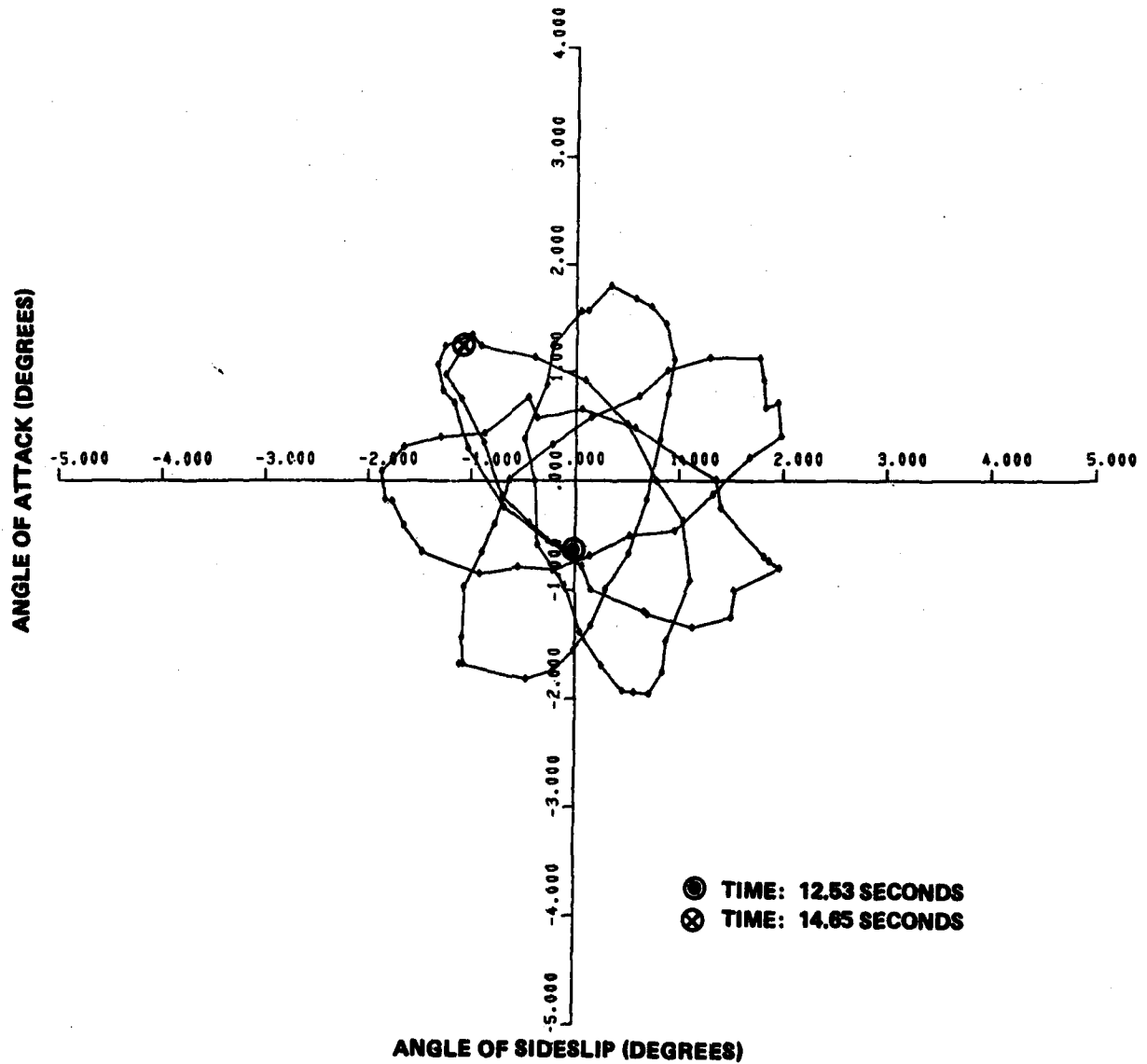


FIGURE 15 (p) ANGLE OF ATTACK VERSUS ANGLE OF SIDE SLIP FOR TIME INTERVAL 12.53 TO 14.65 SECONDS (ABLATING NOSE)

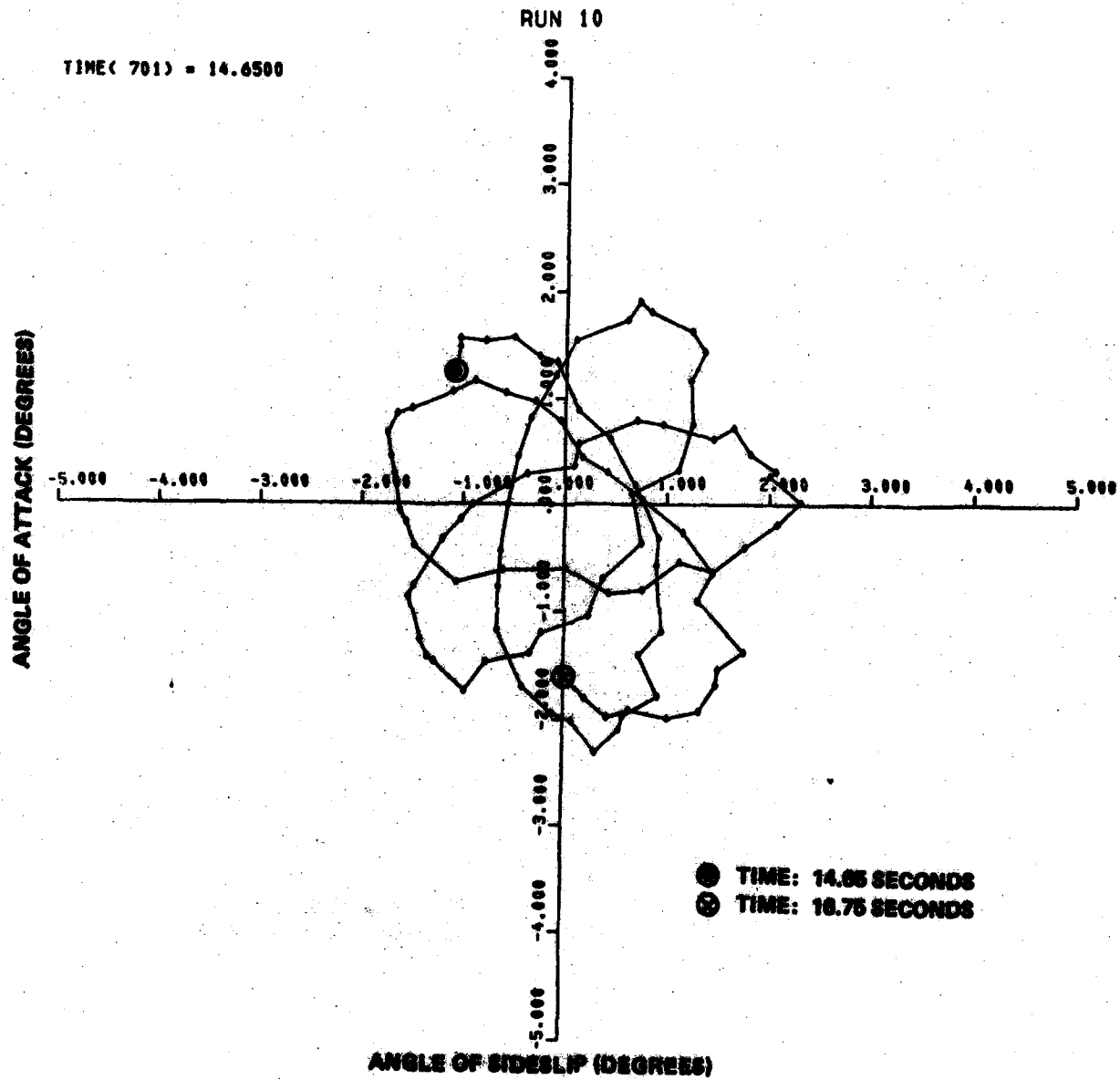


FIGURE 15 (h) ANGLE OF ATTACK VERSUS ANGLE OF SIDE SLIP FOR TIME INTERVAL 14.65 TO 16.75 SECONDS (ABLATING NOSE)

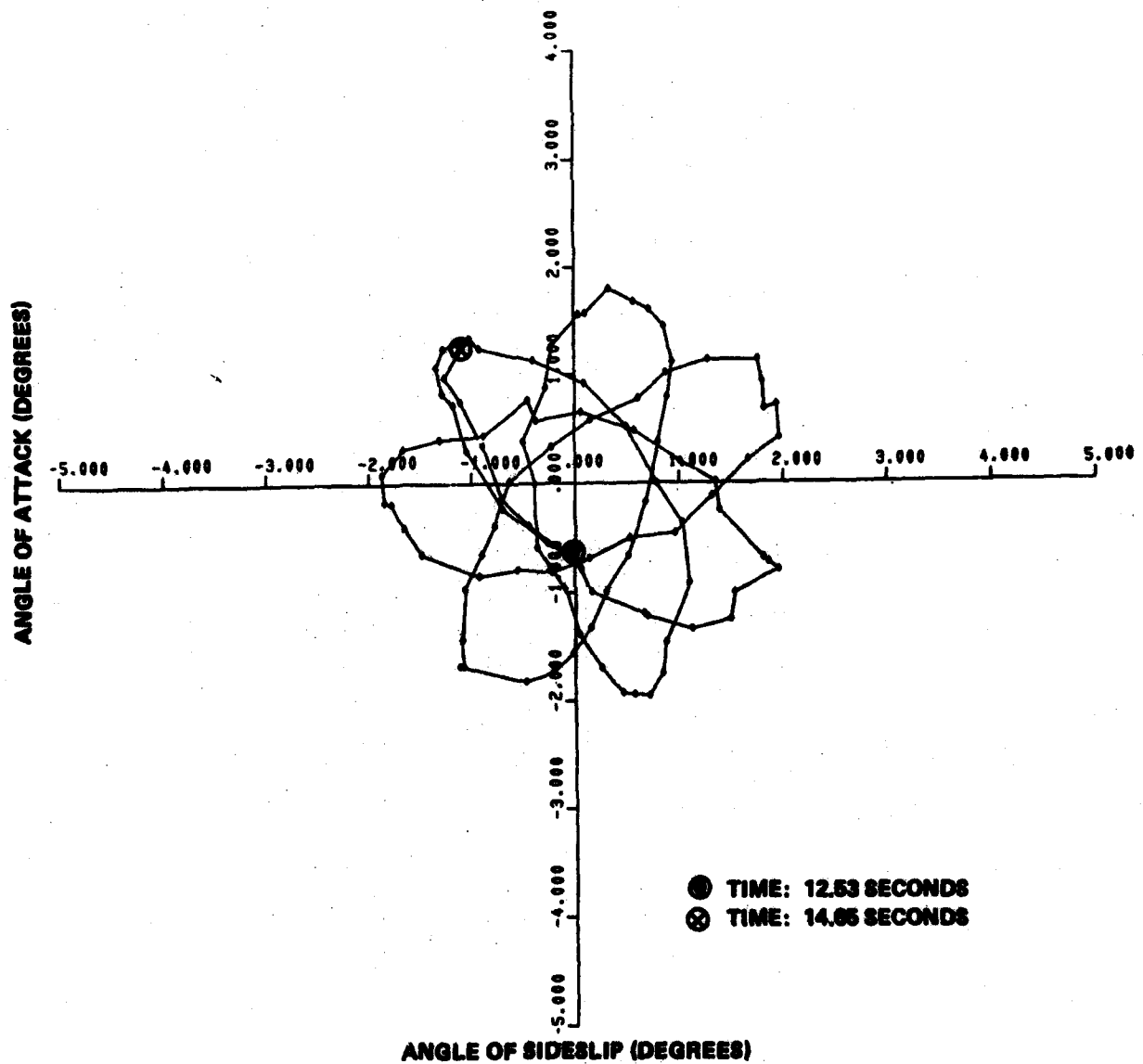


FIGURE 15 (g) ANGLE OF ATTACK VERSUS ANGLE OF SIDE SLIP FOR TIME INTERVAL 12.53 TO 14.65 SECONDS (ABLATING NOSE)

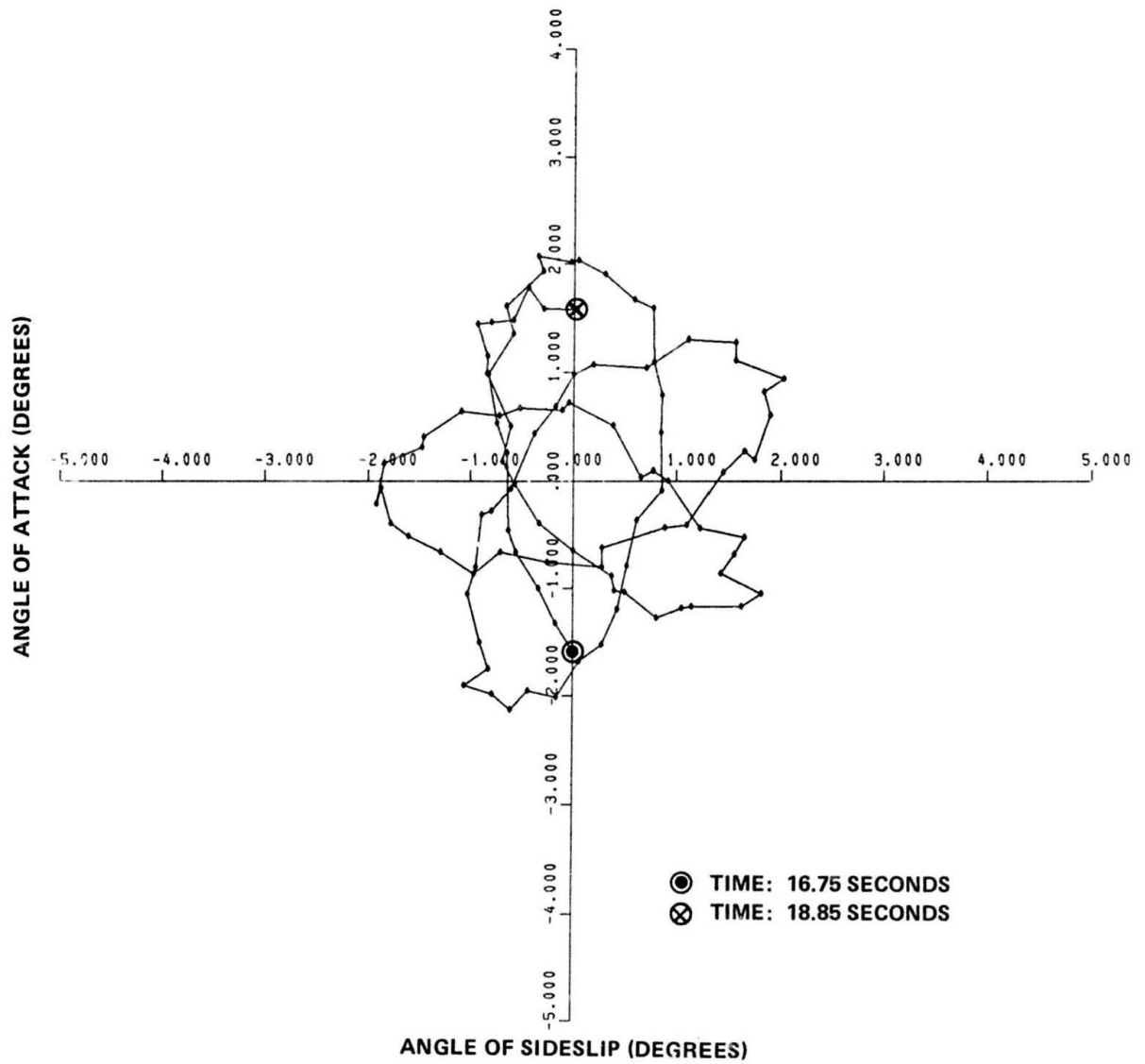


FIGURE 15 (i) ANGLE OF ATTACK VERSUS ANGLE OF SIDE SLIP FOR TIME INTERVAL 16.75 TO 18.85 SECONDS (ABLATING NOSE)

overlapping and non-overlapping records, is given in Table 7. The number of the first and last data point in each record is given in the first column. The corresponding values of time are given for the first and last point in the next column, followed by the average time for the record. The remaining columns give the static pitching moment derivative, $C_{m\alpha}$, the pitch-damping derivative, $C_{m\dot{q}}$, and the center of pressure aft of the c.g. in body lengths, X . It is felt that the spin rate was too low for the Magnus derivative to be assigned any reliability; hence, this derivative is not presented. The center of pressure is calculated from the pitching moment derivative, $C_{m\alpha}$, and an estimated value of the normal force derivative, as was done in equation (38). The difference between the center of pressure defined in equation (38) and in equation (39), below, is that the reference point now is taken as the center of gravity, 0.595 body lengths from the nose.

$$\bar{X} = \frac{C_{m\alpha} (d/l)}{C_{N\alpha}} \quad (39)$$

A value of $C_{N\alpha}$ of 1.35 / radian was taken from reliable sources. The conversion (d/l) is used to express \bar{X} in terms of body length where $C_{m\alpha}$ is based upon the body's maximum diameter as a reference.

It will be noted in Table 7. that the center of pressure at the beginning of ablation is about 0.0724 body lengths aft of the c.g. This value might be compared with the value of 0.0724 given in Table 6 for the sphere-cone test. The theoretical value for the non-ablating sphere cone is something like 0.053 body lengths, although the data in Table 7 is for an ablating model. An examination of the data in Table 7 shows that during ablation there is a steady forward motion of the center of pressure. At the beginning of ablation the center of pressure is about 0.074 body lengths aft of the c.g. After three seconds,

TABLE 7 SUMMARY OF REDUCED DATA FROM ABLATING
MODEL WITH SYMMETRICAL NOSE SUBSTRUCTURE

DATA POINT NUMBERS	TIME (SECONDS)	AV.-TIME (SECONDS)	$C_{m\alpha}$	C_{mq}	\bar{x} (% L)
1	0				
50	1.04	0.52	-.319	-7.5	0.0724
5	0.09				
55	1.15	0.62	-.321	-15.6	0.0728
10	0.19				
60	1.25	0.72	-.331	-19.9	0.0750
15	0.29				
65	1.34	0.81	-.336	-7.5	0.0760
20	0.40				
70	1.46	0.93	-.325	+6.3	0.0736
25	0.51				
75	1.56	1.035	-.308	+7.1	0.0699
50	1.04				
100	2.08	1.560	-.313	+23.4	0.0709
100	2.08				
150	3.14	2.61	-.323	-5.4	0.0732
150	3.14				
200	4.18	3.66	-.316	-3.6	0.0716
200	4.18				
250	5.22	4.70	-.315	11.0	0.0714
250	5.22				
300	6.26	5.74	-.314	8.0	0.0712
300	6.26				
350	7.30	6.78	-.313	-10.5	0.0708
350	7.30				
400	8.34	7.82	-.314	-7.6	0.0711
400	8.34				
450	9.41	8.87	-.314	+12.5	0.0713
450	9.41				
500	10.44	9.92	-.315	+0.3	0.0714

TABLE 7 (Cont.)

DATA POINT NUMBERS	TIME (SECONDS)	AV.-TIME (SECONDS)	$C_{m\alpha}$	C_{mq}	\bar{X} (% L)
500	10.44				
550	11.49	10.96	-.315	-11.5	0.0714
550	11.49				
600	12.50	11.99	-.315	+4.0	0.0713
600	12.50				
650	13.59	13.04	-.287	+7.1	0.0650
650	13.59				
700	14.63	14.11	-.241	+1.7	0.0545

the center of pressure is about 0.070 body lengths aft. As ablation continues and as the record nears the end the center of pressure moves to about 0.054 body lengths. The center of pressure measured in a wind tunnel on a constrained (static) model is close to the theoretical value of 0.053. It should be remembered that the model in the dynamic test is undergoing motion in three degrees of freedom and that the windward meridian is constantly changing in body coordinates.

As pointed out earlier, the damping in pitch derivative, $C_{m\dot{q}}$, may be given only a qualitative interpretation. It will be noted at the beginning of ablation that the angular record indicates dynamic stability. At about 1 second after the start of the record the motion has become dynamically unstable until something like 2 seconds has elapsed. After 2 seconds, the motion becomes stable again. This alternate dynamic stability and instability continues throughout the record.

Of minor interest perhaps is the fact that the plane of oscillation is rotating. (See Figures 15). If $\dot{\psi}$ is taken as the rotation rate of the plane of oscillation, then it may be shown that there is a relationship between $\dot{\psi}$ and the nutational and precessional frequencies, ω_1 and ω_2 , as:

$$\dot{\psi} = \omega_1 + \omega_2 \quad (40)$$

From equation (11c) it is immediately obvious that:

$$\dot{\psi} = \frac{I_x}{I_y} p \quad (41)$$

Therefore, the rate of rotation of the plane of oscillation is a simple function of the roll rate, p .

Of considerably more interest is the attitude of the nose toward the velocity vector which is assumed to be at the origin of the α - β petal graphs. It will be

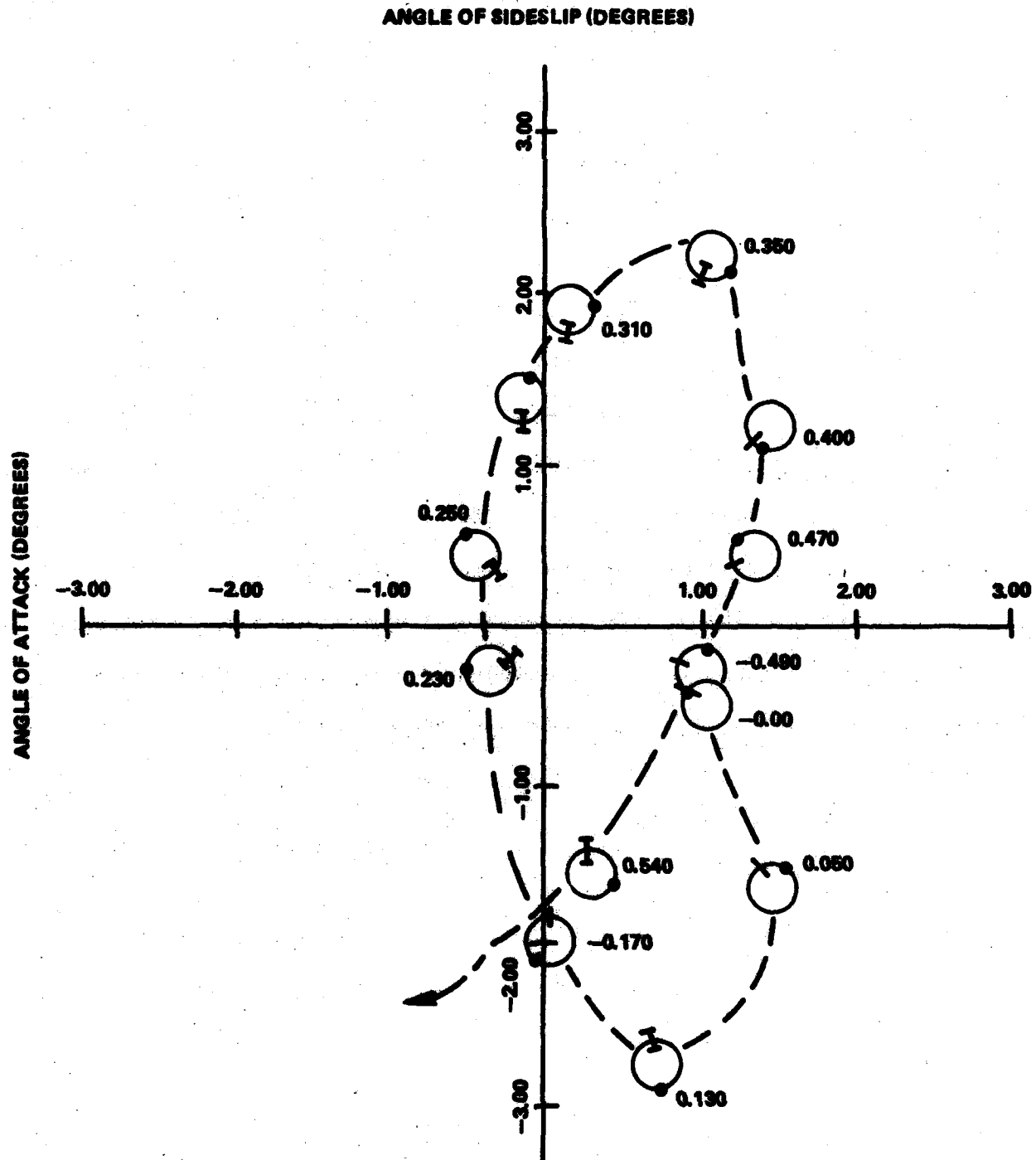


FIGURE 16 RELATIVE POSITION OF INITIAL WINDWARD MERIDIAN (•) AND INSTANTANEOUS WINDWARD MERIDIAN. (I) (ABLATING NOSE)

presumed that the meridional line on the body (or nose) that faces the origin or velocity vector will be the meridian of greatest heat transfer. At the nose this is the meridian of greatest ablation. Figure 16 is a rough attempt to track the windward meridian and a fixed point on the nose as the model undergoes about one oscillation. The fixed point on the nose that is being tracked is the original stagnation point at time $t = 0.00$ seconds. It will be noted that the model does not present the same meridian to the velocity vector as the model oscillates. One might expect fairly uniform ablation of the model, and hence no large trim angles, should develop throughout the ablation phase.

It would seem that since the ablation must perforce be confined to the nose, the forces (and their moments) resulting from the ablation are an entirely localized phenomenon. This may not be entirely accurate. It is true that there are local forces generated by the local ablative mass addition to the boundary layer. In addition however, we might expect the generation of forces considerably downstream due to cross-flow effects because the boundary layer has been thickened by the upstream ablation, i.e., there may be a transport effect associated with ablation. In addition there are the obvious effects due to changing body geometry resulting from the ablation. In the tests under discussion, with ablation confined to the nose, body shape changes are limited to the increase in nose bluntness and the development of a bi-conic shape (see Figures 12 and 13). Generally an increase in nose bluntness causes a decrease in the damping of angular motion. The effects caused by changes in nose geometry are usually small for the oscillation frequencies encountered and are therefore not the principal source of the ablation effect. Ablation induced loads arise "from a deflection of the free-stream flow caused by mass

injection into the boundary layer, either locally or by transport through the boundary layer from some other part of the body." ⁷

The question still remains as to whether or not ablation situated at the model's nose causes dynamic instability. The test results reported herein indicate that nose ablation does cause dynamic instability. These results agree with the conclusions of Ericsson and Reding (reference (5)):

"A slender conical reentry body may experience increased static stability but severely decreased dynamic stability at low angles of attack and low oscillation amplitudes when ablation is concentrated to the blunted nose and cone trailing edge."

Ericsson and Reding's paper (reference (5)) is an analytic exercise and is not substantiated by any experimental results. The authors admit in the conclusion to their paper: "... the analysis presented herein is highly speculative ...". Nevertheless to some extent the conclusions of this paper as indicated by the above quotation seem to be substantiated by the results of the ablating nose test reported herein.

In 1965 a series of experiments were carried out to examine the dynamic behavior of an ablating model undergoing single degree of freedom angular (pitch) motion. These experimental results were reported in what may be regarded as the seminal paper in the experimental investigations of the effects of surface ablation on the dynamics of a reentry body. ⁸ While this paper by Grimes is based upon wind tunnel dynamic tests, it should be appreciated that there are

⁷Ericsson, L.E., et al, "Ablation Effects on Vehicle Dynamics," Journal of Spacecraft, Vol. 3, No. 10, October 1966.

⁸Grimes, J.H., "Influence of Ablation on the Dynamics of Slender Reentry Configuration," Journal of Spacecraft, Vol 2, Jan/Feb 1965.

considerable differences between the model support system used in Grimes experiments and the three-degree-of-freedom gas bearing. The model in the tests reported in reference (8) cannot spin and its angular motion is restricted entirely to a plane. By way of contrast the model in the three-degree-of-freedom gas bearing is free, within an upper bound restriction on total angle of attack, to undergo simultaneous and mechanically-uncoupled yaw, pitch and roll motion. In other words a comparison is being made between experimental results from single degree of freedom and three degree of freedom model supports. Clearly there must be considerable differences between the ablation physics in both cases. In the three-degree-of-freedom support the presence of roll rate allows the region of ablation to alter its orientation with respect to the velocity vector independent of the angle of attack. Consequently neither Grimes nor Ericsson's paper for that matter can be entirely supportive of the gas bearing test presented in this report. Indeed there seems to be some conflict between Ericsson and Grimes as to the effect of ablation on dynamic stability. The following quotation is taken from Grimes' paper which conflicts with the experimental results of this report and the analytic results of Ericsson as indicated by the previously given quotation.

"Coating the entire model ... forward of the center of gravity, produced a dynamically stable configuration with C_{mq} values approaching those for flight test. Coating the rearward sections of a conic or cone-cylinder flair produces a dynamically unstable model."

In the above quotation the word "coating" refers to the application to the model of a low temperature ablator such as paradichlorobenzine $C_6H_4Cl_2$. Locating the "coating" is equivalent to setting the location of the model's surface ablation.

In brief the results of the three-degree-of-freedom support indicate that while the model is initially dynamically stable, the initiation of ablation causes dynamic instability which continues until the ablation ceases and the metallic bi-conic nose is revealed.

The following is a partial listing of the conclusions that might be drawn from these ablation tests:

(a) The static center of pressure is at about 0.073 body lengths aft of the center of gravity (0.595 body lengths aft of the nose) at the beginning of ablation. This value is essentially the same as that measured for the steel nose (non-ablating) sphere cone model.

(b) The static center of pressure moves forward during ablation to a value of about 0.054 body lengths.

(c) Agreement seems to be acceptable with results from supported testing where the center of pressure is about 0.053 body lengths. It must be remembered that dynamic testing about a single axis cannot provide the normal force derivative, C_{N_α} , and hence a final evaluation of the center of pressure must rely on an external source of C_{N_α} .

(d) Dynamic measurements indicate regions of dynamic stability and instability. No convincing argument is available at this time to entirely explain this observation.

4.3 POST-ABLATION WIND TUNNEL TEST - ABLATING NOSE SUBSTRUCTURE

(SYMMETRICAL). In the previous section (Section 4.2)) the ablating nose tests were discussed. It should be recalled and emphasized that ablation was confined to the nose by replacing the steel nose by a low temperature ablator. The initial shape of this ablating nose was a hemi-sphere of 0.223 bluntness (see Figure 7). The substructure of this nose is the contour illustrated in Figure 12. When the ablation process is completed this contour is

revealed. The "post-ablation" shape was developed from photographic records of preserved contours from earlier static ablation tests. It may be seen in the ablation sequences of Figures 13 that the contour does ablate to something like this shape, so that Figure 12 depicts the asymptotic contour of the ablation process. It is of course necessary to preserve this ablated shape as a steel substructure for post-ablation dynamic testing - the low temperature ablator would continue to change shape under ambient conditions.

It was assumed that 60 seconds after initiation of the ablation run, that ablation was complete and the steel substructure was completely revealed. The kicking jet was then initiated to supply angular displacement to the model. This would then begin a new run designated as the post ablation run with symmetrical steel sub-structure. Since it was not possible to be completely certain that ablation has removed all of the low temperature ablator, it was decided to reduce the 750 data point-long run in overlapping records of 150 data points each. The result of this exercise is presented in Table 8. It will be noted that the center of pressure is nearly exactly that measured at the end of the ablating run (see Table 7). The α - β history of this post-ablation run is given in Figures 17; the α - β petal plots are presented in Figures 18. It will be noted that these petal plots for the post-ablation run are nearly circular as compared with the more leaf-like shape observed during the ablation run (see Figures 15) as the sphere-cone runs (see Figures 10). It is possible to show that the character of the motion is merely dependent upon initial conditions in α and β . First by way of definition,

TABLE 8 SUMMARY OF REDUCED DATA FROM POST-ABLATION MODEL
WITH SYMMETRICAL NOSE SUBSTRUCTURE

DATA POINT NUMBERS	TIME (SECONDS)	AV.-TIME (SECONDS)	$C_{m\alpha}$	C_{mq}	\bar{X}
1	0				
150	3.11	1.55	-.231	-2.17	0.0524
50	1.03				
200	4.15	2.59	-.233	-6.19	0.0528
100	2.07				
250	5.19	3.63	-.263	+2.30	0.0596
150	3.11				
300	6.23	4.67	-.236	-3.40	0.0535
200	4.15				
350	7.27	5.71	-.237	2.81	0.0536
250	5.19				
400	8.31	6.75	-.239	6.79	0.0542
300	6.23				
450	9.35	7.79	-.240	3.48	0.0544
400	8.31				
550	11.43	9.87	-.239	0.69	0.0543
450	9.35				
600	12.47	10.91	-.241	1.52	0.0547
500	10.39				
750	15.59	12.99	-.243	-.06	0.055

ANGLE OF ATTACK —————
 ANGLE OF SIDESLIP - - - - -
 TIME: 0 TO 5 SECONDS

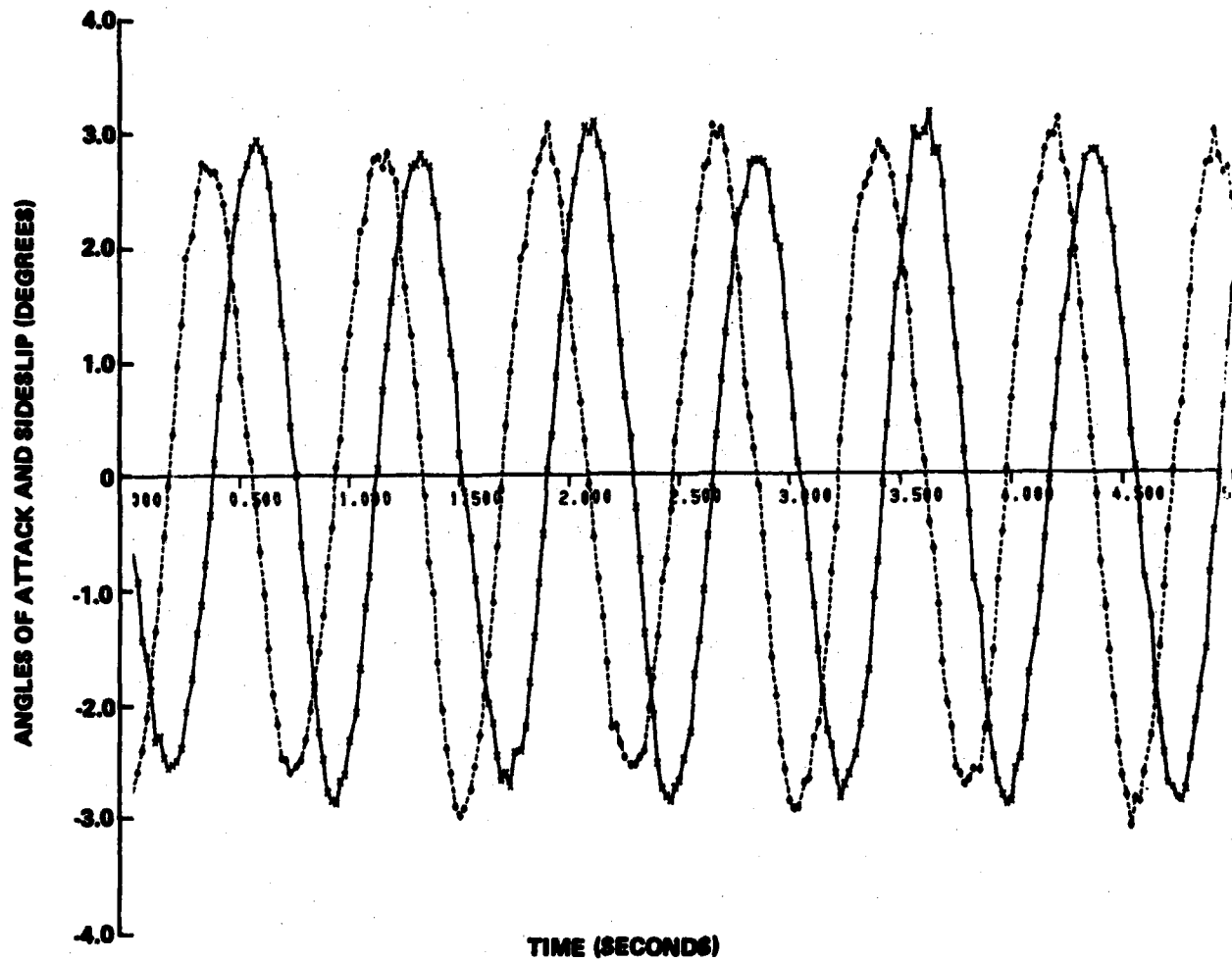


FIGURE 17 (a) ANGLES OF ATTACK AND SIDESLIP VERSUS TIME
 (ABLATING NOSE SUBSTRUCTURE - NO TILT)

ANGLE OF ATTACK —————
 ANGLE OF SIDESLIP - - - - -
 TIME: 5 TO 10 SECONDS

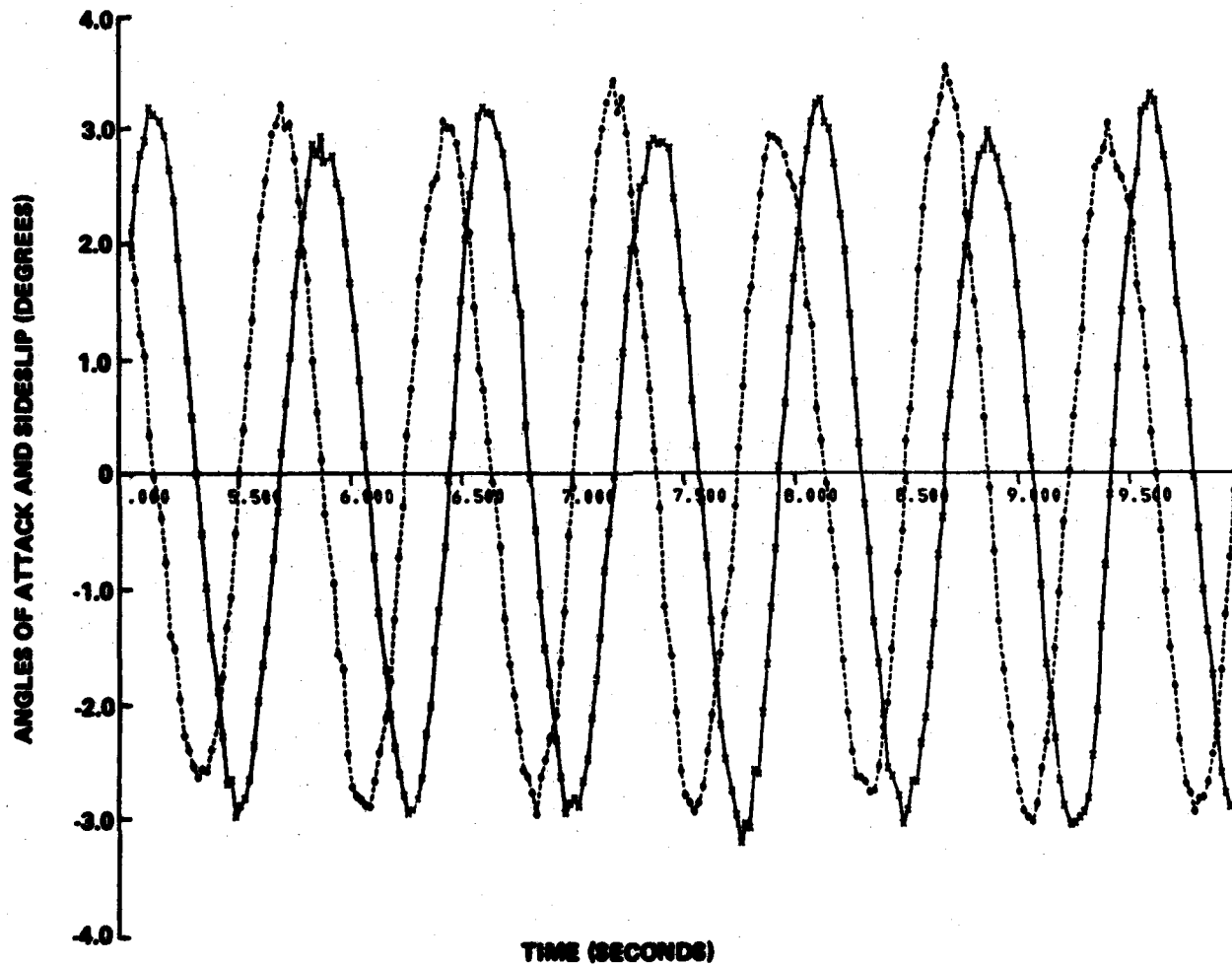


FIGURE 17 (b) ANGLES OF ATTACK AND SIDESLIP VERSUS TIME
 (ABLATING NOSE SUBSTRUCTURE - NO TILT)

ANGLE OF ATTACK —————
 ANGLE OF SIDESLIP - - - - -
 TIME: 10 TO 15 SECONDS

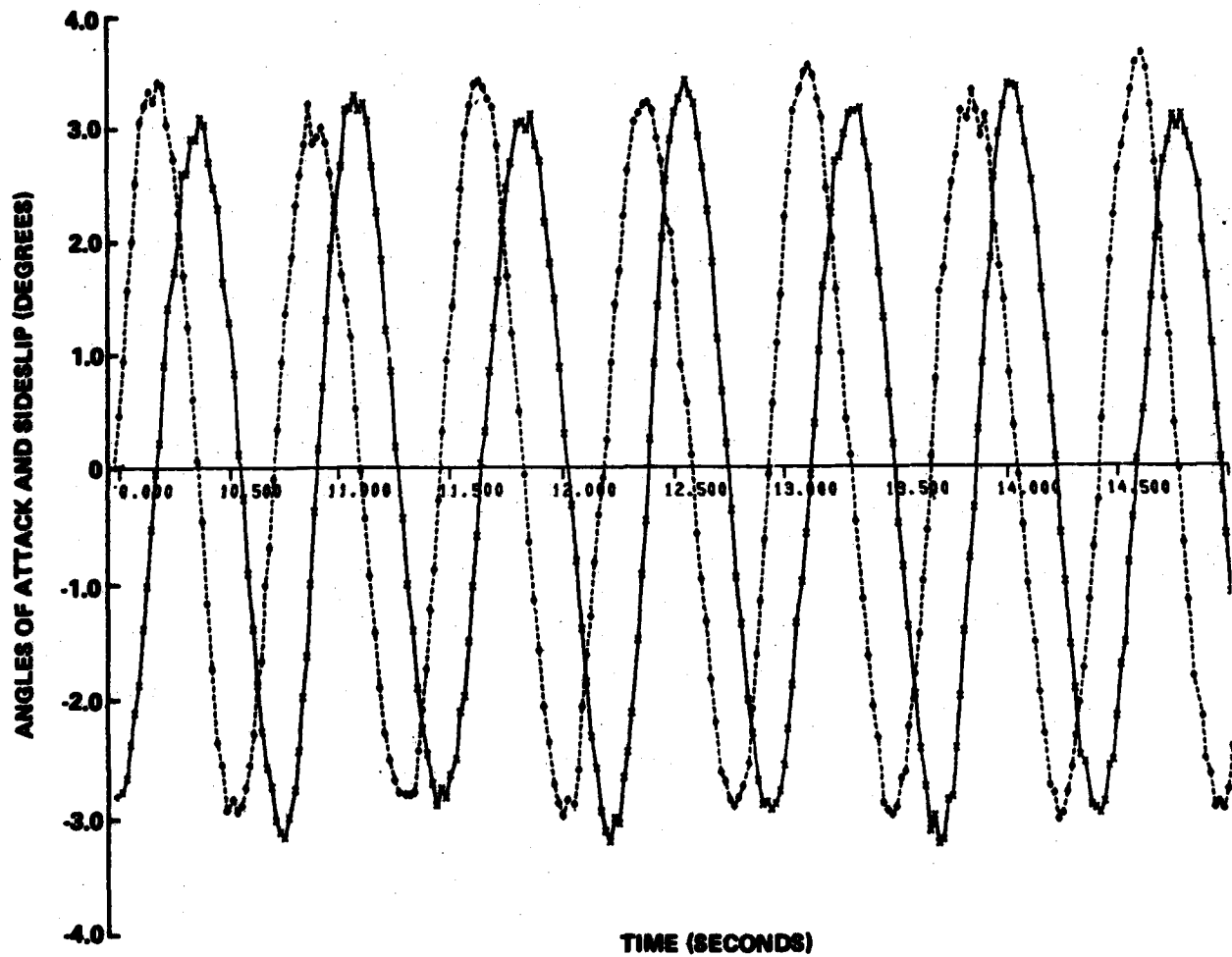


FIGURE 17 (c) ANGLES OF ATTACK AND SIDESLIP VERSUS TIME
 (ABLATING NOSE SUBSTRUCTURE - NO TILT)

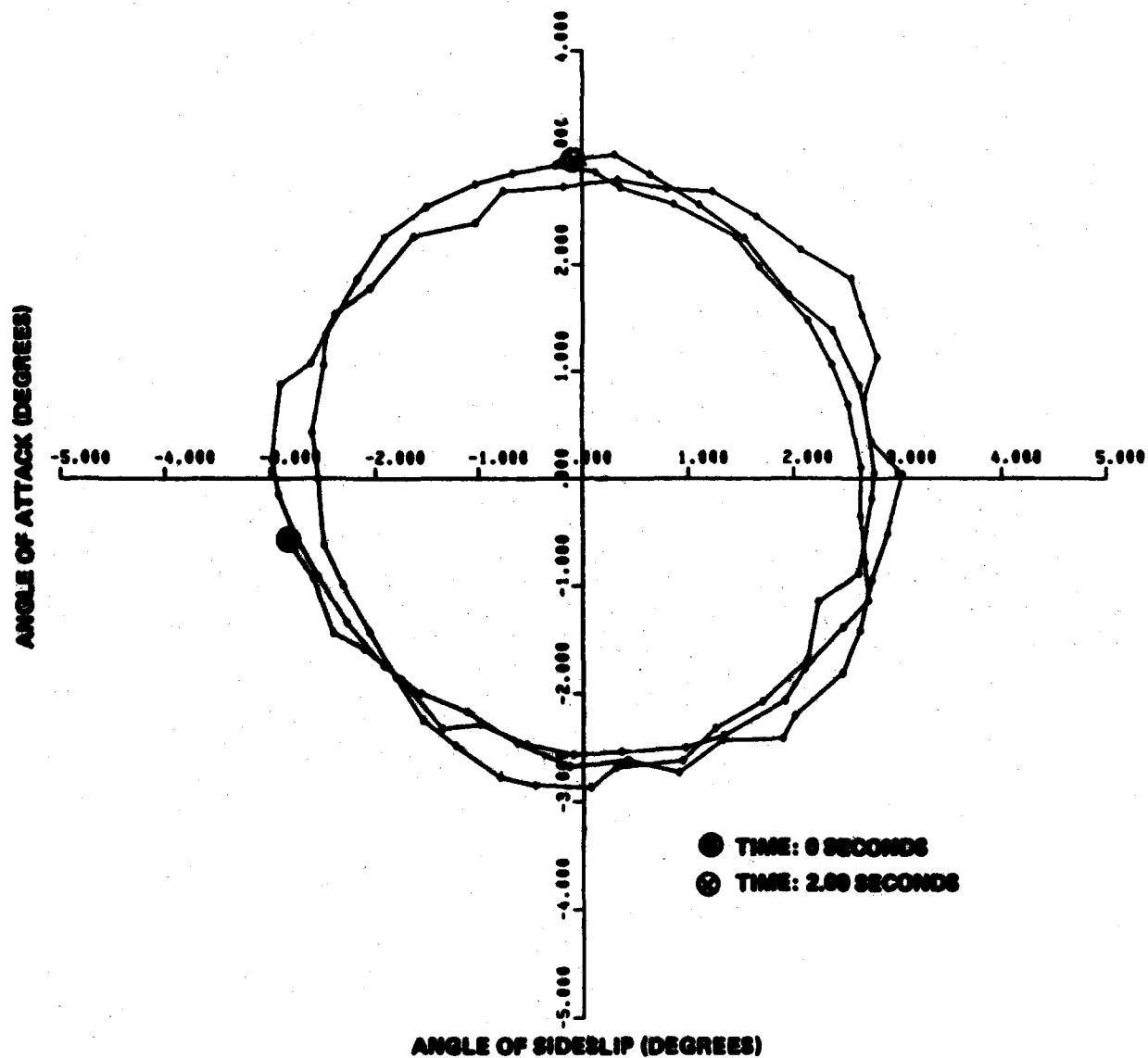


FIGURE 10 (a) ANGLE OF ATTACK VERSUS ANGLE OF SIDE SLIP FOR TIME INTERVAL 0 TO 2.00 SECONDS
(ABLATING NOSE SUBSTRUCTURE - NO TILT)

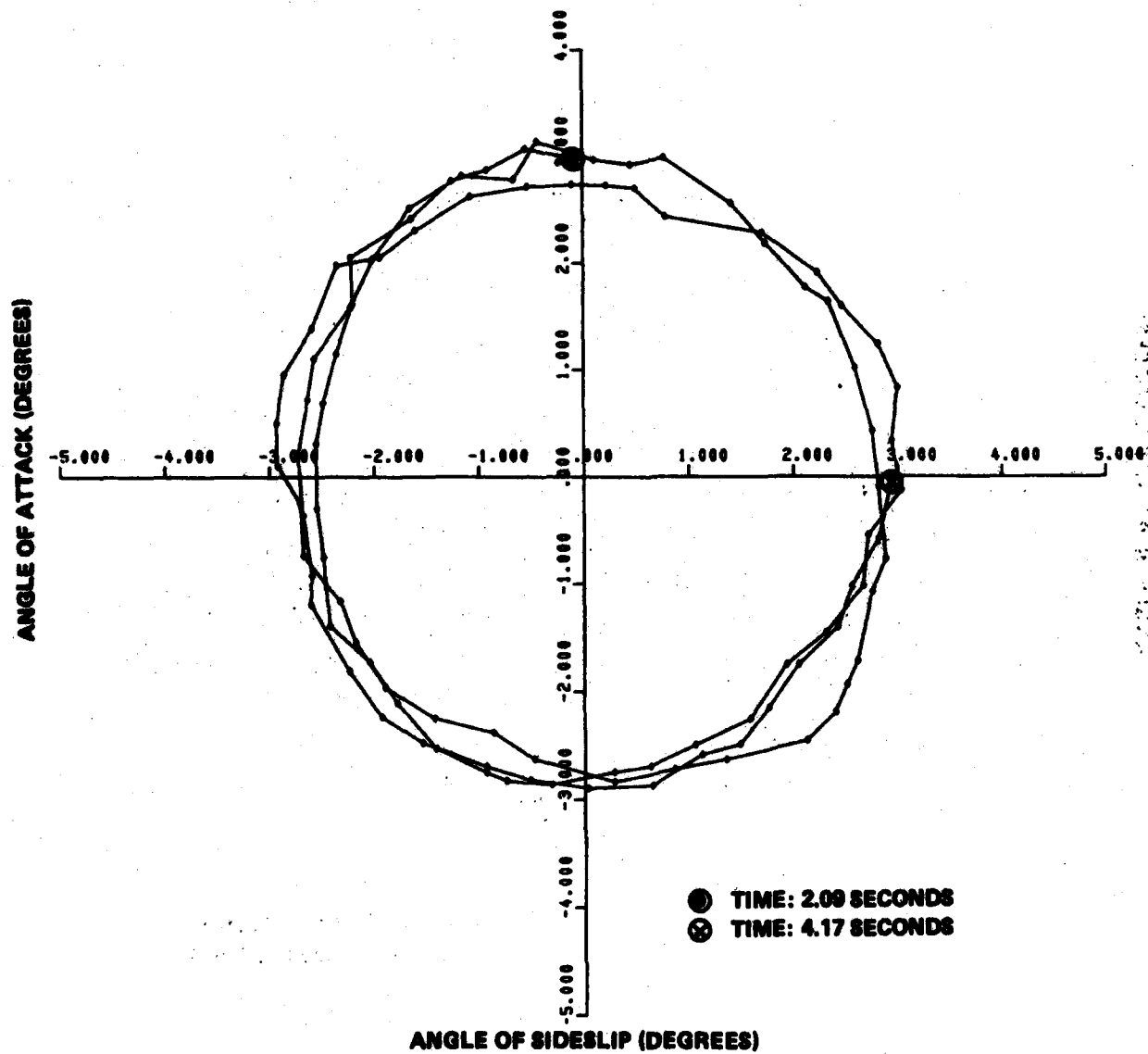


FIGURE 18 (b) ANGLE OF ATTACK VERSUS ANGLE OF SIDE SLIP FOR TIME INTERVAL 2.09 TO 4.17 SECONDS
(ABLATING NOSE SUBSTRUCTURE - NO TILT)

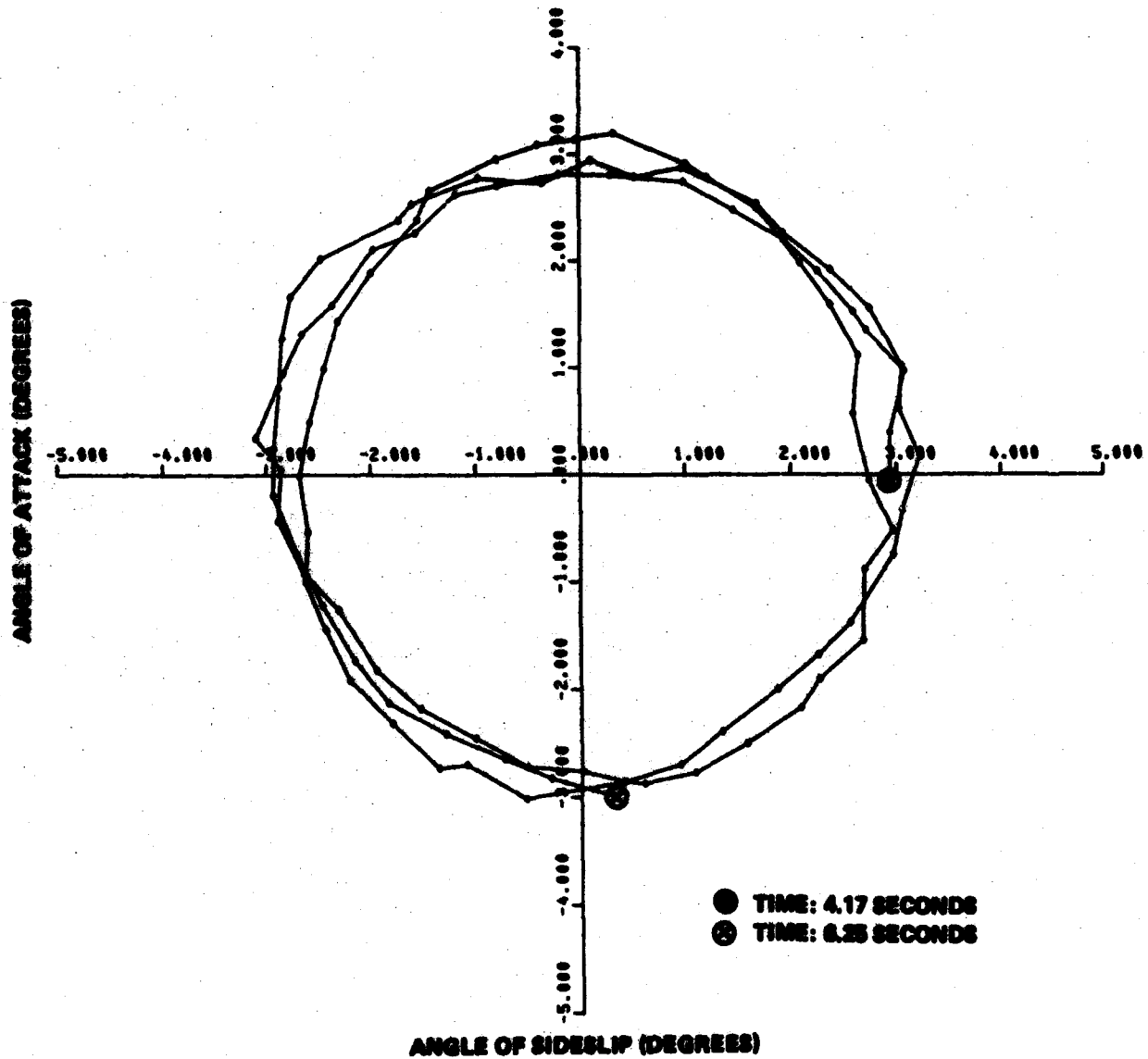


FIGURE 10 (a) ANGLE OF ATTACK VERSUS ANGLE OF SIDE SLIP FOR TIME INTERVAL 4.17 TO 6.25 SECONDS (ABLATING NOSE SUBSTRUCTURE - NO TILT)

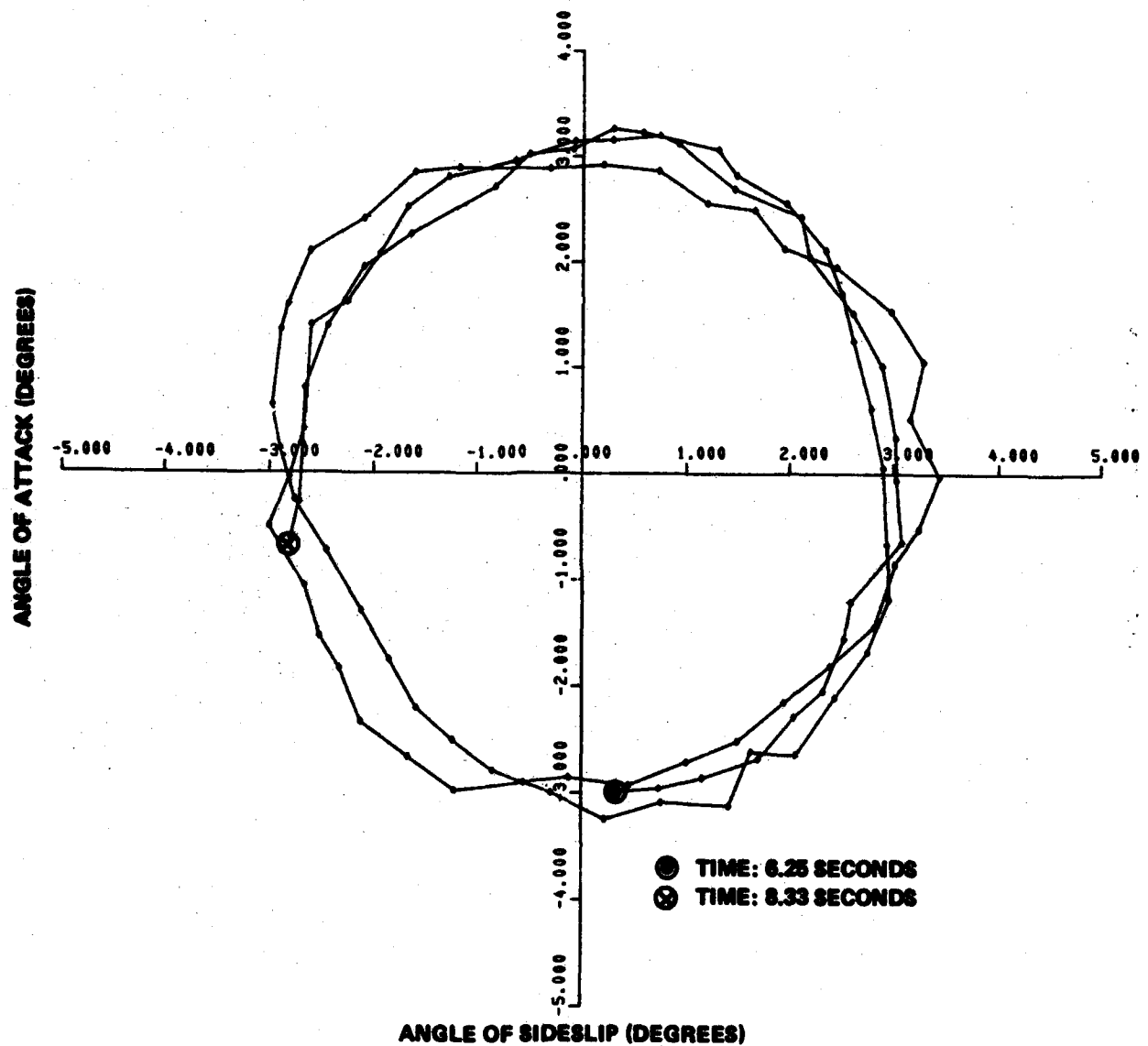


FIGURE 18 (d) ANGLE OF ATTACK VERSUS ANGLE OF SIDE SLIP FOR TIME INTERVAL 6.25 TO 8.33 SECONDS (ABLATING NOSE SUBSTRUCTURE - NO TILT)

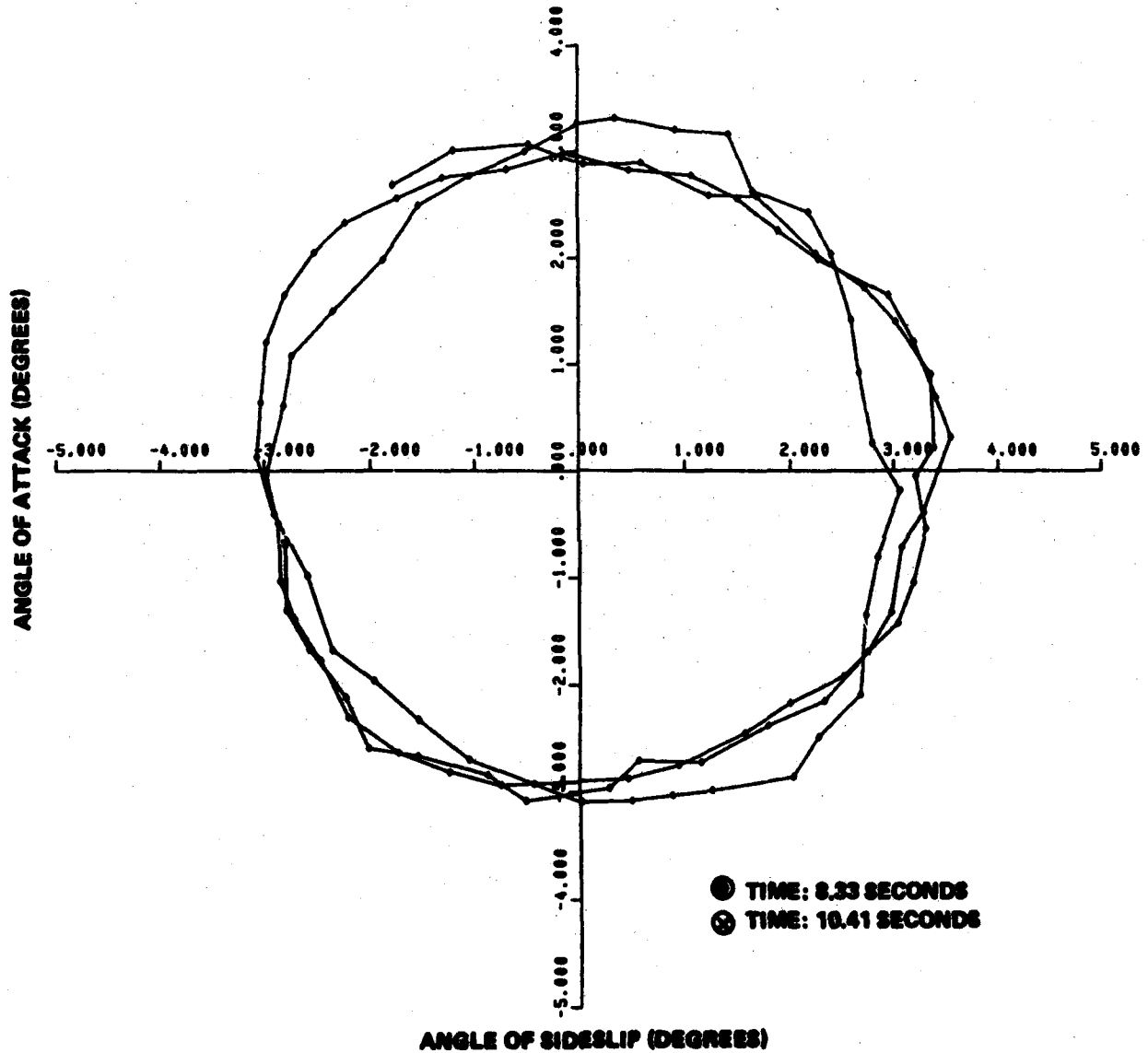


FIGURE 18 (a) ANGLE OF ATTACK VERSUS ANGLE OF SIDE SLIP FOR TIME INTERVAL 8.33 TO 10.41 SECONDS
(ABLATING NOSE SUBSTRUCTURE - NO TILT)

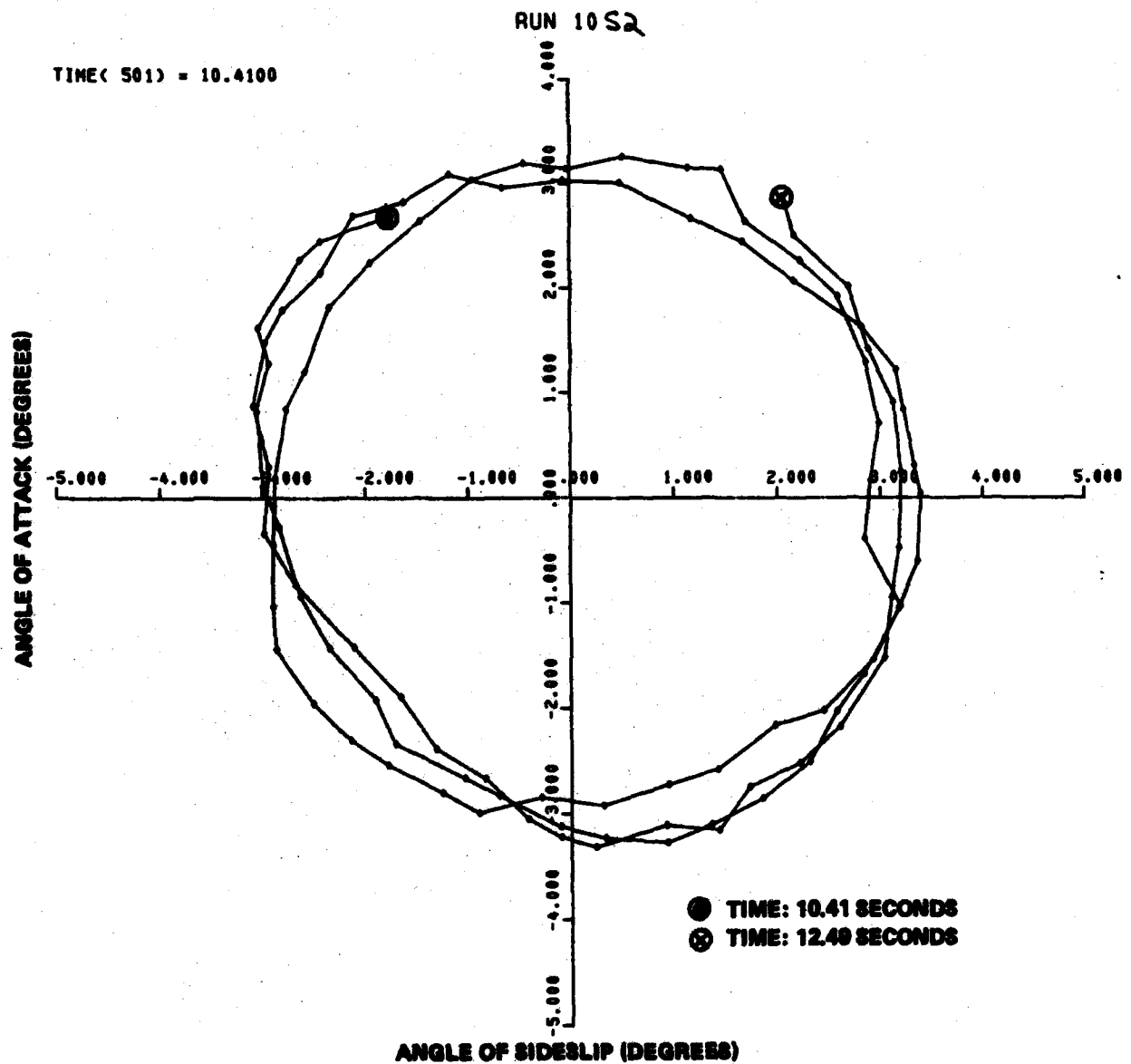


FIGURE 18 (7) ANGLE OF ATTACK VERSUS ANGLE OF SIDE SLIP FOR TIME INTERVAL 10.41 TO 12.49 SECONDS
(ABLATING NOSE SUBSTRUCTURE - NO TILT)

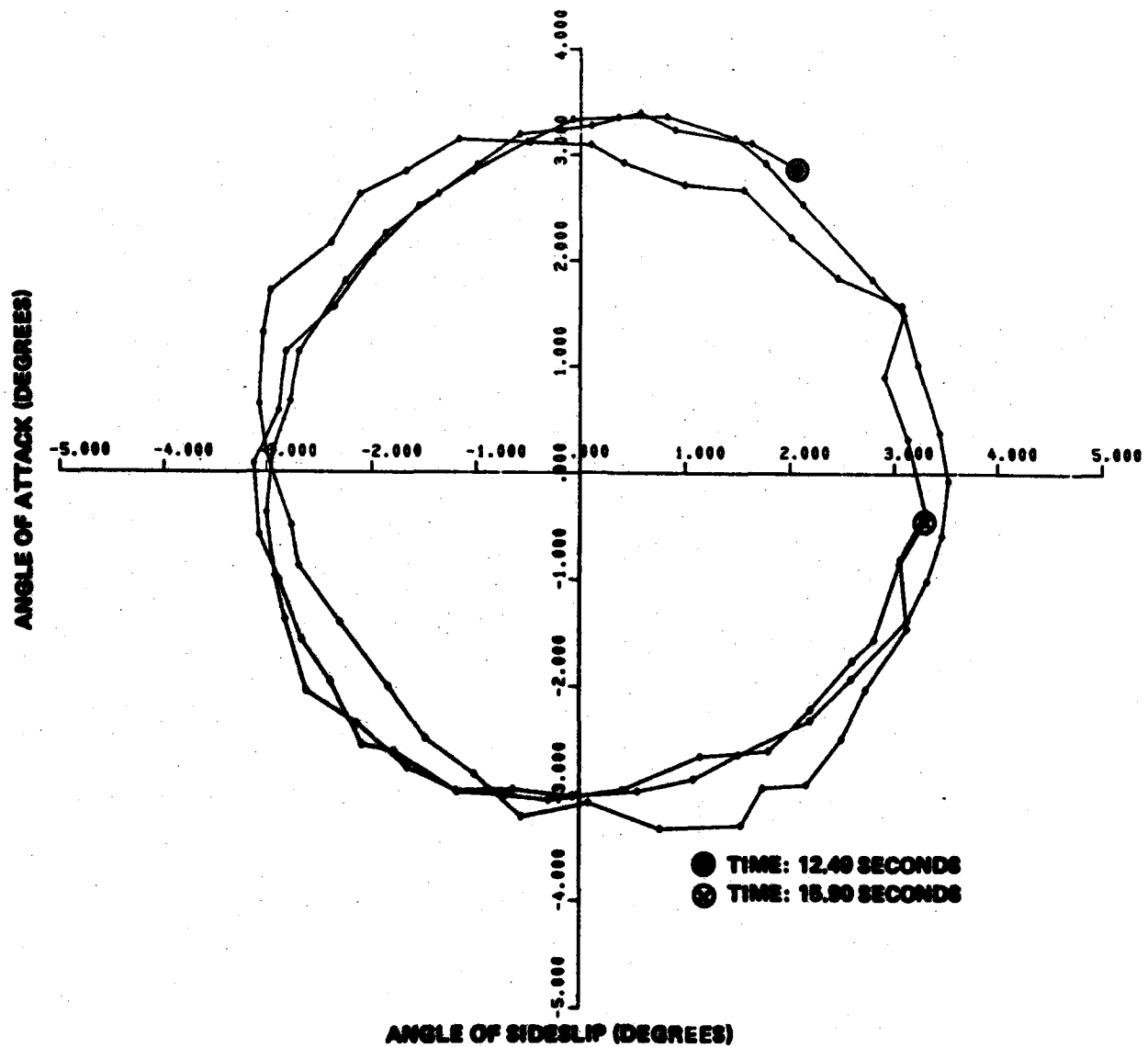


FIGURE 18 (a) ANGLE OF ATTACK VERSUS ANGLE OF SIDE SLIP FOR TIME INTERVAL 12.40 TO 15.90 SECONDS (ABLATING NOSE SUBSTRUCTURE - NO TILT)

$$\alpha /_{t=0} = \alpha_0$$

$$\frac{d\alpha}{dt}/_{t=0} = \dot{\alpha}_0$$

$$\beta /_{t=0} = \beta_0$$

$$\frac{d\beta}{dt}/_{t=0} = \dot{\beta}_0$$

(42)

In equations (6) it was shown that the motion is initially established by the six constants $A_1, B_1, A_2, B_2, A_3, B_3$. One of the constants, A_1 , was given in equations (6) as a generic form. Most reentry vehicles, as well as other statically stable vehicles, have the characteristic that the damping exponents λ_1 and λ_2 are small in comparison to the circular frequencies, ω_1 and ω_2 , as

$$\lambda_1 \ll \omega_1$$

$$\lambda_2 \ll \omega_2$$

Neglecting λ_1 and λ_2 where they appear in the expressions for the above six constants results in an error that is typically about 2 percent.* With the assumption noted the six constants

* A more exact estimate of this error is

$$\frac{\sqrt{2} \lambda_1}{\omega_1} \times 100 \qquad \frac{\sqrt{2} \lambda_2}{\omega_2} \times 100$$

which for the wind tunnel runs under consideration are about 2%.

may be written as,

$$\begin{aligned}
 A_1 &= - \left[\frac{\dot{\beta}_0 + \omega_2 \alpha_0 + (p - \omega_2) A_3}{\omega_1 - \omega_2} \right] \approx - \left[\frac{\dot{\beta}_0 + \omega_2 \alpha_0}{\omega_1 - \omega_2} \right] \\
 B_1 &= \left[\frac{\dot{\alpha}_0 - \omega_2 \beta_0}{\omega_1 - \omega_2} \right] \\
 A_2 &= - \left[\frac{\dot{\beta}_0 + \omega_1 \alpha_0 + (p - \omega_1) A_3}{\omega_2 - \omega_1} \right] \approx - \left[\frac{\dot{\beta}_0 + \omega_1 \alpha_0}{\omega_2 - \omega_1} \right] \\
 B_2 &= \left[\frac{\dot{\alpha}_0 - \omega_1 \beta_0}{\omega_2 - \omega_1} \right] \\
 A_3 &= \frac{M_\delta \delta}{I_y} \left[\frac{1}{\omega_2 (p - \omega_1) + p(\omega_1 - p)} \right], \quad p \neq \omega_1
 \end{aligned} \tag{43}$$

$$B_3 \approx 0, \quad p \neq \omega_1$$

where the simplification at the far right assumes no body-fixed asymmetry, i.e., $A_3 \sim \delta = 0$. If A_1 and B_1 are regarded as the components of a polar vector, K_1 in the β (horizontal) and α (vertical) direction, respectively, then,

$$K_1|_{t=0} = K_{10} = \sqrt{A_1^2 + B_1^2} \tag{44a}$$

A similar relationship may be written for A_2 and B_2 as,

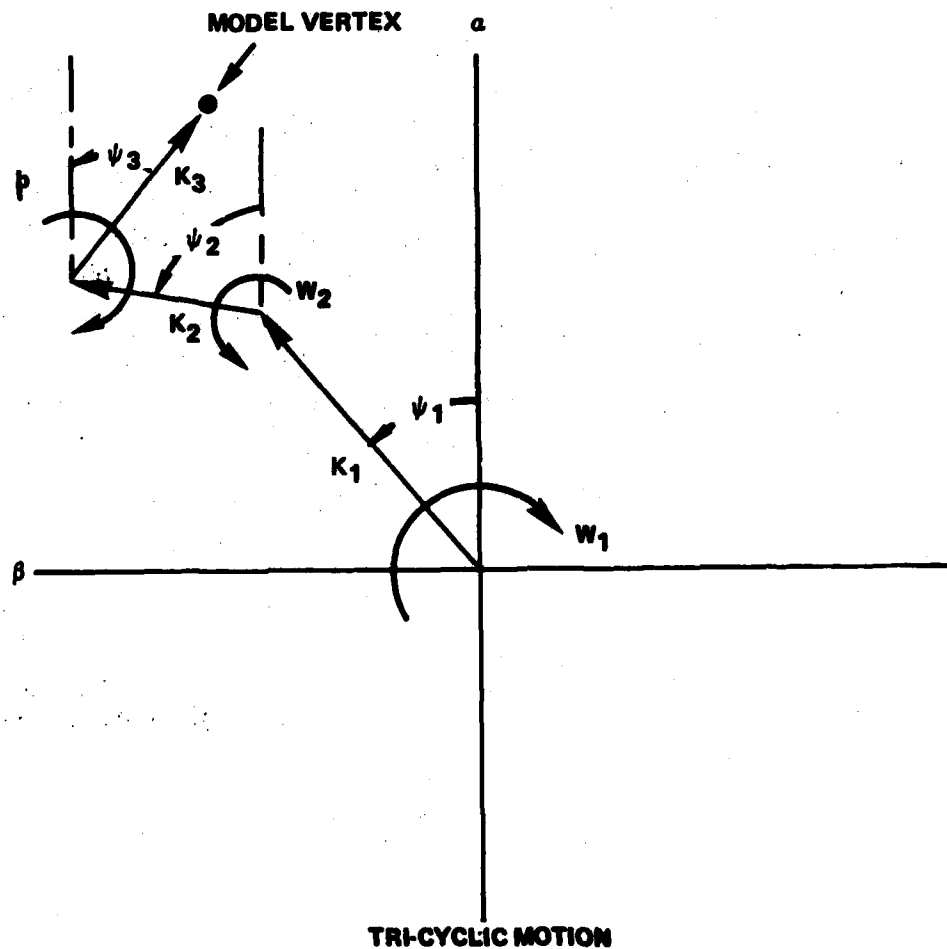
$$K_2|_{t=0} = K_{20} = \sqrt{A_2^2 + B_2^2} \tag{44b}$$

and for A_3 and B_3 as,

$$K_3 \text{ at } t=0 = K_{30} = \sqrt{A_3^2 + B_3^2} \quad (44c)$$

It can easily be shown from equations (6) and (10) the K_1 rotates with a rate ω_1 radians/second in the same direction as the roll rate, p and that K_2 rotates at a rate ω_2 in a direction opposite to the spin rate K_3 , which accounts for a body-fixed asymmetry rotates at the spin rate, p .

The geometry of this "tri-cyclic motion" is given in the sketch below.



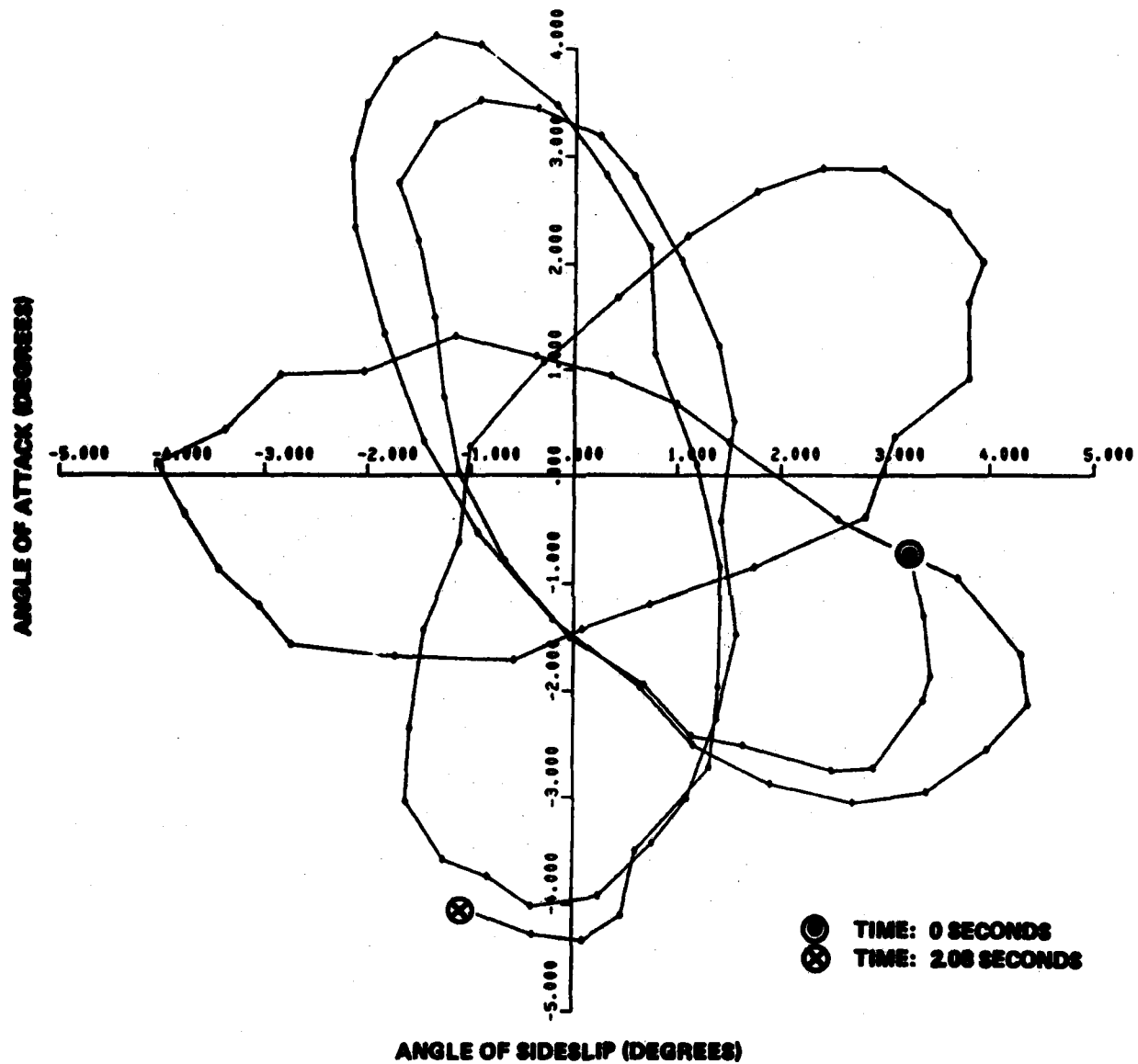


FIGURE 19 (a) ANGLE OF ATTACK VERSUS ANGLE OF SIDESLIP FOR TIME INTERVAL 0 TO 2.08 SECONDS (ABLATING NOSE SUBSTRUCTURE - 3 DEG TILT)

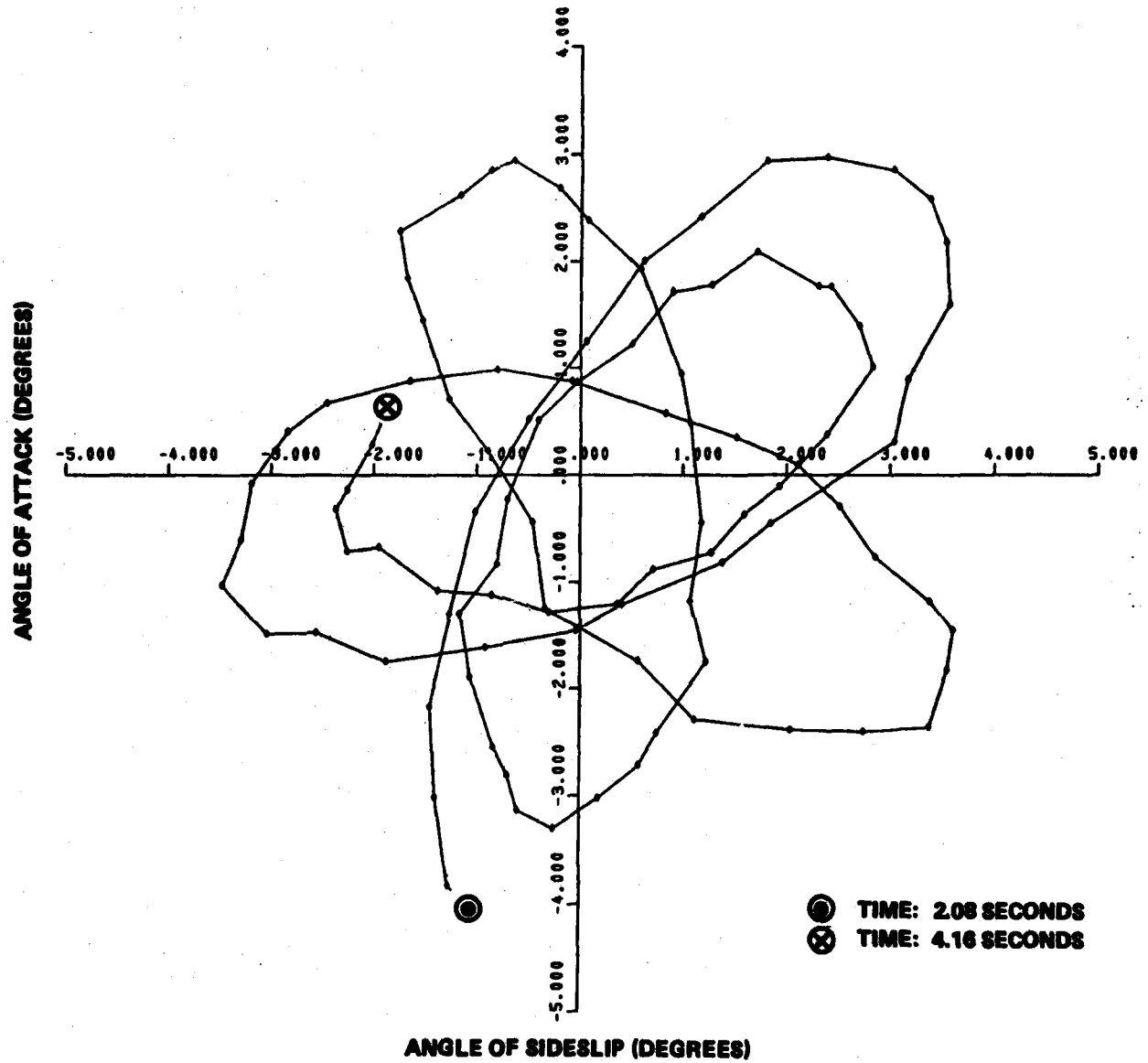


FIGURE 19 (b) ANGLE OF ATTACK VERSUS ANGLE OF SIDESLIP FOR TIME INTERVAL 2.08 TO 4.16 SECONDS (ABLATING NOSE SUBSTRUCTURE - 3 DEG TILT)

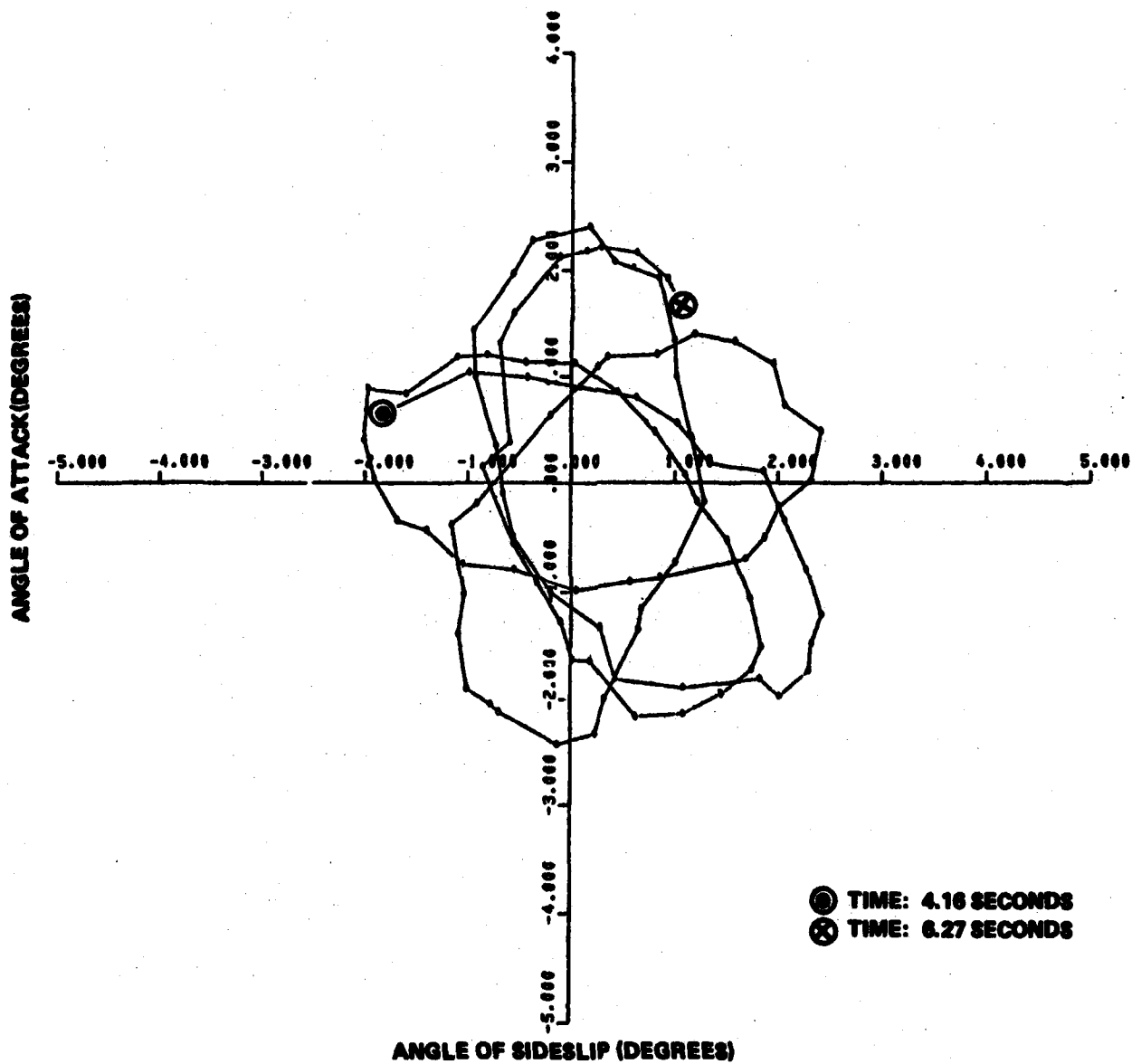


FIGURE 19 (a) ANGLE OF ATTACK VERSUS ANGLE OF SIDESLIP FOR TIME INTERVAL 4.16 TO 6.27 SECONDS (ABLATING NOSE SUBSTRUCTURE - 3 DEG TILT)

In examining the motion of the model in Figures 18, the observed circular motion is due to a vanishing of the K_2 arm. Now, it will be recalled that the air-jet acts only to cause an angular displacement in the vertical plane, i.e., to set α_0 (and perhaps $\dot{\alpha}_0$). However, since the post-ablation run was initiated with some residual motion from the preceding ablating run, it is likely that β_0 and $\dot{\beta}_0$ were not zero at initiation of the kicking jet.

A fortuitous set of circumstances could well result in the minimization or elimination of the K_2 arm by reducing or eliminating A_2 and/or B_2 . This could happen if the numerators in the expressions for A_2 and B_2 in equations (43) are small. For example, remembering that ω_2 is always negative (p, spin rate, and ω_1 nutation rate taken as positive), if $\dot{\beta}_0$ is negative and α_0 is positive, then if

$$\dot{\beta}_0 = -\omega_1 \alpha_0 \quad (45)$$

the numerator of A_2 vanishes. The operation of the kicking jet also occurs when both $\dot{\alpha}_0$ and β_0 are small, reducing the magnitude of B_2 (as well as A_2).

The point of this discussion is that the presence of circular motion does not indicate any unusual dynamic effects. A comparison of the center of pressure values between the ablation test (Table 7) and the post-ablation test (Table 8) indicates coincidence in this parameter.

4.4 POST-ABLATION WIND TUNNEL - ABLATING NOSE SUBSTRUCTURE (ASYMMETRICAL).

The test discussed in this section, like that of the previous section, is also a test of the model with the ablating nose substructure in place (see Figure 12). However, unlike the previous test the axis of symmetry of this nose is tilted 3 degrees with respect to the center line of the conical after body. This nose tilt then introduces an asymmetry into the configuration. The results of this test are given below in Table 9. The α - β petal plats are given in Figure 19.

TABLE 9
NON-DIMENSIONAL AERODYNAMIC COEFFICIENTS AND SPIN RATE FOR MODEL WITH
ASYMMETRICAL NOSE SUBSTRUCTURE

STATIC C _{NA}	DYNAMIC C _{NQ}	MAGNUS C _{MPA}	SPIN P (RAD/SEC)	C.P. X (BO=Y-LENGTH)
-0.25757	-1.98461	-0.939371	-33.6564	5.83634E-2

It will be noted in Table 9 that the center of pressure is comparable to that given for the symmetrical ablating nose substructure (Table 8). Figures 19 do not indicate the circular motion observed for the symmetrical nose. The asymmetric-nose tests were performed as an initial inspection in the wind tunnel and did not follow an ablating test. Consequently β_0 and $\dot{\beta}_0$ were negligibly small so both the K_1 and K_2 modes were excited.

5.0 CONCLUSIONS

These tests led to some interesting results. It was shown that the non-ablating sphere-cone model had a center-of-pressure that was 0.669 body lengths aft of the center of gravity. Comparisons were made favorably with earlier static wind tunnel data. The ablating nose model had a center of pressure almost exactly at the same point as the non-ablating model at the onset of ablation. During ablation there was a steady forward motion of the center of pressure. Dynamic measurements during the ablation indicate that there are regions of dynamic stability and instability.

Completion of this test program has been more laborious than anticipated due to the failure of the fiber optic readout system to function satisfactorily. Nevertheless, it has been demonstrated that the three-degree-of-freedom model support can be used to make pitching moment measurements on ablating and non-ablating models in the Naval Surface Weapons Center's Hypersonic Wind Tunnel.

6.0 BIBLIOGRAPHY

- Ericsson, J.E., and Reding, J. P., "Ablation Effects on Vehicle Dynamics," Journal of Spacecraft, Vol. 3, No. 10, October 1966.
- Grimes, J.H., "Influence of Ablation on the Dynamics of Slender Re-entry Configurations," Journal of Spacecraft, Vol. 2, No. 1, Jan/Feb 1965.
- Jobe, M.D., et al, "Bi-Modal Flow Field Feasibility Demonstration in the NSWC/WO Hypersonic Tunnel (WTR 1319)," NSWC MP 79-217, May 1979.
- Murphy, C. H., "Free Flight Motion of Symmetric Missiles," Report No. 1216, Ballistic Research Laboratories, July 1963.
- Nicolaides, J.D., "On the Free Flight Motion of Missiles Having Slight Configurational Asymmetries," Report No. 858, Ballistic Research Laboratories, June 1953.
- Nielsen, Kaj. L., Methods in Numerical Analysis, 2nd Edition (New York: The Macmillan Company, 1964), pp. 309-313.
- Ragsdale, W.C., et al, "Mach 10 IAP Static Force Test Program in the NSWC/WOL Hypersonic Tunnel (WTR 1296)," NSWC/WOL MP 77-33, September 1977.
- Vaughn, H.R., "A Detailed Development of Tricyclic Theory," Report No. SC-M-67-2933, Sandia Laboratories, February 1968.

DISTRIBUTION

	<u>Copies</u>		<u>Copies</u>
Commander		Director, U.S. Naval Research	
Naval Sea Systems Command,		Laboratory	
Headquarters		Attn: Library	1
Attn: Chief Tech. Analyst		Code 6503	1
SEA 05121	1	Washington, DC 20390	
SEA 033	1		
SEA 031	1	NASA	
SEA 09G32	1	Langley Research Center	
SEA 035	1	Attn: MS/185 Technical Library	1
Department of the Navy		Aero & Space Mech. Div.	1
Washington, DC 20360		Hampton, VA 23665	
Commander, Naval Air Systems		NASA	
Command, Headquarters		Lewis Research Center	
Attn: AIR 03B	1	Attn: Library 60-3	1
AIR 03C	1	Ch, Wind Tunnel &	
AIR 320	1	Flight Div.	1
Department of the Navy		21000 Brookpart Road	
Washington, DC 20360		Cleveland, OH 44135	
Office of Navy Research		NASA	
Attn: ONR 100	1	George C. Marshall Space	
Morton Cooper, 430B	1	Flight Center	
800 North Quincy Street		Attn: Mr. W. K. Dahm, ED 31	1
Arlington, VA 22217		Huntsville, AL 35812	
Commander		NASA	
Naval Ship Research and		Attn: F. C. Schwenk, Director,	
Development Center		Research (Code RR)	1
Attn: Central Library Br. (5641)	1	600 Independence Ave., S.W.	
Aerodynamics Lab. (5643)	1	Washington, DC 20546	
Bethesda, MD 20035			
Commander, Naval Weapons Center		NASA	
Attn: Technical Lib. (533)	1	P.O. Box 33	
Code 406	1	College Park, MD 20740	1
China Lake, CA 93555			

DISTRIBUTION (Cont.)

	<u>Copies</u>		<u>Copies</u>
NASA Ames Research Center		Los Angeles Air Force Station	
Attn: Dr. M. Horstman	1	SAMSO/DYAE	
P. Kutler	1	Attn: Code RSSE	1
L. H. Jorgensen	1	Code RSSM	1
E. J. Hopkins	1	P.O. Box 92960, Worldway Postal	
H. H. Album	1	Center	
Moffett Field, CA 94035		Los Angeles, CA 90009	
Technical Library		Headquarters, Arnold Engineering	
Director Defense Research and		Development Center	
Engineering (DDR+E)		Attn: Library Documents	1
Attn: Stop 103	1	R. W. Henzel, TD	1
Room 3E-1063, The Pentagon		Arnold Air Force Station, TN 37389	
Washington, DC 20301			
Defense Documentation Center		von Karman Gas Dynamics Facility	
Cameron Station		Attn: Dr. J. Whitfield, Chief	1
Alexandria, VA 22314	12	ARO, Inc.	
		Arnold Air Force Station, TN 37389	
Commander (5632.2)		Commanding Officer, Harry	
Attn: Technical Library	1	Diamond Laboratories	
Naval Missile Center		Attn: Library, RM 211, Bldg. 92	1
Point Mugu, CA 93041		Washington, DC 20438	
Commanding Officer		Commanding General	
USA Aberdeen Research and		U.S. Army Missile Command	
Development Center		Attn: AMSMI-RR	1
Attn: DEXER-TS-ST	1	Ch, Document Sec.	1
Aberdeen Proving Ground, MD 21005		AMSMI-RDK, Mr. R. Deep	1
		AMSMI-RDK, Mr. T. Street	1
Naval Surface Weapons Center		Redstone Arsenal, AL 35809	
Dahlgren Laboratory			
Attn: Library	1	Department of the Army	
T. Pepitone (DK-21)	1	Office of the Chief of	
Dahlgren, VA 22448		Research and Development	
Director, Strategic Systems		ABMDA, The Pentagon	
Project Office		Washington, DC 20350	1
Attn: SP-2722	1	Commanding Officer	
Department of the Navy		Picatinny Arsenal	
Washington, DC 20390		Attn: Mr. A. A. Loeb	1
		SMUPA-VC-3	1
Director of Intelligence		Dover, NJ 07801	
Hdqs., USAF (AFNINDE)		Commander (ADL)	
Attn: AFOIN-3B	2	Naval Air Development Center	
Washington, DC 20330		Johnsville, PA 18974	1

DISTRIBUTION (Cont.)

	<u>Copies</u>		<u>Copies</u>
Air Force Weapons Laboratory Kirtland Air Force Base Attn: Technical Library (SUL) Albuquerque, NM 87117	1	Aerospace Engineering Program University of Alabama Attn: Prof. W. K. Rey, Chm. P.O. Box 2908 University, Alabama 35486	1
U.S. Army Ballistic Missile Defense Agency 1300 Wilson Blvd. Arlington, VA 22209	1	AME Department University of Arizona Attn: Dr. L. B. Scott Tucson, AZ 85721	1
The Johns Hopkins University (C/Now 7386) Applied Physics Laboratory Attn: Document Library Dr. L. Croniceh 8621 Georgia Ave. Silver Spring, MD 20910	1 1	Polytechnic Institute of Brooklyn Graduate Center Library Attn: Dr. J. Polczynski Route 110, Farmindale Long Island, NY 11735	1
Director, Defense Nuclear Agency Headquarters DASA Attn: STSP (SPAS) Washington, DC 20305	1	Polytechnic Institute of Brooklyn Spicer Library Attn: Reference Department 333 Jay Street Brooklyn, NY 11201	1
Commanding Officer Naval Intelligence Support Center 4301 Suitland Road Washington, DC 20390	1	California Institute of Technology Attn: Graduate Aeronautical Labs. Aero Librarian Prof. J. Knowles Pasadena, CA 91109	1 1
Department of Aeronautics DFAN USAF Academy, Colorado 80840	1	University of California Dept. of Mechanical Engineering Berkeley, CA 94720	1
Armament Development and Test Center Attn: Technical Lib. DLOSL Eglin AFB, FL	1	Notre Dame University Attn: Dr. T. Muller Dr. R. Nelson Dr. F. Raven Dept. Of Aero Eng., College of Engineering Library Notre Dame, Indiana 46556	1 1 1 1 1
Headquarters, Edgewood Arsenal Attn: Dr. C. Murphy Edgewood Arsenal, MD 21010	1		
AFFDL/FX Wright-Patterson Air Force Base Dayton, OH 45433	1		
Naval Air Test Facility Lake Hurst, NJ 08733	1		

DISTRIBUTION (Cont.)

	<u>Copies</u>		<u>Copies</u>
GASDYNAMICS		Cornell University	
University of California		Graduate School of Aero.	
Richmond Field Station		Engineering	
1301 South 46th Street		Attn: Prof. W. R. Sears	1
Richmond, CA 94804	1	Prof. F. K. Moore,	1
		Head Thermal Engineering	
Department of Aerospace		Dept., 208 Upson Hall	
Engineering		Ithaca, NY 14850	
University of Southern			
California		University of Delaware	
Attn: Dr. John Laufer	1	Mechanical and Aeronautical	
University Park		Engineering Dept.	
Los Angeles, CA 90007		Attn: Dr. James E. Danberg	1
		Newark, DE 19711	
University of California -			
San Diego		Georgia Institute of	
Department of Aerospace and		Technology	
Mechanical Engineering	1	Attn: Dr. Arnold L. Ducoffe	1
Sciences		225 North Avenue, N.W.	
LaJolla, CA 92037		Atlanta, Georgia 30332	
Case Western Reserve		Technical Reports Collection	
University		Gordon McKay Library	
Division of Fluid, Thermal		Harvard University	
and Aerospace Engineering		Div. of Eng. and	
Cleveland, OH 44106	1	Applied Physics	
		Pierce Hall	
The Catholic University of		Oxford Street	
America		Cambridge, MA 02138	1
Attn: Dr. M. J. Casarella			
Mechanical Engr. Dept.	1	Illinois Institute of	
Washington, DC 20017		Technology	
		Attn: Dr. M. V. Morkovin	1
University of Cincinnati		Prof. A. A. Ferjer	
Attn: Dr. Arnold Polak	1	M.A.E. Dept.	1
Department of Aerospace		3300 South Federal	
Engineering		Chicago, IL 60616	
Cincinnati, OH 45221			
		University of Illinois	
Department of Aerospace		101 Transportation Bldg.	
Engineering Sciences		Attn: Aeronautical and	
University of Colorado		Astronautical Engineering	
Boulder, CO 80302	1	Department	1
		Urbana, IL 61801	

DISTRIBUTION (Cont.)

	<u>Copies</u>		<u>Copies</u>
Iowa State University Attn: Aerospace Engineering Department Ames, Iowa 50010	1	University of Michigan Attn: Dr. M. Sichel, Dept of Aero Engr.	1
		Engineering Library	1
		Aerospace Engineering Lib.	1
The Johns Hopkins University Attn: Prof. S. Corrsin Baltimore, MD 21218	1	Mr. C. Cousineau, Engin-Trans Lib.	1
		Ann Arbor, MI 48104	
University of Kentucky Wenner-Gren Aero. Lab. Attn: C. F. Knapp Lexington, KY 40506	1	Serials and Documents Section General Library University of Michigan Ann Arbor, MI 48104	1
Department of Aero. Engineering, ME 106 Attn: Dr. P. H. Miller Louisiana State University Baton Rouge, LA 70803	1	Mississippi State University Department of Aerophysics and Aerospace Engineering Attn: Mr. Charles B. Cliett P.O. Drawer A State College, MI 39762	1
University of Maryland Attn: Dr. S. I. Pai, Institute for Fluid Dynamics and Applied Mathematics Dr. Redfield W. Allen, Department of Mechanical Engineering Dr. W. L. Melnik, Department of Aerospace Engineering Dr. John D. Anderson, Jr., Department of Aerospace Engineering College Park, MD 20740	1	U.S. Naval Academy Attn: Engineering Department Aerospace Division Annapolis, MD 21402	1
		Library, Code 2124 U.S. Naval Postgraduate School Attn: Technical Reports Section Dr. Alan Fuchs Monterey, CA 93940	1
Michigan State University Library Attn: Documents Department East Lansing, MI 48823	1	New York University University Heights Attn: Dr. Antonio Ferri, Director of Guggenheim Aerospace Laboratories Prof. V. Zakkay Engineering and Science Library New York, NY 10453	1
Massachusetts Institute of Technology Attn: Dr. E. E. Covert Aerophysics Laboratory Cambridge, MA 02139	1	North Carolina State College Attn: Dr. F. R. DeJarnette, Dept. Mech. and Aero. Engineering Dr. H. A. Hassan, Dept. of Mech. and Aero. Engr. Raleigh, NC 27607	1

DISTRIBUTION (Cont.)

<u>Copies</u>	<u>Copies</u>
D. H. Hill Library North Carolina State University P.O. Box 5007 Raleigh, NC 27607	1
University of North Carolina Attn: Department of Aero. Engineering Library, Documents Section AFROTC Det 590 Chapel Hill, NC 27514	1 1 1
Northwestern University Technological Institute Attn: Department of Mechanical Engineering Library Evanston, IL 60201	1 1
Virginia Polytechnical Institute Attn: Prof. G. Inger Blacksburg, VA 24061	1
Department of Aero-Astro Engineering Ohio State University Attn: Engineering Library Prof. J. D. Lee Prof. G. L. Von Eschen 2036 Neil Avenue Columbus, OH 43210	1 1 1
Ohio State University Libraries Documents Division 1858 Neil Avenue Columbus, OH 43210	1
The Pennsylvania State University Attn: Dept. of Aero Engr. Hammond Bldg. Library, Documents Section Dr. McCormick University Park, PA 18602	1 1 1
Beyler Engineering Library 126 Benedum Hall University of Pittsburgh Pittsburgh, PA 15261	1
Princeton University Aerospace & Mechanical Science Dept. D-214 Engrg. Quadrangle Princeton, NJ 08540	1
Purdue University School of Aeronautical and Engineering Sciences Lafayette, IN 47907	1
Rensselaer Polytechnic Institute Attn: Dept of Aeronautical Engineering and Astronautics Troy, NY 12181	1
Department of Mechanical Industrial and Aerospace Engineering Attn: Dr. R. H. Page Dr. C. F. Chen Rutgers - The State University New Brunswick, NJ 08903	1 1
Stanford University Attn: Librarian, Dept. of Aeronautics and Astronautics Stanford, CA 94305	1
Stevens Institute of Technology Attn: Mechanical Engineering Department Library Hoboken, NJ 07030	1 1
The University of Texas at Austin Applied Research Laboratories Attn: Director Engr. S.B.114B/ Dr. Friedrich P.O. Box 8029 Austin, TX 78712	1 1

DISTRIBUTION (Cont.)

	<u>Copies</u>		<u>Copies</u>
University of Toledo 2801 W. Bancroft Attn: Dept. of Aero Engineering Dept. of Mech Engineering Toledo, OH 43606	1 1	University of Maryland Baltimore County (UMBC) Attn: Dr. R. C. Roberts, Mathematics Department 5401 Wilkens Avenue Baltimore, MD 21228	1
University of Virginia School of Engineering and Applied Science Charlottesville, VA 22901	1	Systems Research Laboratories, Inc. 2800 Indian Ripple Road Attn: Dr. C. Ingram Dayton, OH 45440	1
University of Washington Attn: Engineering Library Dept. of Aeronautics and Astronautics Prof. R. E. Street, Dept. of Aero. and Astro. Prof. A. Hertzberg, Aero. and Astro., Guggenheim Hall Seattle, WA 98105	1 1 1 1	Institute for Defense Analyses Attn: Classified Library 400 Army-Navy Drive Arlington, VA 22202	1
West Virginia University Attn: Library Morgantown, WV 26506	1	Kaman Sciences Corporation P.O. Box 7463 Attn: Library Colorado Spring, CO 80933	1
Federal Reports Center University of Wisconsin Attn: S. Reilly Mechanical Engineering Building Madison, WI 53706	1	Kaman Science Corporation Avidyne Division Attn: Dr. J. R. Ruetenik 83 Second Avenue Burlington, MA 01803	1
Prototype Development Associates 1740 Garry Avenue Attn: Dr. J. Dunn Dr. P. Crenshaw Suite 201 Santa Ana, CA 92705	1 1	Rockwell International B-1 Division Technical Information Center (BA08) International Airport Los Angeles, CA 90009	1
Los Alamos Scientific Laboratory Attn: Report Library P.O. Box 1663 Los Alamos, NM 87544	1	Rockwell International Corporation Technical Information Center 4300 E. Fifth Avenue Columbus, OH 43216	
		M. I. T. Lincoln Laboratory Attn: Library A-082 P.O. Box 73 Lexington, MA 02173	1

DISTRIBUTION (Cont.)

	<u>Copies</u>		<u>Copies</u>
The RAND Corporation		General Dynamics	
Attn: Library - D	1	Attn: Research Library 2246	1
1700 Main Street		George Kaler, Mail Zone	
Santa Monica, CA 90406		2880	1
		P.O. Box 748	
Aerojet Electrosystems Co.		Fort Worth, TX 76101	
Attn: Engineering Library	1		
1100 W. Hollyvale Ave.		Calspan Corporation	
Azusa, CA 91702		Attn: Library	1
		4455 Genesee Street	
The Boeing Company		Buffalo, NY 14221	
Attn: 87-67	1		
P.O. Box 3999		Air University Library	1
Seattle, WA 98124		(SE) 63-578	
		Maxwell Air Force Base, AL 36112	
Lockheed Missiles and Space Company			
Attn: Mr. G. M. Laden, Dept.		McDonnell Company	
81-25, Bldg. 154	1	P.O. Box 516	
P.O. Box 504		Attn: R. D. Detrich, Dept. 209	
Sunnyvale, CA 95086		Bldg. 33	1
		W. Brian Brooks	1
Lockheed Missiles and Space Company		St Louis, MI 63166	
Attn: Technical Information Center	1		
3251 Hanover Street		McDonnell Douglas Astronautics Co. - West	
Palo Alto, CA 94304		Attn: A3-339 Library	1
		J. S. Murphy, A3-833	1
Lockheed-California Company		M. Michael Briggs	1
Attn: Central Library, Dept.		5301 Bolsa Avenue	
84-40, Bldg. 170		Huntington, Beach, CA 92647	
PLT. B-1	1		
Burbank, CA 91503		Fairchild Hiller	
		Republic Aviation Division	
Vice President and Chief Scientist		Attn: Engineering Library	1
Dept. 03-10		Farmingdale, NY 11735	
Lockheed Aircraft Corporation			
P.O. Box 551		General Applied Science Laboratories, Inc.	
Burbank, CA 91503	1	Attn: Dr. F. Lane	1
		L. M. Nucci	1
Martin Company		Merrick and Steward Avenues	
Attn: Mr. H. J. Diebolt	1	Westbury, Long Island, NY 11590	
3211 Trade Winds Trail			
Orlando, FL 32805		General Electric Company	
		Attn: Dr. H. T. Nagamatsu	1
		Research and Development Lab. (Comb. Bldg.)	
		Schenectady, NY 12301	

DISTRIBUTION (Cont.)

	<u>Copies</u>		<u>Copies</u>
The Whitney Library		LTV Aerospace Corporation	
General Electric Research		Missiles and Space Division	
and Development Center		Attn: MSD-T-Library	
The Knolls, K-1		P.O. Box 6267	1
Attn: M. F. Orr, Manager	1	Dallas, TX 75222	
P.O. Box 8			
Schenectady, NY 12301		Northrop Norair	
		Attn: Tech. Info. 3360-32	1
General Electric Company		3901 West Broadway	
Missile and Space Division		Hawthorne, CA 90250	
Attn: MSD Library,			
Larry Chasen, Mgr.	1	Government Documents	
P.O. Box 8555		The Foundren Library	
Philadelphia, PA 19101		Rice Institute	
		P.O. Box 1892	
General Electric Company		Houston, TX 77001	1
Re-Entry & Environmental Systems			
Division		Grumman Aircraft	
Attn: Dr. S. M. Scala	1	Engineering Corporation	
Dr. H. Lew	1	Bethpage, Long Island, NY 11714	1
Mr. J. W. Faust	1		
A. Martellucci	1	Marquardt Aircraft	
W. Daskin	1	Corporation	
J. D. Cresswell	1	16555 Saticoy Street	
J. Pettus	1	Attn: Library	
L. A. Marshall	1	Van Nuys, CA 91409	1
J. Cassanto	1		
R. Hobbs	1	ARDE Associates	
C. Harris	1	P.O. Box 286	
F. George	1	Attn: Librarian	1
T. J. Duffy	1	580 Winters Avenue	
J. Schell	1	Paramus, NJ 07652	
G. Beardslee	1		
3198 Chestnut Street		Aerophysics Company	
Philadelphia, PA 19101		Attn: Mr. G. D. Boehler	1
		3500 Connecticut Ave., N.W.	
AVCO-Everett Research		Washington, DC 20003	
Laboratory			
Attn: Library	1	Aeronautical Research	
2385 Revere Beach Parkway		Associates of Princeton	
Everett, MA 02149		Attn: Dr. C. duP. Donaldson	1
		50 Washington Road	
LTV Aerospace Corporation		Princeton, NJ 08540	
Vought Aeronautics Division			
Attn: Unit 2-51131 (Library)	1		
P.O. Box 5907			
Dallas, TX 75222			

DISTRIBUTION (Cont.)

	<u>Copies</u>		<u>Copies</u>
General Reserach Corporation 5383 Hollister Avenue Attn: Technical Information Office	1	AVCO Missiles Systems Division Attn: E. E. H. Schurmann J. Otis	1 1
P.O. Box 3587 Santa Barbara, CA 93105		201 Lowell Street Wilmington, MA 01887	
Sandia Laboratories Mail Service Section Attn: Mr. W. H. Curry, Div. 1331	1	Chrysler Coproraton Space Division Attn: N. D. Kemp, Batp. 2910 E. A. Rawls, Dept. 2920	1 1
Albuquerque, NM 87115		P.O. Box 29200 New Orleans, LA 70189	
TRW Systems Group Attn: Technical Libr/Doc Acquisitions	1	General Dynamics Pomona Division Attn: Tech. Doc. Center, Mail Zone 6-20	1
1 Space Park Redondo Beach, CA 90278		P.O. Box 2507 Pomona, CA 91766	
Stanford Research Institute Attn: Dr. G. Abrahamson	1	Hear, Inc. 510 Clyde Avenue Mountain View, CA 94043	1
333 Ravenswood Avenue Menlo Park, CA 94025			
University of Tennessee Attn: Prof. J. M. Wu	1		
Space Institute Tullahoma, TE 37388			
CONVAIR Division of General Dynamics Library and Information Services			
P.O. Box 12009 San Diego, CA 92112	1		